University of Exeter

College of Engineering, Mathematics and Physical Sciences

Applications of Brillouin Light Scattering within the Biological Environment

Thesis for the Degree of Doctor of Philosophy in Physics

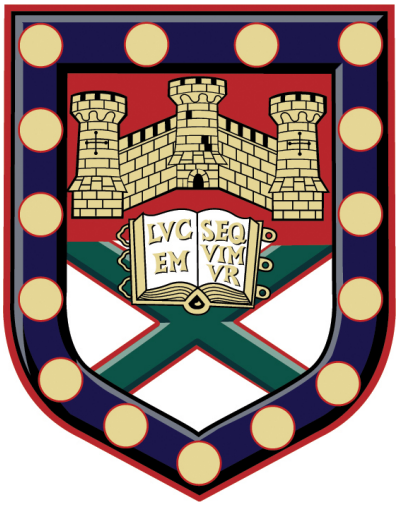

Submitted to the University of Exeter by

Michelle Louise Bailey

Supervised by:

Prof. Francesca Palombo Prof. Nick Stone

I certify that all material in this thesis which is not my own work has been identified and that no material has previously been submitted and approved for the award of a degree by this or any other University.

25th May 2022 *M. L. Bailey*

Abstract

Brillouin light scattering (BLS) provides information on micromechanics through the scattering of light from acoustic waves or phonons. It is widely accepted that the mechanical properties within the biological environment are crucial to the health and vitality of the system, and alterations in mechanics can thereby indicate disease. To date, biological applications of BLS have ranged from the measurement of live cells and organisms, to tissues and fibrous proteins, demonstrating potential for diagnosis of pathology and characterisation of mechanics. Despite this, the information contained within the Brillouin spectrum, and its full significance to biological matter, is still a matter of debate, due to fundamental problems in understanding the role of water in biomechanics.

This work aimed to explore the development and application of BLS to the biological environment, using gelatin hydrogels as a model system. Tuning the degree of physical and chemical cross-linking within the hydrogels, enabled the macromechanical properties to be controlled, mimicking a variety of biological states. Brillouin measurements of these hydrogels gave a unique insight into the viscoelastic properties across a wide range of physical states, ranging from the highly hydrated to the glassy phase, and the transition between the two. The introduction of Raman spectroscopy as a correlative technique enabled the chemical composition of the sample to be determined, in addition to the mechanical information provided by BLS. As well as this, a calibration curve derived from Raman spectra and refractometry data, enabled the refractive index of the hydrogels to be predicted, a parameter necessary to calculate the longitudinal elastic modulus from Brillouin measurements. The final focus of this work was on the development of a virtually imaged phase array (VIPA) based Brillouin spectrometer, exploring system design and experimental considerations for Brillouin measurements. This enabled comparison with measurements from a tandem Fabry-Pérot based system, as well as some consideration to the analysis methods used for the interpretation of Brillouin data. Throughout this work, gelatin hydrogels have been used as a platform to investigate the development and application of BLS to biological systems. As simple models for a host of biological systems, the viscoelastic properties revealed by Brillouin spectroscopy set the basis for BLS within the biological environment.

Acknowledgements

First and foremost, acknowledgement and thanks must go to Cancer Research UK and the EPSRC for funding this PhD project, as well as the BioBrillouin EU COST Action which financially supported multiple research trips as part of this work. In addition to the financial support, there are many other people to thank that have made this research happen.

It's safe to say, I couldn't have achieved this without the help and guidance from my two supervisors, Prof. Francesca Palombo and Prof. Nick Stone. I've been so lucky to work with two such genuinely nice and supportive people. Francesca, your enthusiasm is truly infectious, and I couldn't have wished for a better supervisor. Thank you for always making the time to support and guide me over the last 4 years, and for giving me the freedom to write this thesis in my time and in my own way. You're encouragement and belief in me has made all the difference, and I'm truly grateful for all your support and guidance. Nick, thank you for all your input and expertise, and for building such a relaxed, yet hard-working work environment. Your kindness, patience and passion for research is incredible.

With such fantastic people at the helm, it's unsurprising that the BioSpec group has been a pleasure to work in. And we even made it on that canoeing trip! Thank you to Noemí for the endless treats and coffee, and for answering all my optics questions, you definitely looked after me! Laura, Jenni, Hannah, Doriana, and more recently, Ioana, thank you for all the "Speccy" coffee breaks and catch-ups. Thank you to the wider Biophysics group for the lunchtime entertainment, pub trips, walks, Christmas meals and occasional park run. Thanks to Dave, the epicentre of Physics, Anna, Beth, Skye, Fay, Tobi, Michael and Rikke for the much needed tea breaks, and Ryan, Seb, Michele, Pascaline, Krupakar, Adrian, Alex (D and C), Chuck, Marzieh and anyone else I may have forgotten. Thank you to Ellen, for being so welcoming on my first day as a PhD student, and always being around to answer questions and help with research, all whilst looking after the Biophysics labs. To my unofficial third supervisor, Peter Winlove. Thank you for the many fruitful discussions and ideas, and for always having an open door when it came to answering questions, or giving

advice. Richard, thank you for patiently teaching me about ultrasound elastography, and for your endless positivity and enthusiasm. Suzy, thank you for listening to me talk endlessly about Willow, and for giving me a great distraction from thesis writing in the form of cell culture training. Last but not least, thanks goes to Ben (one of my favourite colleagues) for your expertise in data analysis/Matlab, proof-reading parts of this thesis, and also for all the little adventures we've had, and laughs along the way. I can't thank you enough for all your support and weird and wonderful friendship.

A special mention needs to go to the GHOST laboratory at the University of Perugia. Daniele, Martina and Silvia, grazie mille for welcoming me into your lab, and giving so much of your time to this work. At least a third of this thesis wouldn't exist if it weren't for the time I spent in Perugia. Maybe now the thesis is written, I can try and learn some Italian...

Thank you also to MPhys students Emily Francis-Pollin and Morgan Nancarrow, who's hard work during their project contributed to the Young's modulus measurements presented within this thesis. You were both a pleasure to work with.

Going back to where it all started, thank you to my parents, for bringing me into existence and allowing me to make the spontaneous decisions that led me to a Physics degree, and then a PhD. Thank you also for persisting with proof-reading the Introduction chapter - I hope you learned something! Thank you to my school physics teachers Mr Rudd and Mr Sherwood, and academic tutor Mr Bull for encouraging me to do a Physics degree in the first place. To think, I came so close to not even taking Physics as an A level. 16 year old me certainly didn't see myself doing a PhD in Biophysics!

Finally, this section wouldn't be complete without including Willow, my little furry office buddy whilst working from home. Her main contribution to this thesis may have been chewing through my notes, but she never fails to bring a smile to my face.

Publications

- N. Correa, M. Alunni Cardinali, **M. Bailey**, D. Fioretto, P. D. Pudney & F. Palombo, "Brillouin microscopy for the evaluation of hair micromechanics and effect of bleaching", *Journal of Biophotonics*, e202000483 (2021)
- **M. Bailey**, B. Gardner, M. Alunni-Cardinali, S. Caponi, D. Fioretto, N. Stone & F. Palombo, "Predicting the refractive index of tissue models using light scattering spectroscopy", *Applied Spectroscopy*, 75(5), 574-580 (2021)
- **M. Bailey**, M. Alunni-Cardinali, N. Correa, S. Caponi, T. Holsgrove, H. Barr, N. Stone, C. P. Winlove, D. Fioretto & F. Palombo, "Viscoelastic properties of biopolymer hydrogels determined by Brillouin spectroscopy: A probe of tissue micromechanics", *Science advances*, 6(44), eabc1937 (2020)
- **M. Bailey**, N. Correa, S. Harding, N. Stone, S. Brasselet, & F. Palombo, "Brillouin microspectroscopy data of tissue-mimicking gelatin hydrogels", *Data in brief*, 29, 105267 (2020)
- N. Correa, S. Harding, **M. Bailey**, S. Brasselet & F. Palombo . "Image analysis applied to Brillouin images of tissue-mimicking collagen gelatins", *Biomedical optics express*, 10(3), 1329-1338 (2019)

Contents

List of Figures

List of Tables

List of Abbreviations

AS	anti-Stokes
BLS	Brillouin light scattering
CCD	Charge-coupled device
Cryo-SEM	Cryo-Scanning Electron Microscopy
DHO	Damped harmonic oscillator
DPSS	Diode-pumped solid-state (laser)
EMCCD	Electron multiplying charge-coupled device
FSR	Free spectral range
FWHM	Full width at half maximum
ISBS	Impulsive stimulated Brillouin scattering
KWW	Kohlrausch-Williams-Watts
LHS	Left hand side
MCT	Mode coupling theory
NA	Numerical aperture
NPBS	Non-polarising beam splitter
ODT	Optical diffraction tomography
PBS	Polarising beam splitter
PCA	Principal component analysis
PC	Principal component
RHS	Right hand side
ROI	Region of interest
S	Stokes
SBS	Stimulated Brillouin scattering
SNR	Signal to noise ratio
TFP	Tandem Fabry-Pérot
TFP-2 HC	High contrast tandem Fabry-Pérot
TFPI	Tandem Fabry-Pérot interferometer
VIPA	Virtually imaged phase array
$\lambda/2$	Half waveplate
$\lambda/4$	Quarter waveplate

1. Introduction

This chapter contains sections from the following publications: "Viscoelastic properties of biopolymer hydrogels determined by Brillouin spectroscopy: A probe of tissue mechanics" [1], and "Predicting the refractive index of tissue models using light scattering spectroscopy" [2].

The mechanical properties of living cells and tissues are essential contributors to their physiological function and, on a microscopic scale, they determine many aspects of cellular activity [3–5]. These properties are largely determined by the cytoskeleton in the cell and by networks of collagen and elastin fibres in the extracellular matrix. Classical mechanical testing has provided a basis for understanding how the composition and organisation of the networks in specific tissues yield the requisite mechanical properties, and has demonstrated functionally relevant changes in diseases ranging from osteoarthritis to cancer. Although highly successful in many *ex vivo* applications, commonly used techniques such as AFM [6–8] and micropipette aspiration [9–11] require contact with the sample, and are limited to surface properties only [12]. Ultrasound elastography [13–15], commonly used in the clinical setting, has proven to be a useful diagnostic probe; however, the low spatial resolution of the technique limits it to the macroscopic regime. Research interest in many of the aforementioned diseases has now moved to the sub-cellular level, and this has generated an urgent need to characterise the mechanical properties of tissues on these length scales. In this framework, Brillouin microspectroscopy has emerged as a compelling tool in biomedical sciences. The technique is based on Brillouin light scattering (BLS), which is a photo-acoustic process arising from the interaction of light with thermally activated acoustic phonons* at gigahertz frequencies, resulting in inelastic light scattering [16]. Brillouin microscopy probes micro-elasticity and viscosity, and provides an all-optical means of measuring micro-mechanical properties of biological samples.

*Brillouin scattering of light from magnons is also possible and is significant in the study of magnetic materials, but the focus of this work is on scattering from acoustic phonons only.

1.1. Brillouin light scattering

1.1.1. Historical overview

Brillouin light scattering takes its name from the French scientist Léon Brillouin, who is often credited as the first to theorise the phenomenon in his 1922 publication [16]. However, during that time Russian scientist Leonid Mandelstam was independently working on theorising the same effect, so there is some debate about who predicted the phenomenon first. It is therefore sometimes referred to as "Brillouin-Mandelstam" scattering, although Mandelstam did not publish his theory until 1926 [17]. Brillouin began his work on light scattering some time prior to his 1922 publication [16], and in conference proceedings from a meeting in 1968 [18] whilst discussing his discovery, Brillouin states that "the original nucleus of the whole story" was contained in his 1914 publication [19]. However, the First World War interrupted this work somewhat, as Brillouin joined the French signal corps as a radio engineer, in his own words "completely forgetting my scattering problems" [18]. In 1919 he was demobilised and resumed his research, seeking to complete his PhD thesis. Struggling to decipher his notes (a lesson to all students on the importance of good record keeping) he started again, working backwards from his 1914 publication [19], and finally published the work as part of his PhD thesis in the Annales de Physique in 1922 [16]. An interesting account of this story is given by Brillouin in the conference proceedings from the 1968 meeting he spoke at [18], as well as by Rank [20] who speaks of the conversations he had with Brillouin on the occasions the two met.

The first observation of Brillouin scattering came less than 10 years after Brillouin's 1922 paper [16], and was published first by Gross in 1930 [21]. This saw Mandelstam beaten to publication for the second time. Fabelinskiĭ [22] presents an interesting account of this, including letters exchanged between G. S. Landsberg, who was working with Mandelstam, and Gross regarding this work. According to these letters, it transpires that Mandelstam and Landsberg were conducting similar experiments to Gross, and in numerous letters Gross suggests the idea of a joint publication to Landsberg. However, letters from Landsberg to Gross make it clear that Mandelstam and Landsberg do not feel the work is ready for publication, but urge Gross to publish independently if he wishes. This seems to go back and forth with several exchanges until eventually Landsberg and Mandelstam appear to be satisfied with their data and suggest a simultaneous publication with Gross. Unfortunately, this comes too late, since Gross replies to inform them that he has already submitted his

work for publication, stressing that Landsberg had repeatedly advised him to do just that. Fabelinskiĭ [22] highlights the conscientious working style of Mandelstam and Landsberg, describing how the reliability and observation of the phenomenon should be tested by all possible means prior to acceptance of its existence. This is in stark contrast to the "high-risk, high-reward" approach of immediate publication seemingly favoured by Gross.

Gross' initial publication [21] used a mercury arc and a step grating to observe scattering from quartz over an 80 hour period, observing several lines shifted with respect to the wavelength of incident light. Two months later, Gross published a paper in Nature [23] on a more comprehensive work involving liquids. Here, the frequency shift observed confirms that predicted by theory, and the angle dependence is also verified. Rank [20] provides an account of these early Brillouin experiments and those that followed in the pre-laser era, the majority of which relied on either echelons or Fabry-Pérot etalons and lengthy acquisition times. The introduction of the laser in the 1960s made observation of the Brillouin peaks more straightforward, and led to more regular use of BLS [24].

1.1.2. Biological applications

The first Brillouin measurements of biological samples were carried out towards the end of the 1970s [25–28]; however, it was only 30 years later that biological applications became more prominent. The use of a virtually imaged phase array (VIPA) etalon in Brillouin spectrometers, introduced by Scarcelli and Yun in 2007 [29], enabled faster acquisition times, amenable to many biological applications. This led to a renaissance of Brillouin spectroscopy for biological application, and the past 15 years have seen the field grow in popularity, with several recent reviews and articles summarising its progress and advances [30–37]. Since then, efforts have been made to understand the origin of the Brillouin signals in biological matter, and to investigate their relevance in the biological milieu.

Brillouin spectroscopy provides a new contrast mechanism for biological samples, and has been used successfully in a variety of biological applications. Among the early biological measurements were hydrogels which were first measured by BLS in the 1970s, with further works following before the end of the 20$^{\text{th}}$ century [25, 38–41], and more recent applications focusing on bioprinting [42] and tissue engineering [43]. However, one of the most prolific applications is the cornea, due to its transparency

and easy accessibility, with early work by Vaughan and Randall in 1980 [28]. A host of works have followed this, using Brillouin spectroscopy to study ageing and disease-related stiffening [44–50], and mechanical anisotropy [51–53] of the cornea. Among these, are a selection of *in vivo* measurements [44, 45, 49, 50], with the first human *in vivo* study presented by Scarcelli and Yun in 2012 [47], and a clinical trial for keratoconus (a condition causing softening of the cornea) which has involved > 200 participants to date [54]. BLS has also been used for the study of live cells [55–61] and organisms [62–64], as well as biofluids [65], histological tissue sections [66–70], tumours [71] and tumour spheroids [72–74]. Recent works have also used BLS to probe "stiffer" tissues, such as cartilage [75, 76], bone [76–78] and dentin [79]. BLS has also been used for the study of hair [80–82], wool [83] and plant fibres [84, 85], as well as the constituent protein fibres of the extracellular matrix, collagen and elastin [26, 27, 53, 86–89]. Furthermore, it has been used to measure the complete elasticity tensor and mechanical anisotropy of some fibrous proteins [88, 90], the only technique capable of measuring this.

Since the early biological applications, there has been an effort to relate the longitudinal elastic modulus, probed by BLS, to the more commonly utilised Young's modulus [26, 27] (usually taken as a measure of stiffness). More recently, further attempts to correlate the two moduli have been made [55, 91]; however, these have been limited to the particular sample studied. Due to the different spatio-temporal scales of the two types of measurement, and the intrinsic differences in the definitions of the two moduli, the longitudinal modulus is often found to be many orders of magnitude higher than the Young's modulus determined by more classical mechanical approaches. Nevertheless, measurements and simulations on the nanoscale have revealed a Young's moduli in the GPa range, comparable to the scale of the longitudinal modulus. A further complicating factor is the contribution of water both to cell and tissue biomechanics (and therefore, to the Young's modulus) and to the Brillouin spectrum. The former has previously been established through the use of pore-elastic models [92, 93]; however, recent work suggests that the contribution of water is far more complex, with cell mechanics heavily affected by water [94–96]. In particular, osmotic-induced volume change can affect cell stiffness [94] and deformability [96], fluid flow through cell-cell gap junctions induces mechanical pattern formation [95], and cell migration in confinement is driven by cell volume regulation [97]. The contribution of water to the Brillouin spectrum is still a subject of controversy, with some reports showing that in highly hydrated fluids and gels, simulating some aspects of

the cell cytoplasm, the frequency shift of the Brillouin peak is determined by modes generated in the water phase [91, 98].

1.1.3. Instrumentation

The small shift in the weak Brillouin peaks relative to the much more intense Rayleigh peak makes good spectrometer design paramount in measuring the Brillouin spectrum. Early measurements of biological samples relied on the use of a multi-pass scanning Fabry-Pérot interferometer [25, 26] to achieve the contrast and spectral resolution required to measure the Brillouin spectra. The interferometer consists of two parallel mirrors with variable distance L between them, and transmits light of wavelength λ according to $L = m\lambda/2$, where m is an integer [99]. Piezoelectric scanning of one of the mirrors (and therefore, the cavity spacing), enables a spectrum to be measured. John Sandercock's tandem Fabry-Pérot (TFP) interferometer [99–101] introduced a second interferometer to the same translation stage, such that the overall free spectral range (FSR) is increased, whilst maintaining stability of the system. However, the scanning of the mirrors can result in lengthy spectral acquisition times, leading to the introduction of virtually imaged phase array (VIPA) etalons in spectrometer design.

The first VIPA-based Brillouin spectrometer was introduced by Scarcelli and Yun in 2007 [29]. The use of a VIPA etalon [102] to achieve dispersion of the scattered light, enabled the Brillouin spectrum to be measured without the need for scanning mirrors. The VIPA etalon comprises of a solid etalon with a partially reflective coating on one side, and a highly reflective coating on the other one, with a narrow window for light to enter. The etalon is tilted with respect to the incoming (scattered) light, and transmits an array of beams with varying phase delay. Interference of these beams results in angular dispersion of the frequency components within the beam [29, 102], hence enabling observation of the Brillouin scattered light, spatially separated from the Rayleigh peak. Since its conception, there have been numerous developments and improvements made to the VIPA spectrometer design, including the addition of multiple etalons [103–105], increased acquisition speed [106], elastic light suppression [107–111], and spectral coronagraphy [112]. Improvements in acquisition speed, spectral resolution and contrast are continuously sought to improve the applicability of the technique for biological measurements.

There are strengths and weaknesses to both measurement methods described, and both are commonly used for Brillouin measurements of biological samples. There have been some efforts to compare the two techniques [113, 114], and it has been claimed that for measurements longer than 200 ms, the recording times of the TFPI and VIPA are comparable, but the TFPI is the preferable choice based on its higher finesse [115]; however, continuous development of lab-built VIPA spectrometers and the introduction of a new model of TFP interferometer (HC TFP-2 [101]), makes it difficult to fairly compare the two. There is also variability associated with the efficiency of light coupling to the spectrometers, as well as differences in performance for transparent and turbid samples across the two techniques. It is, however, clear that both methods are limited by a trade-off between speed of acquisition and contrast. Depending on the experimental design and objectives, one of these parameters may be more important than the other, but in many cases a balance is required between the two. Similarly, comparison between a TFP interferometer and VIPA-based spectrometer is highly dependent on the experimental aims and setup.

Common to all Brillouin measurements are experimental considerations such as incident wavelength [59] and choice of scattering geometry. For example, the numerical aperture (NA) of the objective used influences the spectral line shape [116] and spatial resolution [117], with objectives with a larger NA resulting in broader peaks and decreased spectral resolution (but improved spatial resolution). Some degree of broadening due to the instrumental response function is inevitable, so deconvolution of the instrumental response function from the experimental spectra is often implemented to assess the Brillouin linewidth [33, 56, 114]. Although some work has focused on the post-processing of Brillouin data [118–121], it is an area that has received relatively little attention in comparison to developments in instrumental design.

The combination of Brillouin microscopy with other techniques enables a truly correlative approach to measurements. The combination of Brillouin and Raman spectroscopy [101], for instance, has enabled the simultaneous acquisition of the micromechanics and chemical composition of biological samples [56, 66, 67]. Fluorescence imaging has also been used in combination with Brillouin spectroscopy [58, 63], with recent developments integrating epi-fluorescence imaging, Brillouin microscopy and optical diffraction tomography (ODT) [122] to assess the mass density from refractive index measurement. Techniques such as flow cytometry have also been used in combination with Brillouin microscopy (Brillouin flow cytometry) [57], enabling the measurement of live cells as they pass through microfluidic channels. In addition to this, the development of fibre-based Brillouin probes [123–125], and the concept of

an "add-on Brillouin module" [126] demonstrate how Brillouin spectroscopy could be integrated in a versatile manner.

Although the focus of this work is on spontaneous Brillouin scattering, acknowledgement should also be given to the success of stimulated methods, involving both a *pump* and *probe* laser to stimulate the Brillouin scattering event. The development of both stimulated Brillouin scattering (SBS) [64, 127, 128] and impulsive stimulated Brillouin scattering (ISBS) [129, 130] have enabled high-speed Brillouin imaging of biological samples. Similarly, acoustic excitation through the generation of coherent acoustic pulses (the principle behind acoustic microscopy[†]) and time-resolved detection (through a series of short probe pulses) is the basis of time-resolved Brillouin scattering [123, 134–136].

1.2. Refractometry

Refractive index measurements provide key information about the optical properties of materials, essential for the interpretation of data from many optical measurement techniques. Knowledge of the refractive index (in combination with the density) in Brillouin spectroscopy, enables the longitudinal elastic modulus to be determined from Brillouin spectra, hence making it a desirable parameter to measure. The longitudinal modulus is proportional to the square-Brillouin frequency shift through the density-to-square-refractive index ratio (see Chapter 2). The Lorentz-Lorenz equation has been used successfully to assume a constant ratio of density to square-refractive index [63, 98] in materials where direct measurement is not possible, such as in point-to-point mapping experiments. However, this relation is not universal and so care must be taken, particularly in biological samples containing both aqueous-rich and lipid-rich regions, where refractive index and density may vary in opposite directions. Traditional refractometers typically require the material to be homogeneous, measuring the refraction of monochromatic light through a thin film of material sandwiched between two prisms, by determining the critical angle for the sample. Transition between measurement of liquid and solid samples is often not trivial, with different methodology required depending on the state of aggregation, and spatially resolved

[†]Acoustic microscopy utilises an acoustic lens, which focuses acoustic waves onto the sample [131, 132]. The acoustic waves are partially reflected at the sample interface with a strength proportional to the acoustic reflectivity, resulting in a diffraction-limited acoustic image [133].

measurements are not achievable. Although these methods and others have been used successfully to determine the index of refraction for homogeneous materials [137, 138] and hence for approximation of more complex materials such as cells and tissues [60, 66], they do not allow for the spatial resolution required by techniques assessing the micro-scale such as Brillouin microscopy. Advances in phase imaging have led to techniques such as quantitative phase imaging and holographic phase microscopy to be implemented alongside Brillouin spectroscopy in order to measure the refractive index of thin ($\sim$ µm) samples [62, 85], but are currently limited by sample thickness and are yet to be used simultaneously with Brillouin spectroscopy. Optical diffraction tomography (ODT), providing three-dimensional refractive index measurement of thin samples or cells, has recently been proposed as a promising technique to use alongside Brillouin microscopy [139, 140]; however, the simultaneous use of ODT with Brillouin spectroscopy has only recently come to fruition [122]. In certain scattering geometries, Brillouin spectroscopy can itself be used to determine refractive index. Incident light probing a sample (mounted on a reflective substrate) at a 45° angle enables measurement of two peaks; one from the parallel to surface mode, and the other the bulk acoustic mode. The ratio between the frequency shifts of these two peaks can be used to calculate the refractive index of the material, which can then be used to determine the longitudinal elastic modulus [86, 88]. However, due to the geometry required, this technique is not straightforward to implement in all systems, thus limiting the feasibility of this method. Recent advances have led to a system capable of measuring the refractive index based on a similar principle; however, incident light is split into two beams and simultaneously enters the sample both perpendicularly and at an angle α [141]. Both geometries probe the same acoustic phonon direction, enabling the refractive index to be determined from the Brillouin frequency shifts observed.

1.3. Thesis aims and outline

The aims of this thesis can be divided into three parts with one common denominator: the use and development of Brillouin spectroscopy. Part 1 focuses on use and applicability, seeking to explore the novel measurement capabilities of the technique, and how these can be applied to the biological milieu. Part 2 aims to explore correlative techniques, focusing on Raman spectroscopy, to add complementary information alongside Brillouin measurements and hence widen the applicability of the technique. Part 3 of these aims is focused on the development of a VIPA-based Bril-

louin microscopy system, and relevant experimental considerations associated with its improvement and use.

This thesis is divided into seven chapters, beginning with a general introduction to BLS, including relevant background and context to this work (**Chapter 1**). **Chapter 2** gives a theoretical background to Brillouin and Raman light scattering, the two fundamental techniques used within this thesis. The materials and methods used can be found in **Chapter 3**, which is followed by three results chapters. **Chapter 4** reports a study using a commercial Tandem Fabry-Pérot (TFP) interferometer to explore the viscoelastic properties of gelatin with Brillouin microscopy. Correlative compressive testing is included to measure the macro-mechanical properties of the hydrogels, and Brillouin microscopy provides the micro-mechanical information. **Chapter 5** describes the use of Raman spectroscopy to determine the chemical composition of the hydrogels, and monitor changes as the polymer concentration is adjusted. The Raman spectra of gels of varying concentration are used alongside Abbe refractometry measurements to develop a calibration model, which is used to determine the refractive index of the hydrogels from their Raman spectra. The final results chapter, **Chapter 6**, focuses on the development of a lab-built dual-stage VIPA spectrometer. Spectrometer design and methods associated with its development are included, as well as measurement considerations and analysis methods. Finally, **Chapter 7** gives an overall summary of the work and highlights the main conclusions, before giving some perspectives on the techniques used and the applicability of future work.

2. Light Scattering

When light is incident on a medium, it can either be absorbed, reflected, transmitted without interaction, or scattered, and where there is mismatch in refractive index, light will undergo refraction. The focus of this work will be on light that is scattered by the medium, in particular, Brillouin and Raman scattered light. Both of these scattering events are inelastic, meaning that there is a difference in energy (and therefore frequency and wavelength) between the incident and scattered light. Due to conservation of energy, this energy difference corresponds to the energy lost or gained by the medium during the scattering event, and can thereby be used to probe the mechanical or chemical properties of the medium. The shift in energy can be positive or negative depending on the interaction, and is denoted as *anti-Stokes* or *Stokes* scattering, respectively. This will be discussed further in Sections 2.1 and 2.2. The Stokes and anti-Stokes components appear at symmetric positions on the Brillouin and Raman spectra, centred around the peak due to Rayleigh scattered light (Figure 2.1). Elastic light scattering, or Rayleigh scattering, occurs when light

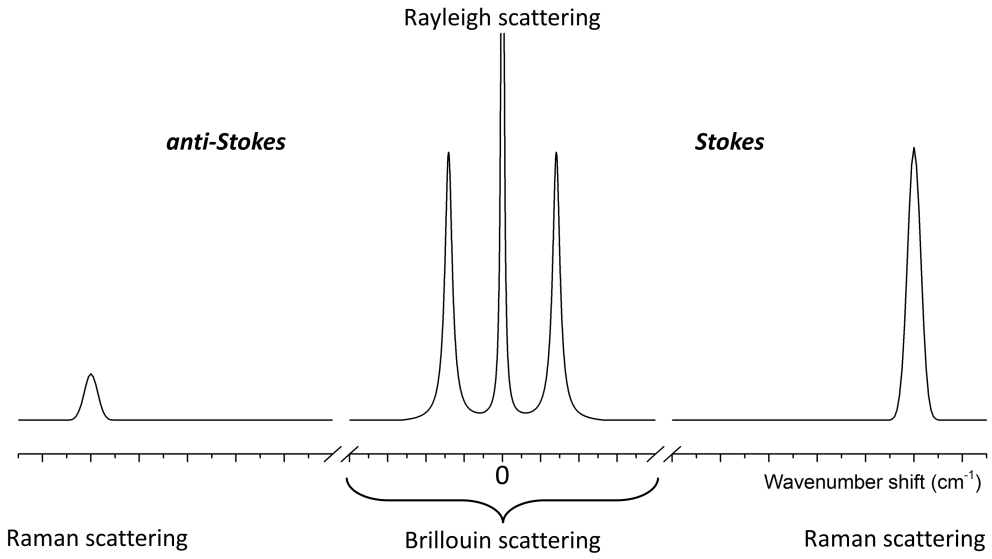

Figure 2.1.: *Brillouin and Raman scattering as a function of wavenumber shift, with peaks positioned symmetrically around the central, unshifted Rayleigh peak. Note that the Brillouin peaks occur much closer to the Rayleigh peak ($< 1\ cm^{-1}$) than the Raman spectra.*

interacts with a medium, resulting in a change in direction of the scattered light, but no change in energy or momentum [142]. The majority of light that is scattered is elastically scattered, meaning that the Rayleigh peak is much more intense than those due to the inelastically scattered light.

The intensity I of Brillouin, Raman and Rayleigh scattering is proportional to the inverse of the fourth power of the incident wavelength λ, such that $I \propto \lambda^{-4}$ [142–144]. Therefore consideration should be taken over the incident wavelength used, since light of shorter wavelength will result in higher scattering intensity. However, light of shorter wavelength is also more likely to cause damage to the sample, and fluorescence can also be problematic in the visible region [144].

2.1. Brillouin light scattering

Brillouin light scattering (BLS) is an acoustic process arising from the inelastic scattering of light [16]. The focus of this work is on spontaneous BLS, resulting from the interaction of incident light with thermally driven acoustic phonons at high frequencies. For energy and momentum to be conserved, the interaction thereby results in the annihilation or creation of a phonon, with energy $\hbar\omega$ and momentum $\hbar\boldsymbol{k}$ [143], where $\hbar\omega = \hbar\omega_i - \hbar\omega_s$ and $\hbar\boldsymbol{k} = \hbar\boldsymbol{k_i} - \boldsymbol{k_s}$, and ω and $\boldsymbol{k}$ are the angular frequency shift and wavevector, respectively; subscripts i and s denote incident and scattered light, respectively. This results in scattered light with a positive (anti-Stokes) or negative (Stokes) frequency shift ω_B, proportional to the acoustic wave velocity v of the phonon in the interaction, where $\omega_B = v|\boldsymbol{q}|$ [145]. The magnitude of the wavevector $\mathbf{q}$ can be determined geometrically from the wavevectors of incident and scattered light, shown schematically in Figure 2.2. The magnitudes of $\boldsymbol{k_i}$ and $\boldsymbol{k_s}$ are $2\pi n/\lambda_i$ and $2\pi n/\lambda_s$, respectively [143], where n is the refractive index of the medium, and λ_i and λ_s are the wavelengths of the incident and scattered light, respectively. Because the shift in wavelength of the scattered light is very small, and the speed of light much faster than the speed of sound, it can be approximated that $|\boldsymbol{k_i}| = |\boldsymbol{k_s}|$ [99, 143]. In this case, the triangle in Figure 2.2 approximates to an isosceles triangle with $|\boldsymbol{q}| = 2|\boldsymbol{k_i}| \sin(\theta/2)$, where θ is the scattering angle between the wavevectors of the incident and scattered light. Substituting in the expression for $|\boldsymbol{k_i}|$ results in

$$|\boldsymbol{q}| = \frac{4\pi n}{\lambda_i} \sin\left(\frac{\theta}{2}\right). \tag{2.1}$$

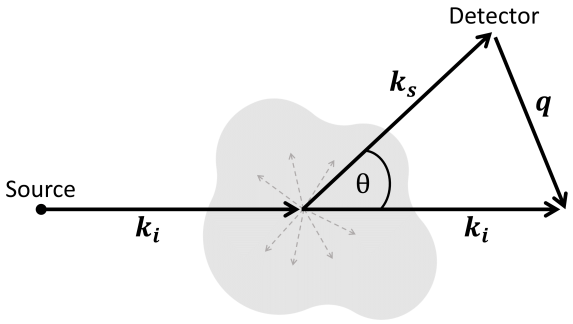

Figure 2.2.: *Schematic representation of light incident on a sample before undergoing a scattering event. Incident light with wavevector* $\boldsymbol{k_i}$ *is scattered in the direction of the detector (wavevector* $\boldsymbol{k_s}$*) at an angle* θ *with respect to the incident wavevector. The wavevector* $\boldsymbol{q}$ *can therefore be determined geometrically. Note, that light is scattered in all directions; only the light scattered in the direction of the detector is highlighted here.*

Applying the dispersion relation ($\omega_B = v|\boldsymbol{q}|$) gives

$$\omega_B = \frac{4\pi v n}{\lambda_i} \sin\left(\frac{\theta}{2}\right), \tag{2.2}$$

relating the Brillouin frequency shift to the acoustic wave velocity and the experimental parameters. In backscattering geometry ($\theta = 180°$), this simplifies to $\omega_B = 4\pi v n/\lambda_i$.

The use of high NA objectives can lead to significant variation in the scattering angle of collected wavevectors (and hence, the scattering angle θ). This results in spectral broadening, making appropriate deconvolution of the instrumental response function necessary to accurately evaluate the Brillouin linewidth. Simulations have previously shown that the Brillouin frequency shift changes negligibly ($< 2\%$) as a function of NA (in the range 0–0.9) in backscattering configuration [116].

The complex longitudinal modulus M^* is defined as:

$$M^* = M' + iM'' \tag{2.3}$$

where the storage modulus M' and loss modulus M'' are defined as:

$$M' = \rho v^2 \qquad M'' = \frac{\rho v^2 \Gamma_B}{\omega_B} \tag{2.4}$$

where Γ_B is the linewidth of the Brillouin peak and ρ is the density of the medium.

2.1.1. Elastic moduli

The elastic modulus of a material describes its response to stress or deformation. The elastic modulus is dependent on the type of deformation that is applied, with the most common (and most easily measurable) being uniaxial deformation, shear, and bulk deformations (Figure 2.3). For an isotropic material, with homogeneous stress and

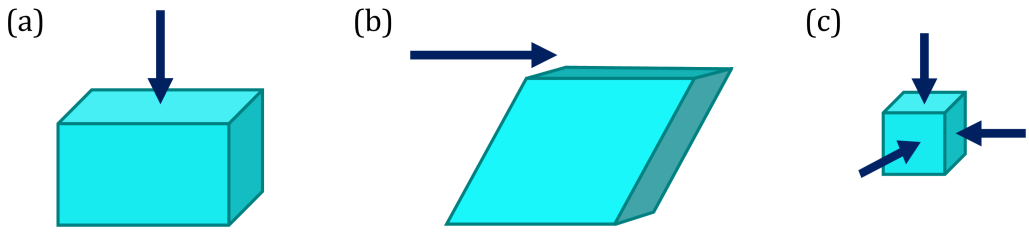

Figure 2.3.: *Deformation of a cube under (a) uniaxial compression, (b) shear stress and (c) bulk compression.*

strain distribution, Hooke's law states that the applied stress σ is proportional to the strain ϵ, such that [146, 147]:

$$c = \frac{\sigma}{\epsilon} \tag{2.5}$$

where the stress, $\sigma = F/A$ is the ratio of applied force F to surface area A, and the strain $\epsilon = \Delta l/l$ is the ratio of the change in length Δl (due to extension or compression) to original length l, and the constant c is the elastic modulus. For uniaxial deformation (Figure 2.3a), the elastic modulus is defined as the Young's modulus E of the material, and is the ratio of the tensile stress to strain. Similarly, shear deformation, where a material is deformed by a force acting parallel to its surface (Figure 2.3b) provides the shear modulus G of the material, where G is the ratio of shear stress to shear strain. For bulk compression, where force is applied in all directions to the material, resulting in a change in volume ΔV (Figure 2.3c), the elastic modulus is defined as the bulk modulus $K = -P/(\Delta V/V)$, where P is the pressure and V the volume [147]. The longitudinal modulus M can be described as a linear combination of shear and bulk moduli, such that $M = \frac{4}{3}G + K$ [148]. The elastic moduli can be related to one another by Poisson's ratio ν, where ν is a dimensionless quantity defined as $\nu = \frac{1}{2}[1 - (1/V)(\partial V/\partial \epsilon)]$ [147].

2.1.2. Stiffness tensor

The generalised form of Hooke's law linearly relates the components of stress σ_i and strain ϵ_j:

$$\sigma_i = c_{ij}\epsilon_j \tag{2.6}$$

where c_{ij} is a fourth-rank tensor containing the stiffness constants [146, 149]. The generalised form of Hooke's law accounts for the stress and strain perpendicular to the direction of the load, as well as in the direction of the load itself. For example, ϵ_1 is the sum of the strain in the direction of the load and the resulting strain in directions perpendicular to the load, such that: $\epsilon_1 = \frac{1}{E}[\sigma_1 - \nu(\sigma_2 + \sigma_z)]$.

The symmetry of the system can be used to simplify the stiffness tensor, and for an isotropic system it reduces to [146]:

$$c_{ij} = \begin{pmatrix} c_{11} & c_{12} & c_{12} & 0 & 0 & 0 \\ c_{12} & c_{11} & c_{12} & 0 & 0 & 0 \\ c_{12} & c_{12} & c_{11} & 0 & 0 & 0 \\ 0 & 0 & 0 & \frac{c_{11}-c_{12}}{2} & 0 & 0 \\ 0 & 0 & 0 & 0 & \frac{c_{11}-c_{12}}{2} & 0 \\ 0 & 0 & 0 & 0 & 0 & \frac{c_{11}-c_{12}}{2} \end{pmatrix} \tag{2.7}$$

Combining (2.6) and (2.7) and equating the σ_1 component to that derived from ϵ_1 gives [146]:

$$c_{11}\epsilon_1 + c_{12}\epsilon + 2 + c_{12}\epsilon_3 = 2\mu\epsilon_1 + \lambda(\epsilon_1 + \epsilon_2 + \epsilon_3) \tag{2.8}$$

where $\mu = \frac{E}{2(1+\nu)}$ and $\lambda = \frac{E\nu}{(1+\nu)(1-2\nu)}$ are the Lamé parameters. Putting both sides of (2.8) in a similar form:

$$\epsilon_1(c_{11} - c_{12}) + c_{12}(\epsilon_1 + \epsilon_2 + \epsilon_3) = 2\mu\epsilon_1 + \lambda(\epsilon_1 + \epsilon_2 + \epsilon_3) \tag{2.9}$$

makes it clear that $c_{11} - c_{12} = 2\mu$ and $c_{12} = \lambda$. In fact, $c_{11} = 2\mu + \lambda = \frac{E(1-\nu)}{(1+\nu)(1-2\nu)} = M$, so for an isotropic medium (as well as other crystal symmetries), the c_{11} component of the stiffness tensor is equal to the longitudinal modulus M.

2.2. Raman scattering

Raman light scattering, named after Sir C. V. Raman, was first observed experimentally, using a converged beam of sunlight, by Raman and Krishnan in 1928 [150]. Like BLS, Raman light scattering is inelastic, and so Raman scattered light is intrinsically weak relative to Rayleigh scattered light, with only 1 in every 10^6–10^8 photons that are scattered being Raman scattered [151]. Raman scattering is the result of the interaction of incident light with a molecule, resulting in energy transfer to molecular vibration. During this interaction, the energy of the incident photon is transferred to the molecule, causing it to be promoted to a *virtual* energy state. Due to the instability of the state, a photon is immediately released, with higher (anti-Stokes) or lower (Stokes) energy than the incident light (Figure 2.4) [144]. On the other hand,

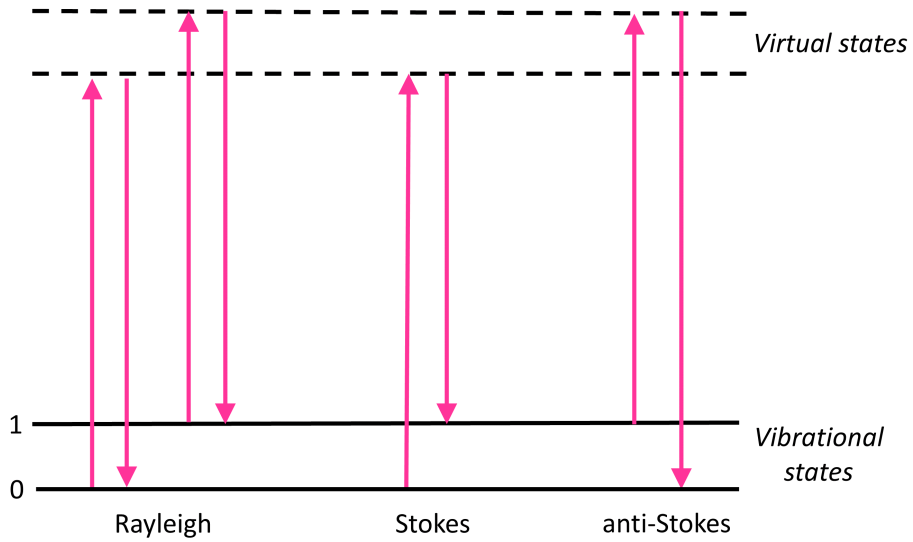

Figure 2.4.: *Energy level diagram showing transitions between vibrational (solid lines) and virtual (dashed lines) states for Rayleigh scattering and Stokes and anti-Stokes Raman scattering. 0 represents the ground state, and 1 is the first excited vibrational state. Adapted from [151]*

Rayleigh scattering does not involve nuclear displacement within the molecules, and so there is no change in energy between the incident and scattered light (Figure 2.4).

The vibrational state of a molecule is dependent on temperature, and the proportion of molecules in the ground and excited vibrational states at temperature T is given by the Boltzmann equation [144]:

$$\frac{N_1}{N_0} = \frac{g_1}{g_0} \exp\left[-\frac{(E_1 - E_0)}{kT}\right] \tag{2.10}$$

Subscripts 0 and 1 denote the ground and first excited vibrational states, respectively, $N_{0,1}$ is the number of molecules in each state and $g_{0,1}$ is the degeneracy of the state. The energy difference between the two states is given by $(E_1 - E_0)$, and k is the Boltzmann constant. At room temperature, the majority of molecules will be in the ground state, so the intensity of anti-Stokes scattered light is very low compared to the Stokes. Following (2.10), the intensity of the anti-Stokes, relative to the Stokes, will increase as temperature increases and a larger proportion of molecules are found in the excited state.

The vibrational energy of a molecule can be approximated by considering the atoms as masses connected by a spring, with a diatomic molecule behaving as a harmonic oscillator. Hooke's law can therefore be used to derive the relationship between frequency ν, bond strength (via force constant k) and mass, resulting in [142, 144]:

$$\nu = \frac{1}{2\pi}\sqrt{\frac{k}{\mu}} \tag{2.11}$$

where

$$\mu = \frac{m_A m_B}{m_A + m_B} \tag{2.12}$$

is the reduced mass of the molecule, with m_A and m_B the mass of the two atoms. Quantum mechanically, (2.11) is obtained from a second order approximation to a series expansion of the Morse potential, given by: [142]

$$V(x) = D_e \left(1 - e^{-a(x-x_0)}\right)^2 \tag{2.13}$$

where $a = \sqrt{\frac{k}{2D_e}}$ and D_e is the bond dissociation energy. Using the harmonic approximation, the energy at vibrational state n is given by

$$E_n = (n + \tfrac{1}{2})h\nu, \tag{2.14}$$

where h is Planck's constant.

From (2.11), the stronger the bond between atoms, the higher the frequency of the vibration will be, and lighter atoms will have higher frequencies than heavier ones. However, note that molecular vibrations are anharmonic, so the equations given by the harmonic approximation will result in vibrational transition frequencies slightly different to those measured experimentally. The inclusion of a higher order term to the series expansion of the potential energy function approximates this anharmonicity,

resulting in:

$$E_n = (n + \tfrac{1}{2})h\nu - (n + \tfrac{1}{2})^2 h\nu\chi. \tag{2.15}$$

$\chi = \frac{h\nu}{4D_e}$ and is always positive, meaning that the anharmonic energy levels are always slightly lower in energy than that approximated by the harmonic oscillator.

The number of vibrations a molecule has is related to the number of atoms, N_a, it is composed of. For example, a non-linear molecule is expected to have $3N_a - 6$ vibrations*, and selection rules govern which of these vibrations are Raman active [144]. Therefore, a Raman spectrum of a complex molecule may contain numerous vibrational bands at varying frequencies. The frequency of vibrations, usually measured in terms of wavenumber shift in cm^{-1}, is therefore used to determine the chemical composition of the sample.

*The total energy of a molecule can be divided into vibrational, rotational and translational energy. For a non-linear molecule, rotational and translational energy each have 3 degrees of freedom, resulting in $3N_a - 6$ vibrations [144].

3. Materials and Methods

This chapter contains sections from the following publications: "Viscoelastic properties of biopolymer hydrogels determined by Brillouin spectroscopy: A probe of tissue mechanics" [1], and "Predicting the refractive index of tissue models using light scattering spectroscopy" [2].

3.1. Hydrogel Preparation

Gelatin hydrogels were used as tissue-mimicking phantoms. Derived from denatured collagen [152], gelatin is comprised of a mixture of polypeptides with the same amino acid composition as the collagen from which it was derived [153], and exists as flexible random coils in solution [154]. The mechanical properties of gelatin can be tuned by varying the physical and chemical cross-links within the sample (Figure 3.1). The

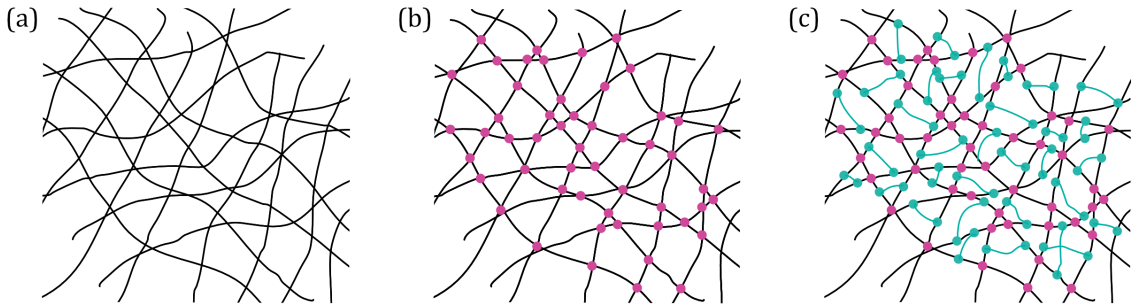

Figure 3.1.: *Schematic representation of (a) gelatin molecules, where hydrogen bonds between molecules constitute physical cross-links, represented by pink dots in (b). (c) Chemical cross-links represented by teal dots, resulting from covalent bonds between the chemical cross-linker and the gelatin molecules.*

former is concentration dependent and relates to cross-links formed by hydrogen bonds between the gelatin molecules and between gelatin and water [155], as well as contributions from hydrophobic interactions between gelatin molecules and hydrophobic hydration [156]. The latter requires the addition of a chemical cross-linker,

such as formaldehyde (a common fixative), which forms methylene bonds with the amino groups of the gelatin molecules [157–160].

Hydrogels were prepared from type-B bovine skin gelatin powder (G9382, Sigma-Aldrich) and distilled water, at concentrations ranging between 4 and 20% (w/w) solute (the solubility limit of the polymer). Gelatin powder and water were combined at the desired concentration and mixed under magnetic stirring in a water bath (temperature 55–65°C) for 60 min to ensure complete dissolution. The beaker containing the gel was then covered with parafilm to reduce evaporation effects and the gel was left to cool at room temperature.

For chemically cross-linked samples, hydrogels of 10% polymer concentration were prepared as previously described; however prior to gelation, formalin (36.5–38% formaldehyde in solution, F8775, Sigma-Aldrich) was added when the gelatin solution reached 50°C, resulting in gels comprising of 1–16% formalin.

To reach concentrations beyond the solubility limit of the gelatin powder, a hydrogel of 20% polymer concentration was prepared as previously described (Section 3.1). A small amount of gelatin solution was deposited onto a substrate and spread thinly, resulting in a 200–300 μm thick film which was left to dehydrate at room temperature.

3.2. Cryo-SEM measurements

A Jeol JSM-6390LV scanning electron microscope with a Gatan Alto 2100 cryo system was used for cryo-Scanning Electron Microscopy (cryo-SEM) measurements of gelatin hydrogels of 4 and 18% polymer. A thin slice of the gel was mounted on the sample holder using adhesive and graphite. The sample was snap frozen at -210°C by liquid nitrogen slush and then transferred to the cryo preparation chamber, where it was fractured with a razor blade to give a clean edge for imaging. The sample was left to sublime at -95°C for 30 min, and then sputter coated with gold/palladium. Measurements were taken at -135°C with a 5 kV accelerating voltage, and magnifications varying between ×400 and ×20000. Cryo-SEM measurements revealed the porous structure of the gel, comprised of interconnected cavities varying in size with gel concentration (Figure 3.2). The gels were relatively homogeneous and the cryo-SEM measurements confirmed the absence of fibres within the samples. As expected, there was a substantial difference in pore-size between gels of low ($\sim$ 4%) and high

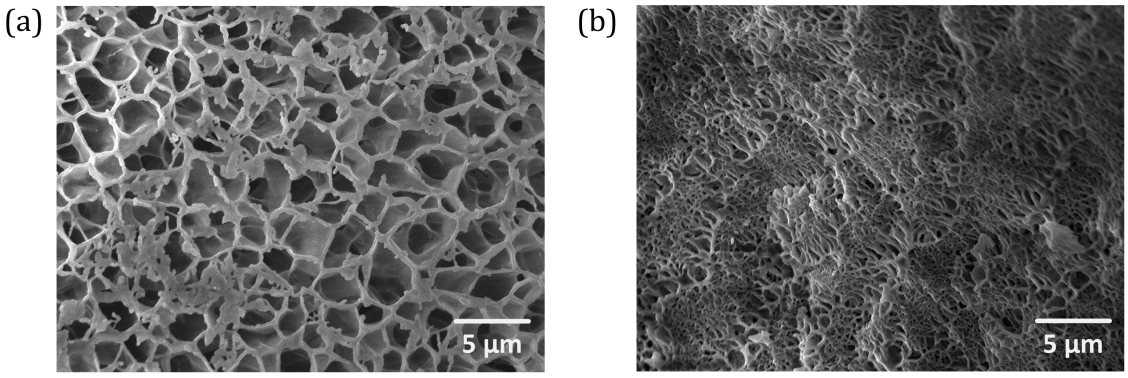

Figure 3.2.: *Cryo-SEM images of (a) 4% and (b) 18% polymer hydrogels with 5 kV accelerating voltage and ×4000 magnification.*

(∼ 18%) polymer concentration, with the less concentrated gel having a larger pore size than the latter.

3.3. Refractive Index and Density Measurement

Refractive index was measured using an Abbe refractometer (Atago model NAR-1T; resolution 0.0002 nD), with distilled water used for calibration. For hydrogels, a small sample of gel was placed between the plates of the refractometer prior to gelation (Figure 3.3), ensuring good contact with both plates. Measurements were

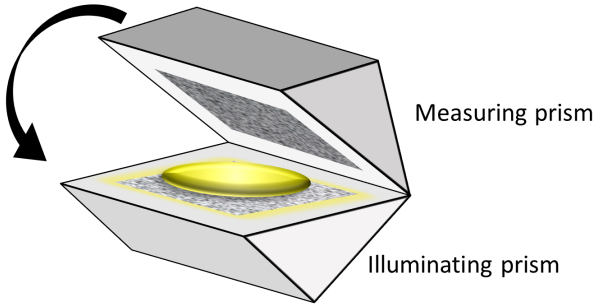

Figure 3.3.: *Schematic representation of the refractometer. The sample is placed on the lower prism (illuminating prism) and the upper prism (measuring prism) is closed, sandwiching the sample between the two prisms. A light source illuminates the matted illuminating prism, sending light into the sample at all possible angles. A telescope (not shown) is then used to measure the border between bright and dark areas to determine the critical angle and hence, the refractive index of the sample. Two compensating Amici prisms are present in the telescope to prevent dispersion.*

taken when the gel reached room temperature (average temperature at measurement 21.1±0.2°C).

Density measurements using conventional methods, such as pycnometer-based gravimetric measurements, are difficult to conduct with hydrogels due to their porous nature and fragility. Instead, the density of the hydrogels was determined using a biphasic ideal mixing model:

$$\rho = \frac{(m_w + m_g)}{\left(\frac{m_w}{\rho_w} + \frac{m_g}{\rho_g}\right)} \tag{3.1}$$

Where m_w and m_g denote the mass of water and dry gelatin respectively, and ρ_w and ρ_g the respective densities. The density of water was taken to be 1.00 g/cm^3, and the density of dry gelatin 1.35 g/cm^3 [161]. This model is based on the assumption that the hydrogels behave as ideal mixtures, i.e. there are no molecular interactions between constituents, which is not an unreasonable assumption here, since gelatin is essentially hydrophobic and has low miscibility with water.

3.4. Macro-mechanical Testing

3.4.1. Compressive testing

An Instron ElectroPuls E10000 (High Wycombe, UK) linear dynamic test instrument was used to perform unconfined compressive testing on gelatin hydrogels of 4–18% w/w polymer concentration. Prior to gelation, gels were transferred into custom-built aluminium moulds (Figure 3.4), resulting in cylindrical samples of 21 mm diameter (surface area, $A \approx 346$ mm^2) and height $L \approx 10$ mm. Approximately 24 hours after gelation, the gel samples were removed from the mould and placed on a fixed aluminium base for compressive testing (Figure 3.5). The samples were compressed at a steady rate of 0.03 mm/s until a 10% strain was reached, resulting in negligible radial deformation. The applied load, F, was measured using a 1 kN load cell ($< 2\%$ linearity error) mounted onto a flat aluminium plate in contact with the surface of the gel. WaveMatrix dynamic testing software was used to control the position of the load cell during measurements and for data acquisition. Stress-strain plots were determined for each sample and subjected to a linear curve fit to derive Young's modulus,

$$E = \frac{\sigma}{\epsilon} \tag{3.2}$$

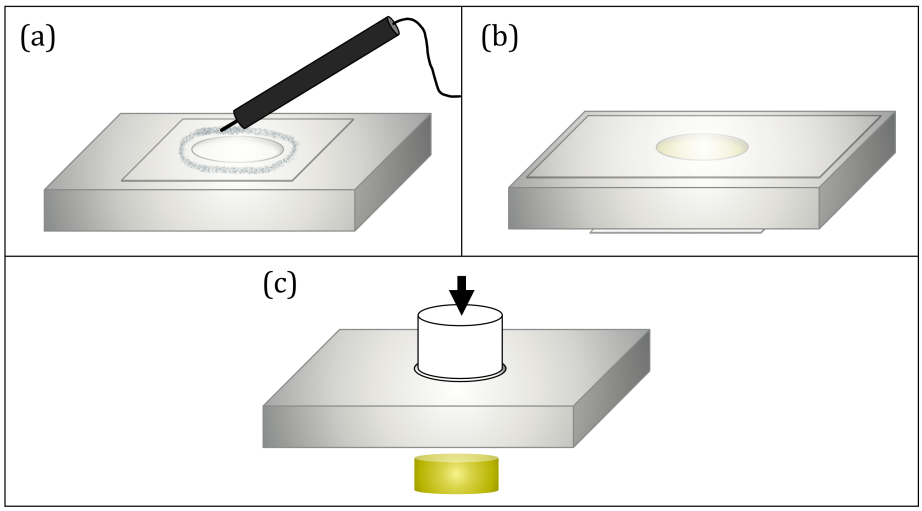

Figure 3.4.: *Custom-made aluminium mould with a cylindrical hole (21 mm diameter) through the middle, used to prepare gels for compressive testing. (a) Underside: A piece of parafilm is placed over the cylindrical hole in the aluminium, and melted slightly using a soldering iron to hold it in place. This acts as a removable base. (b) Gel is poured into the mould, covered with parafilm and left to set. (c) Prior to testing, parafilm is removed and a PTFE plunger is used to push the gel out of the mould.*

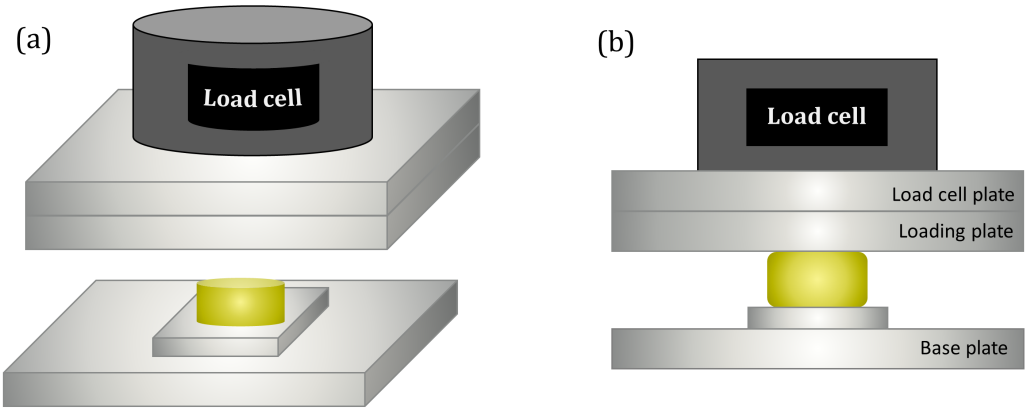

Figure 3.5.: *Compressive testing using an INSTRON ElectroPuls E10000. (a) Unloaded gel, mounted on aluminium plate for testing. (b) Side view of testing. Upper plates are lowered onto surface of the gel and compression begins. Force is measured using a 1 kN load cell.*

Where $\sigma = F/A$ and $\epsilon = \Delta L/L$ are the stress and strain, respectively, and ΔL is the decrease in height of the gel during compression.

3.4.2. Ultrasound elastography

Shear wave ultrasound elastography measurements were conducted using an ACUSON S3000 Ultrasound system (HELX Evolution with Touch Control, Siemens). Gelatin hydrogels were prepared as previously described (Section 3.1), with the addition of titanium (IV) oxide powder (TiO_2) after mixing which acted as an ultrasound scattering agent, enabling B-mode images to be generated. TiO_2 was added to the gelatin solution and combined under magnetic stirring in a water bath held at 45°C for approximately 1 h. Hydrogels were prepared to 6–18% w/w polymer concentration, and 0.1% TiO_2 and measured 24 h after gelation. For ultrasound measurements, cylindrical gel samples (diameter $\sim$ 7 cm, height 5–10 cm) were submerged in distilled water and shear wave elastograms were taken using a 9L4 transducer. The transducer was held in place parallel to the surface of the gel. Submerging the samples in water resulted in a higher quality ultrasound image than samples in air (Figure 3.6). The ultrasound probe enables large regions of the sample to be scanned. Using virtual touch imaging quantification (VTIQ), regions within the image can be selected for further quantitative analysis (Figure 3.6), and within these regions, quantitative values can be obtained within regions of $\sim 3 \times 3$ mm. The transducer measures the displacement of the B-mode representation due to an acoustic push pulse, in order to determine the shear wave speed ν_s. The shear wave speed was measured from n points within each sample and used with the gel density, ρ (calculated using the biphasic ideal mixing model and assuming negligible contribution of TiO_2) to determine the shear modulus, G:

$$\nu_s = \sqrt{\frac{G}{\rho}} \tag{3.3}$$

Due to the high water content of the gels, Poisson's ratio was taken to be 0.5 [14], giving rise to the relation $E = 3G$, enabling the Young's modulus E to be determined.

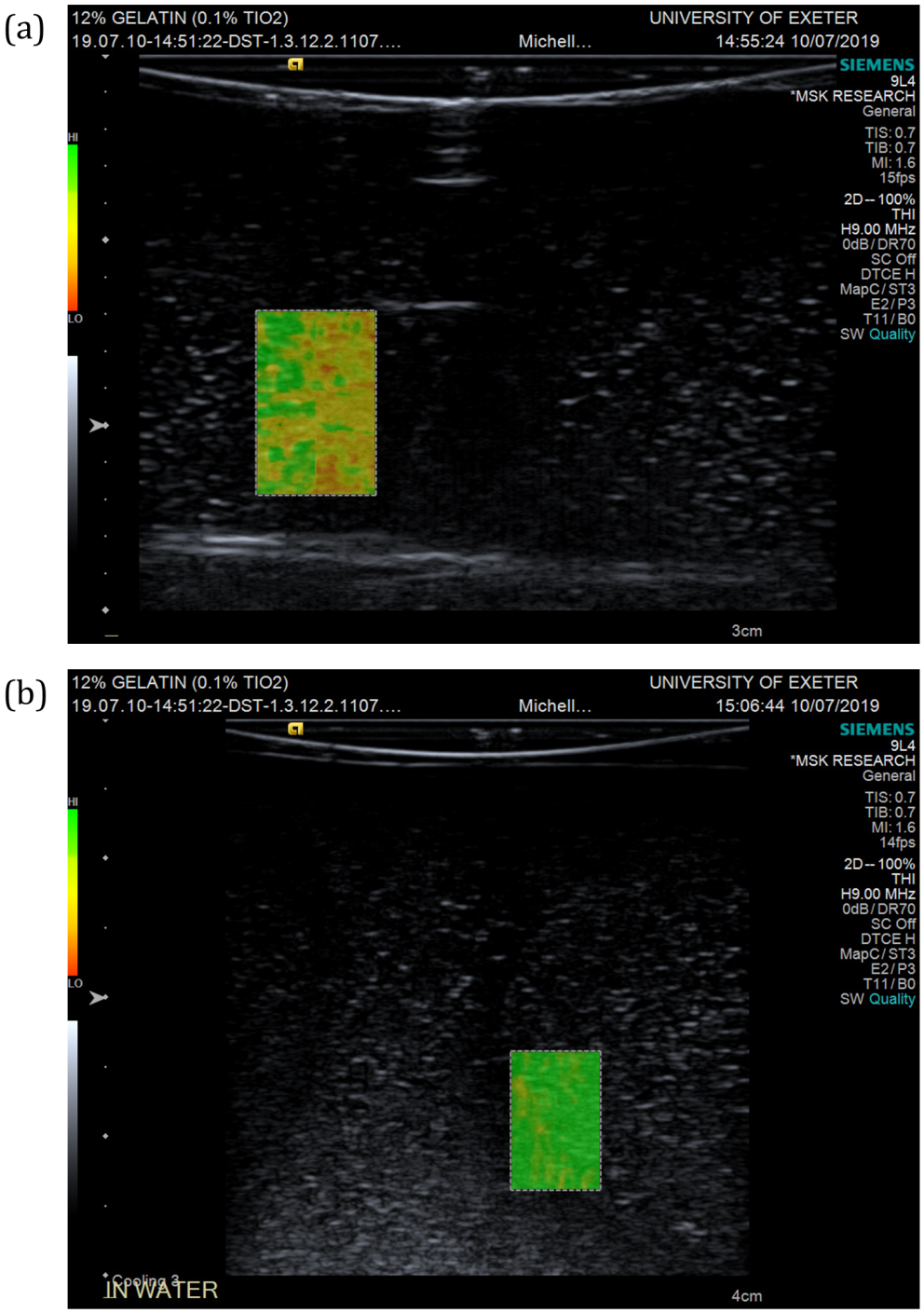

Figure 3.6.: *Example ultrasound B-mode image with quality map overlaid for a region within a 12% gelatin (a) in air, and (b) submerged in water. The quality map follows a traffic light scale, with regions of high quality marked in green, and regions of low quality in red.*

3.5. Brillouin Spectroscopy

3.5.1. TFPI-based Brillouin spectroscopy

Brillouin spectrometer

Brillouin spectra were acquired using a high contrast tandem Fabry-Pérot (TFP-2 HC) interferometer system [101], with a 532 nm continuous wave laser. The spectral resolution was 135 MHz and contrast was >150 dB. The scattered light was collected in both backscattering (180°) and 45° geometries (Figure 3.7). In both cases,

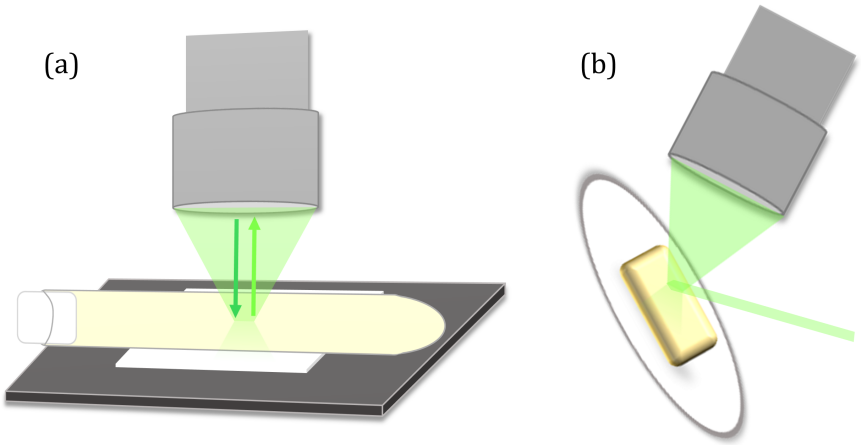

Figure 3.7.: *Schematic representation of (a) backscattering (180°) and (b) 45° scattering geometries. Samples are held in glass vials for backscattering geometry, and spread thinly over a reflective substrate for 45° scattering geometry.*

the scattered light was split by a short-pass tunable edge filter, which transmitted the quasi-elastically scattered light to the Brillouin spectrometer and reflected the inelastic light to a Raman spectrometer.
Unless otherwise stated, spectra were acquired at room temperature (20 ± 1°C), and it was assumed that the gels were not subjected to any significant local heating from the laser, since no visible change or damage occurred, and measurements conducted at different depths within the gel gave the same results.

Backscattering geometry (TFPI-180):
Incident light was directed to the sample by a 20× (NA 0.42) Mitutoya objective, which was also used to collect the backscattered light (Figure 3.7a). The power at the sample was a few mW, and the acquisition time was 17 s per spectrum.

45° scattering geometry (TFPI-45):
The sample was placed at a 45° angle to the incident light (Figure 3.7b) which was focused by an achromatic lens (NA 0.033), also used for collection of the scattered light. The power at the sample was ∼35 mW. Both bulk and parallel-to-surface acoustic modes were detected in this geometry.

Spectral acquisition

High Hydration:
Hydrogels prepared up to the solubility limit (18%) were transferred to glass vials, and the measurements were conducted in triplicate from different spatial locations within the sample, using a backscattering geometry with 180° scattering angle (Figure 3.7a) and with a total acquisition time of ∼ 17 s. At two concentrations, 10 and 20% polymer, measurements were also conducted as a function of temperature. A water bath was used to vary the temperature of the hydrogels from 65°C down to 4–5°C, to encompass the sol-gel transition. Spectra were acquired using JRS GHOST software, and Brillouin peaks were analysed using a damped harmonic oscillator (DHO) function [32, 162] in the range 7–9 GHz. Average fit parameters from Stokes and anti-Stokes peaks were obtained after deconvolution of the instrumental response function (performed using JRS GHOST software through fitting of the Rayleigh peak for each spectrum).

Low Hydration:
For Brillouin measurements during gelatin dehydration, a 45° scattering geometry was employed (Figure 3.7b). A drop of 20% w/w gelatin hydrogel was spread thinly (200–300 μm thickness) on a reflective silicon substrate, which was then mounted on an analytical scale (Sartorius BL210S) to measure the change in concentration during the measurements. Brillouin spectra were collected every few minutes for ∼2 hours with an acquisition time of ∼ 2.5–10 s.

3.5.2. VIPA-based Brillouin spectroscopy

A lab-built dual-VIPA (Virtually Imaged Phase Array) spectrometer, coupled to an inverted microscope was used for VIPA measurements. The system is described in full in Chapter 6, but briefly, a 532 nm laser was employed and an exposure time of 0.01–5 s was used for spectral acquisition. A fit to a Lorentzian function was applied

to extract the Brillouin frequency shift and linewidth from the spectra, and methanol and distilled water samples were used for calibration.

3.5.3. Longitudinal elastic moduli

The storage modulus M' was derived from the Brillouin frequency shift ω_B through the relation

$$M' = \left(\frac{\lambda}{4\pi}\right)^2 \frac{\rho}{n^2}\omega_B^2 \tag{3.4}$$

where $\frac{\lambda\omega_B}{4\pi n} = v$ is the acoustic wave velocity, λ is the excitation wavelength (532 nm), and ρ and n are the mass density and refractive index of the medium, respectively. Equation (3.4) shows that there is a direct relation between the real part of the longitudinal modulus and the square Brillouin shift, through the ratio ρ/n^2. In a similar way, the loss modulus M'' can be derived from the Brillouin frequency shift ω_B and linewidth Γ_B

$$M'' = \left(\frac{\lambda}{4\pi}\right)^2 \frac{\rho}{n^2}\omega_B\Gamma_B. \tag{3.5}$$

Note that Equations (3.4) and (3.5) are valid for backscattering geometry, and the Brillouin shift is expressed in units of angular frequency.

3.6. Raman Spectroscopy

3.6.1. Raman Spectrometer

Two Raman systems, with incident light of different wavelengths, were used throughout this work. The two different systems have complementary sensitivities to the lower (fingerprint) and higher (C-H stretching) regions of the spectrum. In particular, the Horiba spectrometer is part of a dual Brillouin-Raman system, enabling simultaneous measurement of Brillouin and Raman spectra.

inVia Raman microscope

A Renishaw inVia confocal microscope with a long working distance 50× (NA 0.50) objective was used with an 830 nm laser. The backscattered light was dispersed through a 600 lines/mm grating and detected by a back-illuminated, deep-depletion CCD camera. A spectral range of 370–2345 cm^{-1} was used, which covered the entire

fingerprint region of the spectra. (Note that measurements below 370 cm^{-1} are prevented by a prominent peak due to the CaF_2 substrate (321 cm^{-1}), and edge filter cutoff at ca. 200 cm^{-1}.)

Horiba Raman spectrometer

A Horiba iHR320 Triax Raman spectrometer was used with a 532 nm laser and a microscope equipped with a 20× (NA 0.42) Mitutoyo objective. As described in Section 3.5.1, the backscattered light was split by a tunable edge filter, which transmitted the quasi-elastically scattered light, and reflected the remaining light to the Raman spectrometer, where it was reflected and dispersed through a 600 lines/mm grating onto a CCD camera.

3.6.2. Spectral Acquisition

Hydrogels up to the solubility limit

inVia Raman microscope:
Hydrogels were prepared to concentrations between 4 and 18% as previously described (Section 3.1) and left to set in cylindrical moulds. Prior to measurement, gels were removed from the mould and transferred onto a Raman-grade polished calcium fluoride slide (Cystran, UK). Raman spectra were acquired with an exposure time of 7 s per spectrum and 32 accumulations. To avoid changes in the focus at the surface of the gel due to dehydration over time, spectra were collected from approximately 50 µm below the gel surface and from three different locations across the sample. WiRE v.4.0 software was used for all data acquisition.

Horiba Raman spectrometer:
Hydrogels were left to set in sealed glass cuvettes, where they remained for Raman measurements. Spectra were acquired with an exposure time of 1 s and 60 accumulations, with a power at the sample of approximately 15 mW. Five Raman spectra were collected at different locations within the sample and LabSpec5 software was used for data acquisition.

Thin film dehydration

The Renishaw inVia confocal microscope previously described (Section 3.6.1) was used to measure the Raman spectra during the dehydration of a thin film of gelatin. Two thin films of gelatin were prepared on a Raman-grade calcium fluoride substrate (Cystran, UK), as described in Section 3.1. The focal point was set to the interface of the CaF_2 substrate and the hydrogel. A slightly thicker film of gelatin was also prepared by removing a thin slice of gelatin from the centre of a larger gel (20% w/w). The hydrogel slice ($\sim$ 2 mm thickness) was placed on a Raman-grade calcium fluoride slide and the focal point was set to the gel surface for measurement. Spectra for both thin and thick films were acquired every 2–4 min, with an exposure time of 2.5 s and 16–24 accumulations. The focal point was adjusted prior to each measurement, and WiRE v.4.0 software was used for data acquisition.

3.6.3. Spectral Analysis

All Raman spectra were processed in Matlab using custom written scripts. Spectral pre-processing (Figure 3.8) was performed in three steps: (i) cosmic ray removal, (ii) baseline subtraction, and (iii) normalisation.

Cosmic rays were identified as spikes in the spectra and were replaced with the median of the nearest neighbours. The baseline of each spectrum was determined using an asymmetric least squares method [163], which was then subtracted from the raw spectra. Finally, each spectrum was normalised to its Euclidean norm.

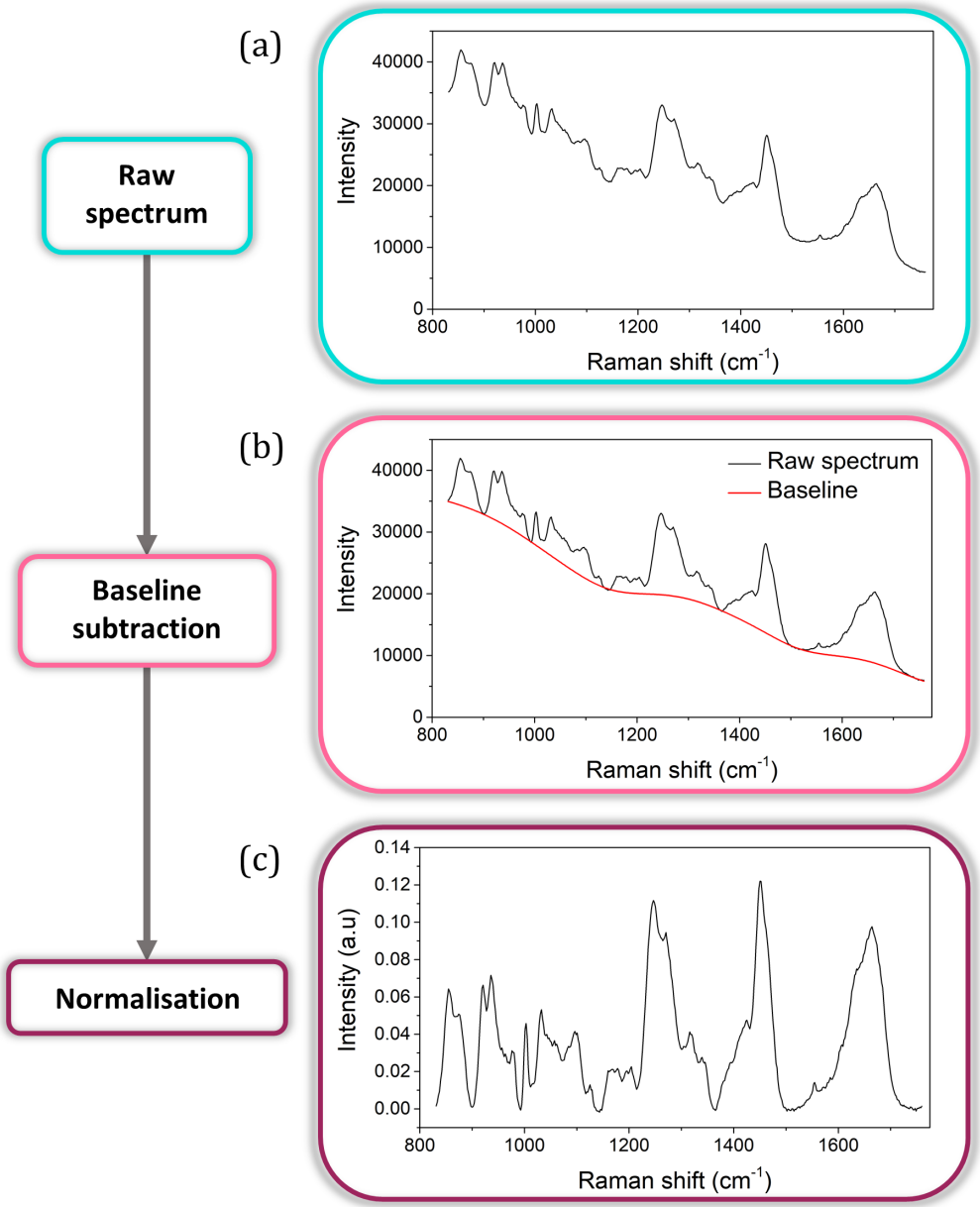

Figure 3.8.: *Data processing for an 18% gelatin hydrogel. (a) Raw Raman spectrum. (b) Baseline (red) is determined by asymmetric least squares fit to raw spectrum (black). (c) Spectrum is normalised through division by its Euclidean norm.*

3.7. Rule of Mixtures

The spatial resolution of Brillouin measurements is limited to the phonon length scale in the material under investigation. Inhomogeneities that occur on a smaller spatial scale than the mean free path of the phonon ($\sim$ 2.1 µm for water [117]) will not be resolved but will give rise to heterogeneous broadening of the Brillouin peak [69]. This is the case for the gelatin hydrogels studied here, where cryo-SEM images (Figure 3.2) show the presence of pores ranging between $\sim$ 2 and 0.2 µm in diameter for gels containing 4–18% solute. From this perspective, it is reasonable to apply effective medium modelling to the measured storage moduli of the gels.

The material properties of a composite material can be modelled as a weighted combination of the properties of its components. Derived from Hooke's law, the elastic modulus can be modelled assuming constant strain (Voigt model) or constant stress (Reuss model), providing an upper and lower bound, respectively, for the elastic modulus of the material. For a fibrous material, the Voigt model assumes that the force is applied in a direction parallel to the fibres (Figure 3.9a), resulting in a constant strain along the fibres and surrounding matrix. On the other hand, the Reuss model

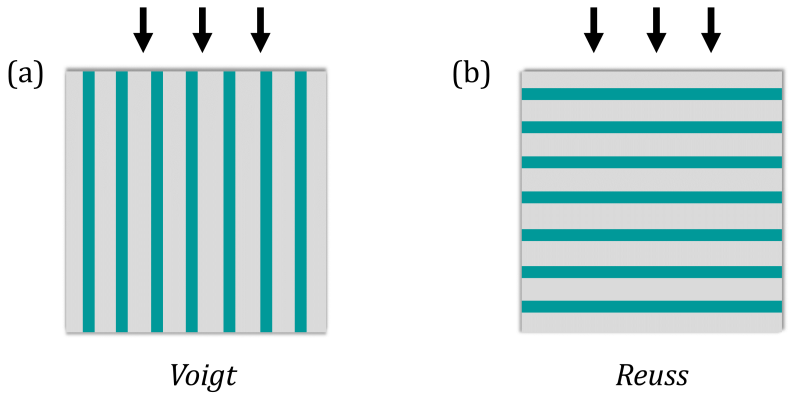

Figure 3.9.: *Schematic representation of a fibrous material, where force is applied (a) parallel to the direction of the fibres (Voigt model) and (b) perpendicular to the fibres (Reuss model).*

assumes that the force is applied orthogonal to the fibre axis (Figure 3.9b), resulting in constant stress across the composite [164, 165]. Applying this theory to the Brillouin-derived storage modulus M' of gelatin hydrogels, the Voigt model:

$$M' = \epsilon M'_f + (1 - \epsilon) M'_s \tag{3.6}$$

provides an upper bound for the total modulus, whilst the Reuss model:

$$\frac{1}{M'} = \frac{\epsilon}{M'_f} + \frac{(1-\epsilon)}{M'_s} \tag{3.7}$$

gives the lower bound in these relations. ϵ is the volume fraction of water (the fluid component of the gel) and M'_f and M'_s are the moduli for the fluid and solute components, respectively. Of course hydrogels are not fibrous, with the solid component dispersed throughout the fluid (Figure 3.2), so neither model is expected to suit the material perfectly and should just be taken as an approximate lower and upper bound for the moduli.

4. Brillouin-derived viscoelastic properties of hydrogels with a TFPI

The following chapter contains sections from the publication "Viscoelastic properties of biopolymer hydrogels determined by Brillouin spectroscopy: A probe of tissue mechanics" [1].

4.1. Introduction

Tissue phantoms are a useful tool for the demonstration and testing of instruments and techniques. They can provide simplistic models of biological tissue, and the complexity can be adjusted as required through the addition of cells or fibres. As well as being relatively cheap and easy to produce in a variety of shapes and sizes, gelatin provides a homogeneous medium for testing, where the concentration, and therefore mechanical properties, can be tuned as desired. Gelatin is a homogeneous, aqueous gel and is derived from the breaking of the triple-helical structure of collagen [152, 166]. As well as adjusting the hydration, the mechanical properties of gelatin can also be controlled by the addition of chemical cross-linkers such as formaldehyde or gluteraldehyde [166, 167]. The mechanical properties of gelatin with and without the addition of chemical cross-linkers have been studied at varying water concentrations through stress-strain testing [166, 168, 169], and has been shown to approximate the properties of soft tissues adequately [167, 169].

This chapter presents measurements of gelatin hydrogels using a commercially available tandem Fabry-Perot interferometer (TFPI), and aims to explore the information content of the Brillouin spectrum of gelatin (denatured collagen). Correlative compressive testing and Raman spectroscopy are also used, with the intention of further investigating the chemical and macro-mechanical properties of the hydrogels. Tuning the polymer content of the hydrogels across a broad range (0–80% w/w polymer), it is possible to cover a wide range of static and dynamic macroscopic mechanical moduli that replicate those of many biological tissues.

4.2. High hydration

Brillouin measurements conducted in backscattering geometry.

4.2.1. Gelatin macro-mechanics

Compressive testing

Gelatin hydrogels were prepared at varying concentrations to tune their mechanical properties, as measured by uniaxial compressive testing. Compressive testing was applied to hydrogels of 4–18% polymer concentration, resulting in stress-strain plots (Figure 4.1a) for each measurement. A linear fit was applied to the data to determine the Young's modulus. The Young's modulus was found to increase with increasing

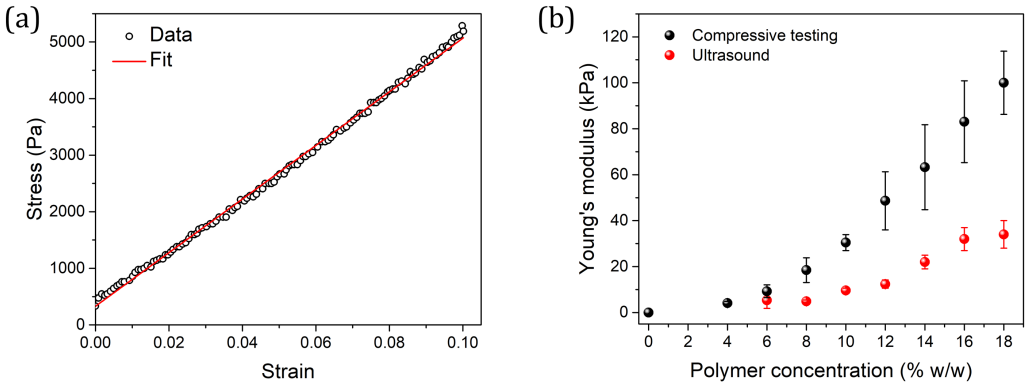

Figure 4.1.: *(a) Stress-strain plot of a* 12% *gelatin sample. Linear fit yields the Young's modulus (*47.4 ± 0.2 *kPa). (b) Plot of Young's modulus versus polymer concentration from compressive testing measurements (black) and ultrasound elastography (red). Error bars denote the standard deviation across three successive measurements at different spatial locations.*

polymer concentration (Figure 4.1b), ranging up to $\sim$ 100 kPa.

Ultrasound elastography

Ultrasound elastography operates at MHz frequencies, so is at an intermediate frequency regime between low frequency (Hz) compressive testing, and high frequency (GHz) Brillouin spectroscopy. In addition to this, it also gives a closer representation of how stiffness is used as a contrast mechanism in the clinical environment. Gelatin

hydrogels of 6–18% polymer were measured using a Siemens S3000, which gave values for the Young's modulus for regions of $\sim 31 \times 3$ mm within the sample.

Values of the shear wave velocity were used to determine the Young's moduli of the hydrogels (red dots in Figure 4.1b), which were found to follow the same trend as those calculated from compressive testing measurements. Although both sets of results had a similar order of magnitude, those from ultrasound elastography were slightly lower than the compressive testing results. This is likely due to inhomogeneity in the distribution of the scattering agent, and poor reflectivity of the TiO_2, resulting in discontinuity in where shear wave propagation is measured within the sample. In addition to this, the way in which the transducer was used may also have contributed to this discrepancy. In order to keep the measurements between samples consistent, the probe was held in position with a clamp. However, the transducer is sensitive to the angle of insonation and the pressure which is applied to it. Subtle adjustments in pressure and the angle of the probe can improve the image quality and result in better shear wave transmission. Experienced users would adjust the pressure on the probe and angle of insonation accordingly to get the highest quality image for each measurement, however, with the probe secured in place this was not possible.

4.2.2. Brillouin-derived mechanics

Brillouin spectra of gelatin hydrogels contain a single sharp peak (with Stokes and anti-Stokes components; Figure 4.2a), indicating that the gels are homogeneous on the phonon wavelength scale (ca. 0.3 μm for 532 nm excitation).

With increasing polymer concentration, there is an increase in both the Brillouin frequency shift, ω_B, and linewidth, Γ_B (Figure 4.2b), in line with previous observations [25, 40]. The values of ω_B and Γ_B were derived from fitting the peaks to a damped harmonic oscillator (DHO) function (Figure 4.2c), and plotted as a function of polymer concentration in Figure 4.2d. An observed Brillouin shift of the order of 8–9 GHz reproduces well what has been observed for the cornea in highly hydrated conditions [170]. Measurements of the refractive index (Figure 4.3a) and calculation of the density (based on the ideal mixing model; see Chapter 3) of the gels verified the Lorentz-Lorenz relation [171] for the samples tested (Figure 4.3b). Indeed, the deviation from a constant trend observed here was $< 1\%$, validating the approximation of uniform ratio made in many Brillouin scattering investigations. This confirms

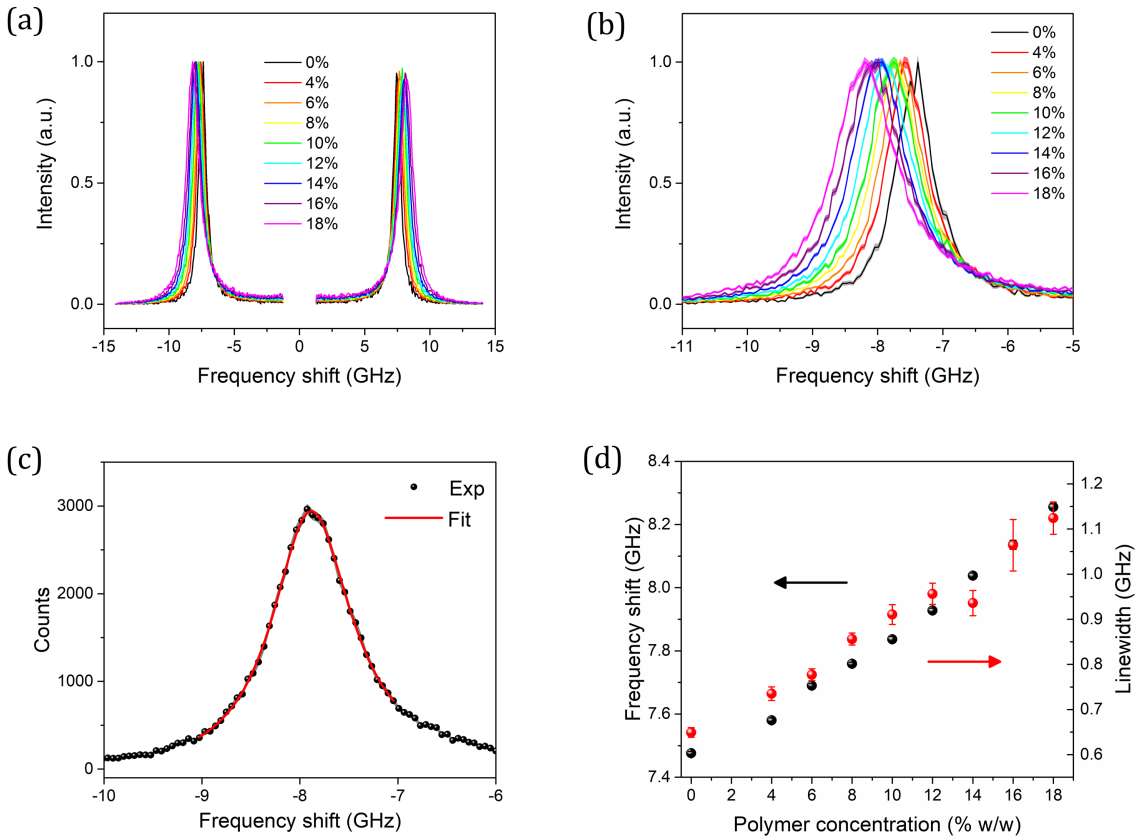

Figure 4.2.: *(a) Brillouin spectra and (b) Stokes peak for all gelatin concentrations, normalised to the Stokes peak. Shading represents the standard error, i.e., square root of number of counts. (c) Results of a damped harmonic oscillator (DHO) fit to the maximum of the Stokes peak. (d) Plot of frequency shift and linewidth of gelatin hydrogels versus polymer concentration. Full symbols denote experimental data, and error bars represent the fit error.*

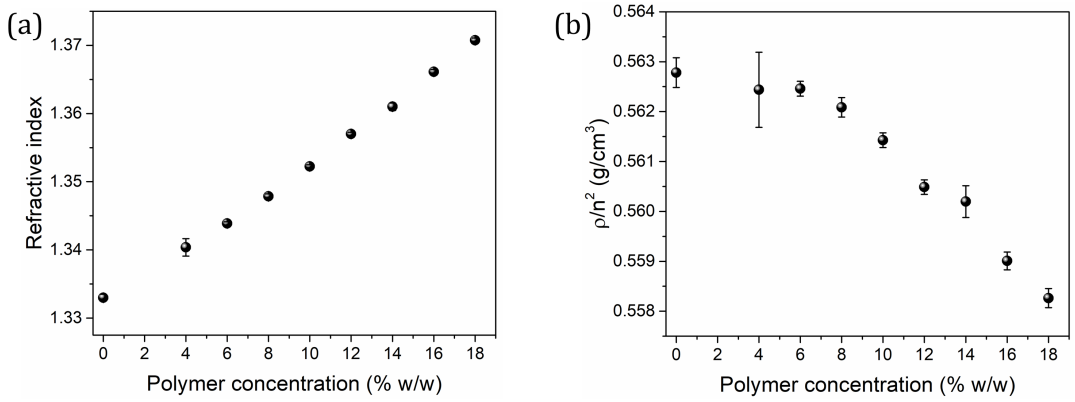

Figure 4.3.: *(a) Measured refractive index for varying gelatin concentration. Error bars indicate the standard deviation for four measurements on different gels. (b) Plot of the density-to-refractive index square ratio vs. polymer concentration, with a maximum change of* 0.8%.

that the changes in ω_B and Γ_B are unambiguously assigned to an increase in storage and loss moduli (Figure 4.4a), and that changes are predominantly due to the mechanics.

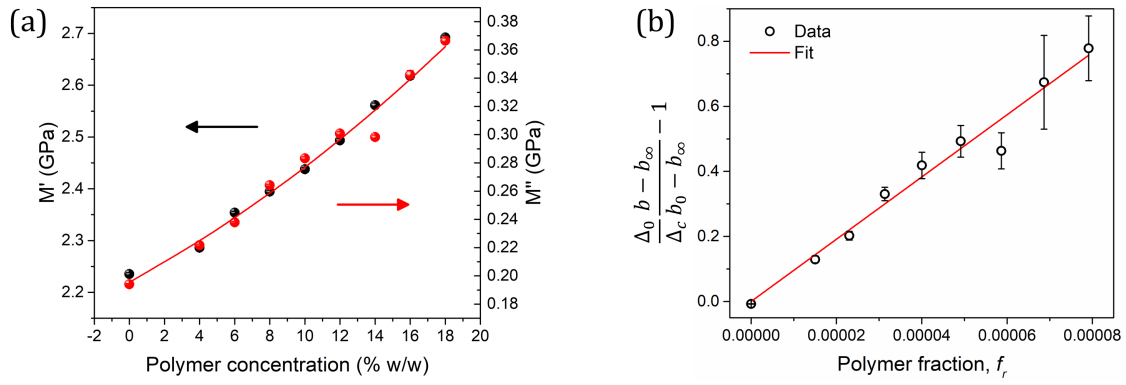

Figure 4.4.: *(a) Plot of the storage and loss moduli versus polymer concentration. Full symbols denote experimental data, and error bars represent the fit error. Red line denotes the linearised model derived from (b) and described in Section 4.2.2. (b) Plot of equation (4.2) (empty circles) versus polymer concentration and linear fit (red line) giving a gradient of* $N_h(\epsilon - 1) = 9566$.

The Brillouin linewidth was identified as being most affected by change in polymer concentration, leading to an 89% increase in loss modulus between 0 and 18% polymer (Figure 4.4a), which reflects variations in the microscopic viscosity of the gel. This variation is attributed to the restricted mobility of water, particularly in the first hydration shell of the polymer molecules. In comparison, the evolution in storage modulus shows only a 20% increase. This is to be expected since the modulus of the water is high (2.2 GPa) and the addition of polymer molecules produces only a small effect. This result shows that, in this system, the Brillouin frequency shift is sensitive to the presence of the polymer network and, furthermore, that the modulus of the network can be determined, provided that the spectrometer has adequate resolution.

Linearised model

When the system is in a liquid-like state (as is the case for water and diluted aqueous solutions), the molecular relaxation occurs on a picosecond time scale, i.e., at much higher frequency than that of the Brillouin peak. This gives rise to a linear relationship between the loss modulus and frequency, $M''(\omega) = \omega b$, where the linewidth

of the Brillouin peak Γ_B yields the "longitudinal" kinematic viscosity b of the liquid through the relationship $b = \rho\Gamma_B/q^2$, where q is the exchanged wave vector, as defined in Chapter 3. The longitudinal kinematic viscosity can give information on the characteristic times of molecular relaxations. For a highly diluted hydrogel, water can be considered as having two phases; "free" (or bulk) water, and "hydration" water (interacting more strongly with the polymer chains). In this state, the observed increase in Γ_B or M'' with increasing polymer concentration (Figure 4.2d and Figure 4.4a) can be attributed to an increase in b due to two contributions; one from bulk and the other from (retarded) hydration water, which increases linearly with polymer concentration.The longitudinal kinematic viscosity can then be written in terms of the characteristic relaxation times τ_h and τ_b of the hydration and bulk water, respectively:

$$b = \Delta_c[\alpha\tau_h + (1-\alpha)\tau_b] + b_\infty \tag{4.1}$$

where α is the fraction of relaxation strength associated to hydration water, b_∞ accounts for contributions to viscosity that are fast (instantaneous) relative to the picosecond time scale investigated by Brillouin scattering, and Δ_c is the total relaxation strength of the solution at each polymer concentration, given by relaxed (c_0) and un-relaxed (c_∞) sound velocities through the relationship: $\Delta_c = c_\infty^2 - c_0^2$. Assuming that the relaxation strengths of the two processes are proportional to the relative fractions of hydration and bulk water, α can be expressed as $\alpha = f_r N_h$, where f_r is the fraction of polymer-to-water molecules and N_h is the hydration number. Hydration water molecules are typically found to diffuse more slowly than bulk molecules, and the retardation parameter $\epsilon = \tau_h/\tau_b$ is used to quantify this effect. Equation (4.1) can therefore be rearranged to give:

$$\frac{\Delta_0}{\Delta_c}\frac{(b-b_\infty)}{(b_0-b_\infty)} - 1 = N_h(\epsilon-1)f_r \tag{4.2}$$

where b_0 and Δ_0 are the kinematic viscosity and relaxation strength of pure water, with c_0 obtained from the frequency position of Brillouin peaks and $c_\infty = 2860$ ms^{-1} measured by inelastic x-ray scattering (IXS) [172] and assumed to be independent of polymer concentration [173]. $b_\infty = 2.99 \times 10^{-3}$ cm^{2}s^{-1} was derived from IXS measurements [172]. Figure 4.4b shows well defined linear behaviour of $\frac{\Delta_0}{\Delta_c}\frac{(b-b_\infty)}{(b_0-b_\infty)} - 1$ versus f_r across the whole range of polymer molecular fraction. A linear fit to the data gives $N_h(\epsilon-1) = 9566(\pm 290)$. Using geometrical arguments and modelling the collagen molecule as a rod with a radius of 0.36 nm and a length of 300 nm [174], the hydration number, N_h can be estimated as the number of water molecules

(number density $\rho = 33.37 \times 10^{27}$ m^{-3}) within 3.1 Å of the triple helix surface, giving $N_h = 10071$. From this value (and $N_h(\epsilon - 1) = 9566$), the retardation factor $\epsilon = 1.94(\pm 0.03)$ can be deduced for hydration water. Of course, this value is based on the approximation that collagen molecules are perfectly cylindrical rods, but nevertheless $\epsilon = 1.9$ is in the range previously found for hydrophobic hydration in a large class of biomimetic molecules [137, 173]. The close agreement between the prediction of this two-step relaxation model and the measured concentration dependence of Brillouin parameters (red line in Figure 4.4a), together with the adequate value obtained for the retardation of hydration water, supports the view that water forming the first hydration shell of collagen molecules has a great impact on the dynamics of these hydrogels, thus affecting the viscosity and loss modulus far more than the elasticity and storage modulus.

4.2.3. Gelation

The Brillouin frequency shift is so sensitive to the elastic properties of the gelatin network that it reveals the onset of a sol-gel transition, which arises from the development of a percolative cluster involving a population of cross-linked gelatin molecules. This phenomenon was observed by investigating two different gelatin concentrations, 10 and 20%, as a function of temperature. The sol-gel transition gives rise to a small

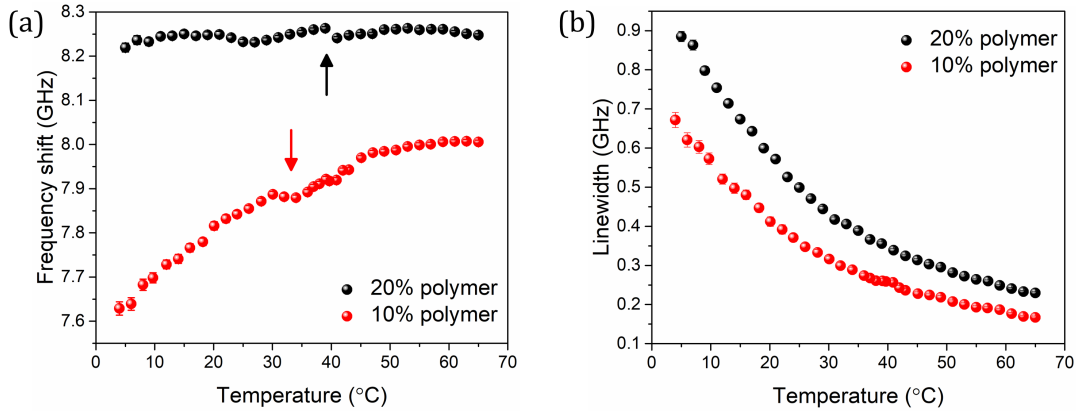

Figure 4.5.: *Evolution of (a) frequency shift and (b) linewidth derived from Brillouin spectra of hydrogels as the temperature is reduced from 65 to 4–5° C. Arrows indicate the gel transition.*

"step" gradient of the frequency shift (see arrows in Figure 4.5). In contrast, the plot of linewidth as a function of temperature shows no discontinuity at the gel transition point (Figure 4.5b). This is consistent with the fact that a large fraction of the

molecules are still in the liquid phase and their diffusive motion dominates the picosecond dynamics. This gives rise to the broadening of the Brillouin spectra in both liquid and gel phases. The solid-like portion of the sample, composed of cross-linked gelatin molecules (Chapter 3, Figure 3.1b), is responsible for the relaxation process occurring at very long time scales (hundreds of seconds or more), and this gives rise to a divergence of the "static" viscosity and the onset of shear (G) and Young's (E) moduli. The small number of molecules involved in this process is responsible for the small jump in the value of M', revealed in Figure 4.5a. The liquid fraction of the sample is almost unchanged by the gelation process and is still responsible for the high-frequency (picosecond) relaxation, which is comparable to that of diluted solutions, demonstrated by a smooth transition in M'', as shown in Figure 4.5b.

4.2.4. Chemically cross-linked gelatin

Brillouin spectroscopic measurements

The effect of chemical cross-linking was investigated by the addition of formalin to the gels. Increasing the concentration of formalin in a 10% gelatin hydrogel leads to an increase in the Brillouin frequency shift, with a small gradient discontinuity at $\sim 8\%$ formalin (Figure 4.6a). This behaviour is also seen in the linewidth (Figure 4.6b), albeit more subtly.

Formalin is an aqueous solution of formaldehyde (37% w/w formaldehyde), so by tuning the concentration of formalin in the gels, the water content is also changing slightly. Plotting the Brillouin frequency shift (Figure 4.6c) and linewidth (Figure 4.6d) as a function of water content for gels with and without formalin shows no significant difference in the linewidth due to the addition of formalin. There is, however, a small deviation in the frequency shift for gels containing formalin. As formalin concentration is initially increased (0–6% formalin) there is a more rapid increase in frequency shift (see red dashed line in Figure 4.6c), compared to that of gels without formalin. Beyond this point, the frequency shift reaches a plateau (as seen in Figure 4.6a), before increasing again, at a slower rate to that initially observed. However, upon visual inspection, a small amount of excess liquid was observed on the surface of gels with higher formalin concentrations, suggesting saturation had been reached. Therefore, the true water content of the gels is probably slightly lower than that predicted in Figure 4.6c–d.

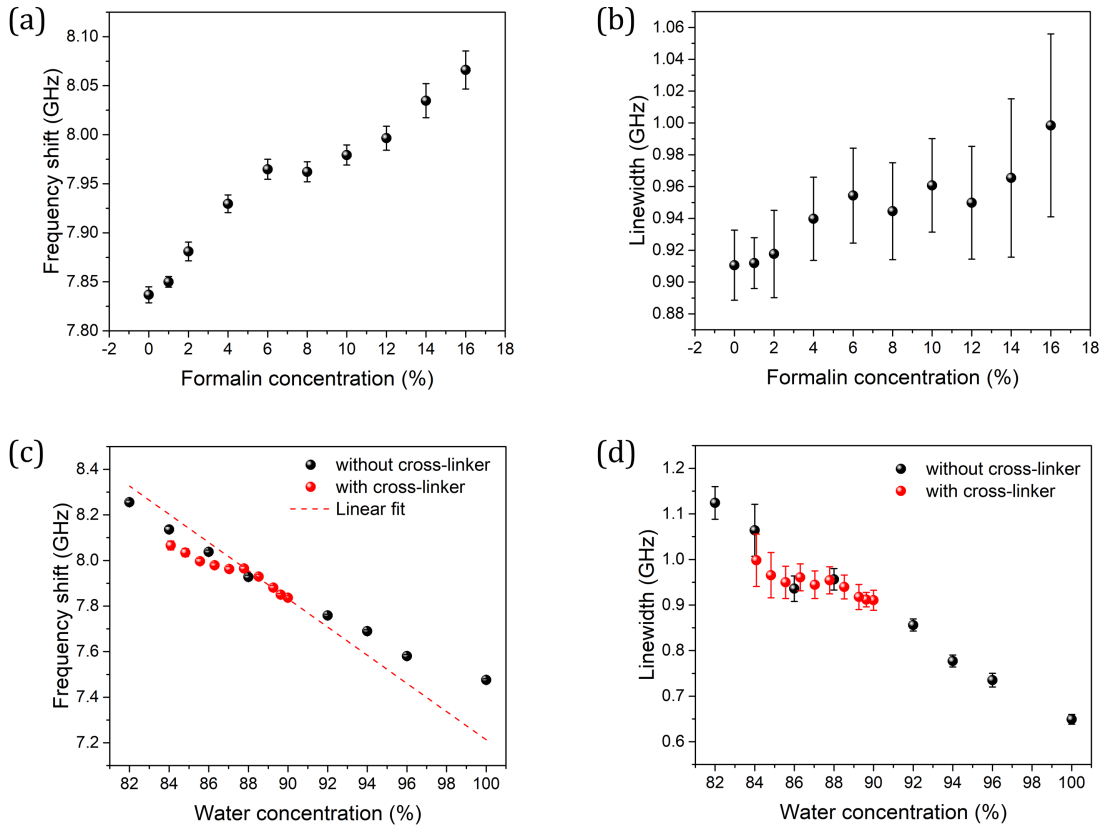

Figure 4.6.: *Brillouin frequency shift (a) and linewidth (b) as a function of formalin concentration. Evolution of (a) frequency shift and (b) linewidth as a function of water concentration, for gels with (red dots) and without (black dots) chemical cross-linker (formalin). Red dashed line in (c) is an extrapolated linear fit to data points corresponding to* $0-6\%$ *formalin concentration, and serves as a guide for the eye.*

Raman spectroscopic measurements

Raman spectra of gels of varying formalin concentrations enable further interpretation of the molecular changes. Figure 4.7a shows the evolution in Raman spectra as formalin concentration is increased. The Raman spectrum of pure formalin shows two distinct peaks centred at 912 and 1058 cm^{-1}, assigned to symmetric and anti-symmetric C-O stretching modes, respectively [175, 176]. As the formalin concentration is increased, a peak emerges at $\sim$ 1037 cm^{-1} for 2–10% formalin gels, and $\sim$ 1045 cm^{-1} for 12–16% formalin, showing a blue-shift with increasing formalin concentration. The difference spectra (calculated with respect to a 10% gelatin containing no formalin) highlights this change, with the emergence of a peak centred at $\sim$ 1040 cm^{-1} (Figure 4.7b). Integrating this peak and plotting the result as a function of formalin concentration (Figure 4.7c) shows an increase in the area under the peak with increas-

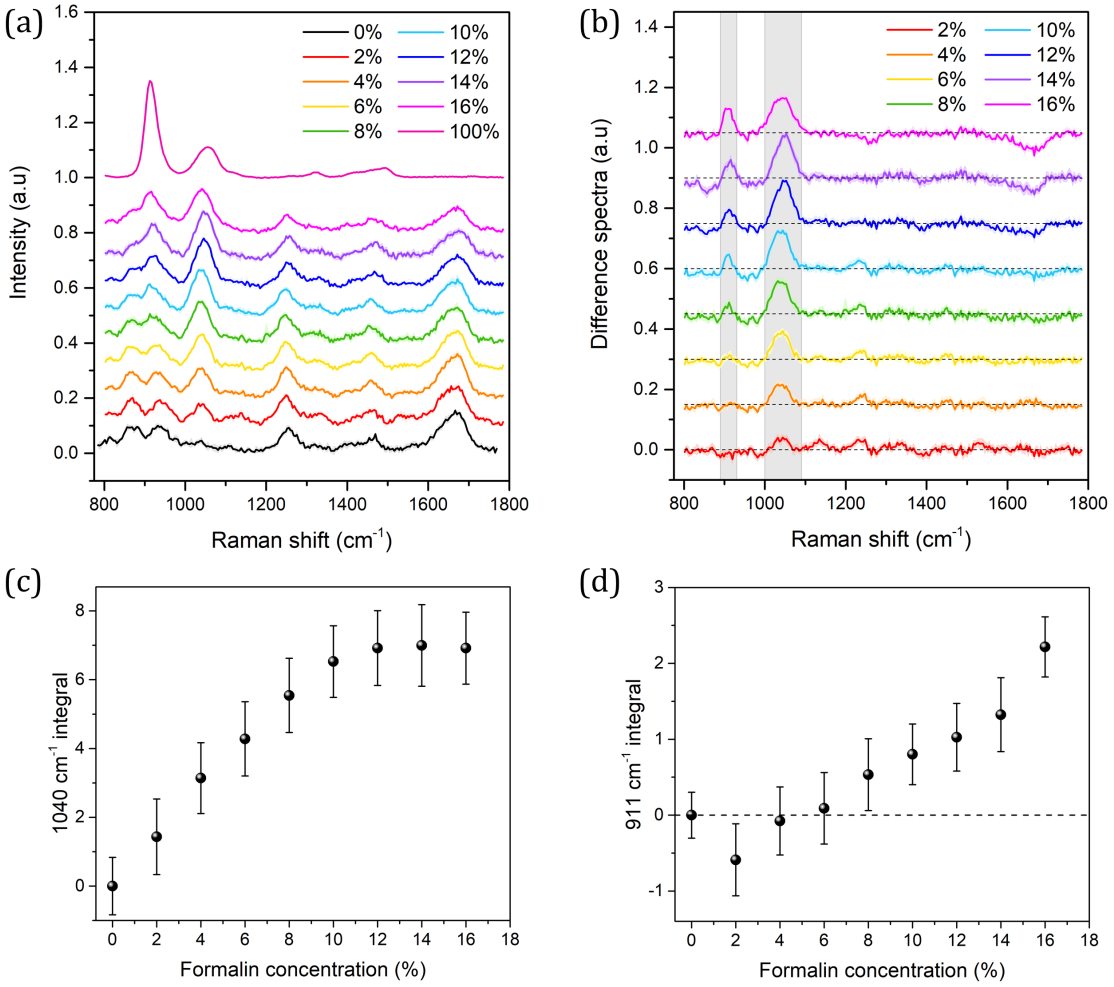

Figure 4.7.: *(a) Raman spectra for a 10% gelatin sample with varying concentrations of formalin (0–16%) and spectrum of pure formalin (top). (b) Difference spectra, calculated with respect to 0% formalin gel (10% gelatin). Grey shaded regions encompass the peaks at ∼ 911cm^{-1} and ∼1040 cm^{-1} (areas plotted in (c) and (d), respectively). (c) Integrated intensity of the formalin peak at ∼1040 cm^{-1} as a function of formalin concentration. (d) Integrated intensity of the peak centred at ∼ 911 cm^{-1} in the difference spectra as a function of formalin concentration. Shading on spectra (a,b) denotes the standard deviation in the normalised spectra across 3 sequential measurements at different spatial locations within the sample.*

ing formalin concentration, before a plateau is reached at ∼ 10% formalin. A peak at 1041 cm^{-1} has previously been identified as a formaldehyde contamination peak in fixed tissue samples [177], and a Raman band at 1030–1032 cm^{-1} has been assigned to pyridinium ring vibrations and found to increase in samples cross-linked with an aldehyde [178]. It's therefore plausible that the initial increase in peak intensity is due to the increased formalin concentration, with some contribution from pyridinium cross-links. At concentrations greater than 10% formalin the gel reaches saturation,

in line with the discontinuity in gradient seen in Figure 4.6c, which suggests that the gel reaches saturation between 8 and 10% formalin.

In addition to this, there is a change in shape of the doublet in the 835–980 cm^{-1} region, highlighted more clearly by the emergence of a peak centred at $\sim$ 911 cm^{-1} in the difference spectra calculated with respect to the non cross-linked gel (Figure 4.7b). The 835–980 cm^{-1} doublet is also present in the spectrum of the non cross-linked gel, and is explored as a function of gelatin concentration in Chapter 5, where it is found that the peak at 911 cm^{-1} is due to bound water within the gel. Integrating the peak at $\sim$ 911 cm^{-1} in the difference spectra and plotting as a function of formalin concentration (Figure 4.7d) shows an increase in the peak area with increasing formalin concentration. This peak has contributions from both the formalin (peak centred at 912 cm^{-1}; Figure 4.7a) and bound water. It is plausible that the increase in intensity beyond the formalin saturation point, observed in Figure 4.7c, is due to an increased proportion of bound water in the sample due to the decrease in overall water concentration (Figure 4.6c,d), however, the spectral resolution makes it difficult single out this contribution from that of the formalin.

4.2.5. Gelatin stability over time

To ensure stability and reproducibility of the gel samples, a selection of gelatin samples were studied over time up to approximately 24 h after gelation. Gelatin concentrations of 4, 10 and 18% polymer were used, to cover the entire concentration range, and Brillouin spectra were acquired every 10 min. Figure 4.8 shows that, although there are small changes in the Brillouin frequency shift during the first 12 h, both the frequency shift and Brillouin linewidth are approximately constant 24 h after preparation. Stability measurements were also carried out beyond the initial 24 h period (Figure 4.9) and showed that, whilst the gels were kept in sealed vials, the Brillouin frequency shift and linewidth stayed approximately constant for up to 12 days after initial preparation, suggesting that the seal was secure enough to prevent any significant dehydration during measurements.

4.3. Low hydration

Brillouin measurements conducted in 45° scattering geometry.

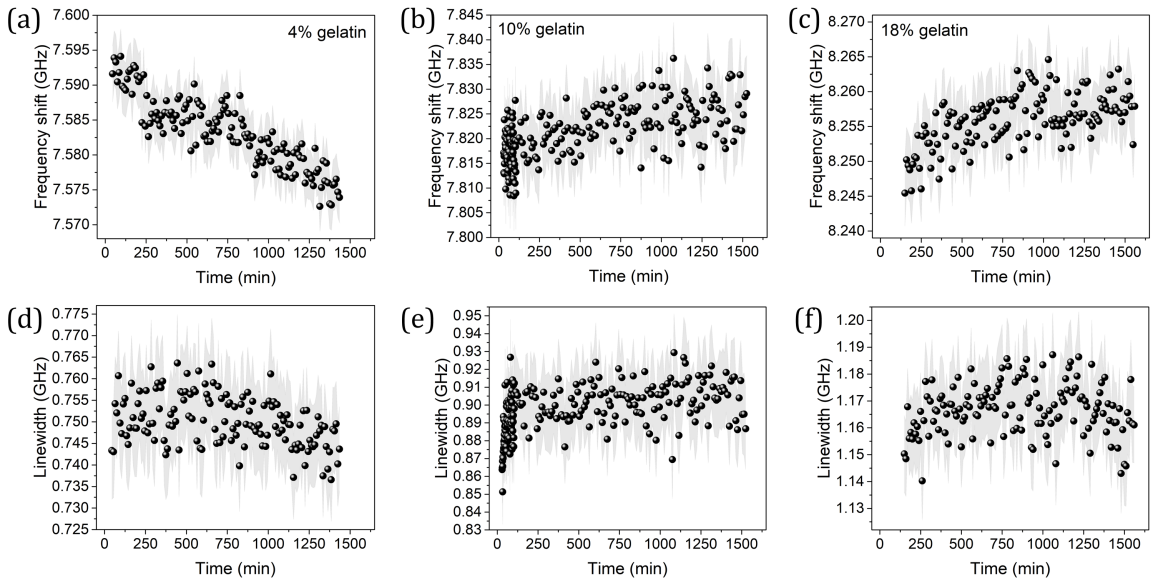

Figure 4.8.: *Evolution of frequency shift (a–c) and linewidth (d–f) over the first 24 hour period after gel preparation for (a,d) 4%, (b,e) 10% and (c,f) 18% polymer concentration. Shading denotes error in DHO fit.*

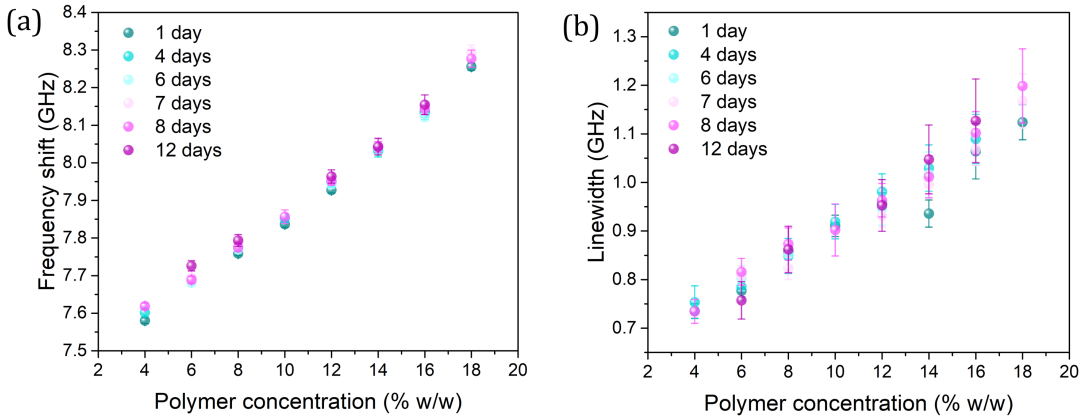

Figure 4.9.: *(a) Frequency shift and (b) linewidth as a function of polymer concentration measured at 1, 4, 6, 7, 8 and 12 days after gel preparation.*

As the water fraction in the gel is reduced, the dynamics of the residual water is increasingly coupled to that of the gelatin molecules, until an arrested (glassy) phase is reached. Note that this is also the mechanism responsible for the hardening of animal glue, one of the most widely used glues worldwide. In fact, the word collagen derives from the Greek “kolla”, glue. Due to the 45° scattering geometry employed, Brillouin spectra present peaks due to both the bulk (high frequency) and parallel-to-surface (low frequency) modes. The results of a DHO fit to the anti-Stokes component of each of these modes is shown in Figure 4.10 a and b. The transition from the liquid

phase (low elastic modulus) to the solid phase (high elastic modulus) is revealed by the sigmoidal trend in the frequency shift and the associated maximum in linewidth of the Brillouin peaks (Figure 4.10c). The frequency shifts measured in the case of

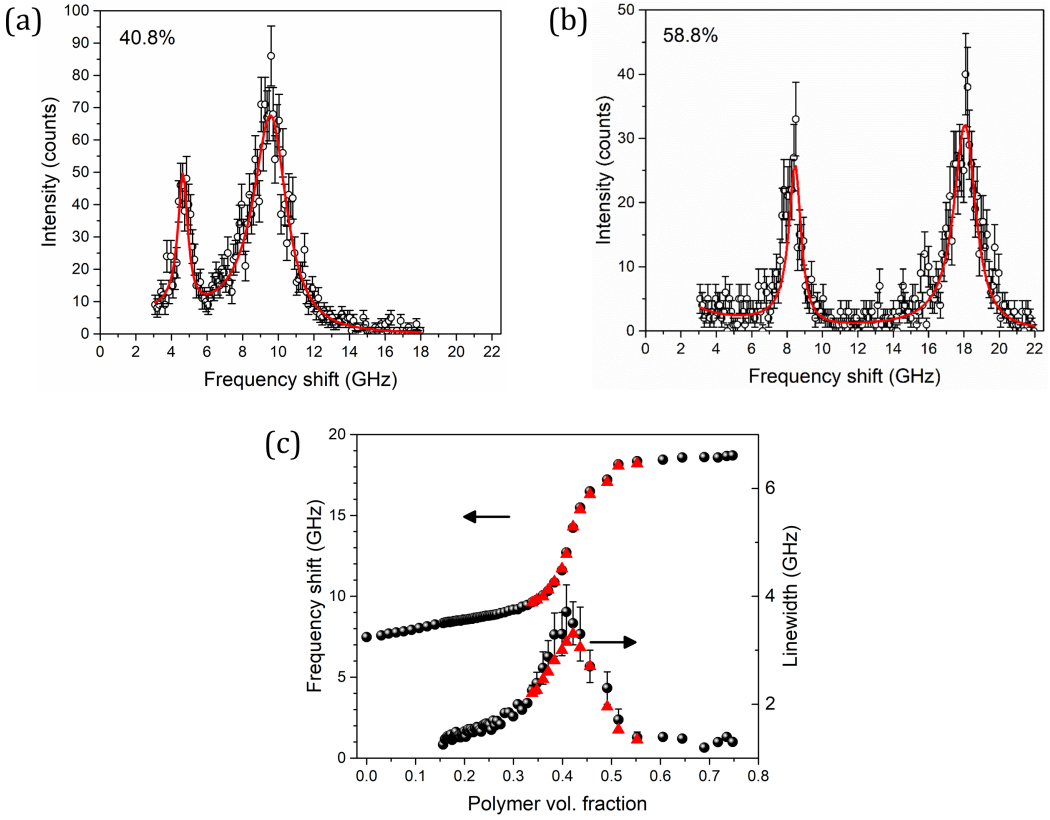

Figure 4.10.: *Results of DHO fitting applied to both bulk and parallel-to-surface modes for hydrogels at (a) 41% and (b) 59% polymer concentration. (c) (Top plot) Brillouin frequency shift and (bottom plot) linewidth of gelatin versus polymer volume fraction. The error bars encompass the range of values obtained from the fits, and the red triangles denote the frequency shifts and linewidths of the theoretical curves derived from a viscoelastic fit (Appendix A).*

liquid- and solid-like gels reproduce well the Brillouin response of articular cartilage [76], with a peak at 8 GHz characteristic of the soft component (disordered phase of thin, poorly oriented collagen fibres, proteoglycans and water) and a peak at 19 GHz related to the hard component (collagen fibre bundles). Hence, this hydrogel model system mimics both the soft component of cartilage in the hydrated condition, and the hard component (the collagen fibre bundles) in the dehydrated condition.

In both relaxed and unrelaxed conditions, the modulus is independent of frequency, and both bulk and parallel to surface modes give the same value for M'. This implies that, in these conditions, $\omega_{0B}/q_B = \omega_{0S}/q_S$ from which the refractive index can be

obtained, $n = (\omega_{0B}/\omega_{0S})\sin(\theta/2)$. The values of n measured by refractometry at low concentrations (black dots) are reported in Figure 4.11 together with the values obtained by the ratio of the frequencies of bulk and parallel to surface modes (red dots). Although the Brillouin-derived refractive index of the hydrogel behaved

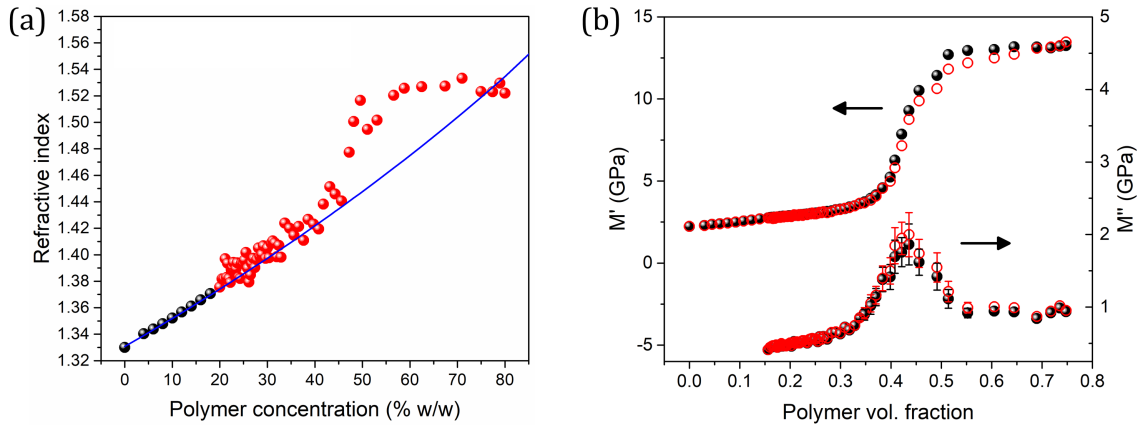

Figure 4.11.: *Plot of refractive index measured by refractometry at low concentration (black dots) and obtained from Brillouin measurements (red dots). The blue line is a linear extrapolation of* $1/n^2$ *in the range 0–19% polymer concentration,* $n = 1/\sqrt{0.56467 - 0.00175x}$. *(b) Storage and loss moduli calculated from the Brillouin frequency shift and linewidth presented in Figure 4.10c. Black dots are data determined using extrapolated refractive indices (blue line in (a)), and red circles are data derived from refractive indices determined from Brillouin measurements (red dots in (a)).*

non-uniformly during the glass transition (Figure 4.11a), the storage and loss moduli are relatively unaffected by this behaviour. Moduli determined using a linear extrapolation of $1/n^2$ (black dots in Figure 4.11b) and those derived from Brillouin measurements (red circles in Figure 4.11b) display the same characteristic behaviour observed in Figure 4.10c.

The glass transition in dried collagen was first investigated through a more traditional thermodynamic path by Flory and Garret [179] and attributed to the temperature-induced arrest of the side chains of collagen molecules. As in the analyses of the hardening of epoxy resins [180, 181], the mode-coupling theory (MCT) [182] provides a rationale for the early stage of the structural arrest associated with the glass transition of collagen (Appendix A). The time scale investigated by BLS is the most appropriate to unveil the divergence of the structural relaxation that is the intimate nature of the glass transition. Fundamental physical studies on the glass transition phenomenon have shown that the relaxation of density fluctuations in the gigahertz region is dominated by the coupling between density fluctuation modes, originating from the glass transition itself [182].

4.4. Rule of Mixtures

The Voigt and Reuss models provide an upper and lower bound, respectively, for the elastic modulus of a composite material. Based on this rule of mixing, the Brillouin-derived storage modulus of the gelatin hydrogels can be modelled as a weighted average of solvent and solute moduli or, of their reciprocal values. A fit to the Voigt

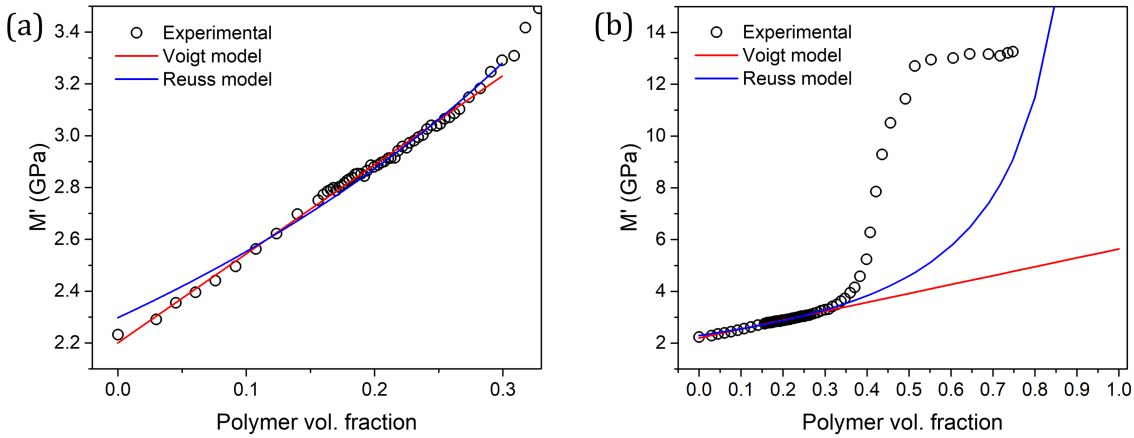

Figure 4.12.: *Evolution in storage modulus versus polymer volume fraction (1−ϵ). (a) Red line: linear fit to a Voigt model (3.6) which predicts the storage moduli of water and solute to be $M_f = 2.20 \pm 0.01$ GPa and $M_s = 5.64 \pm 0.03$ GPa, respectively; $R^2 = 0.994$. Blue line: fit to a Reuss model (3.7), giving the storage modulus of water as $M_f = 2.298 \pm 0.005$ GPa and failing to accurately determine the modulus of the solute (predicted value $M_f = (1 \pm 8) \times 10^{43}$ GPa); $R^2 = 0.985$. (b) The evolution of the Voigt (red) and Reuss (blue) models across the entire concentration range, using the parameters derived in (a). Fits were applied for ϵ =0.7–1 and errors denote the standard error in the fit.*

model (Figure 4.12a) for a water volume fraction of 0.7–1.0 yields a storage modulus of 2.20 GPa and 5.64 GPa for the fluid (water) and solute components, respectively. The value predicted for the fluid component agrees well with the measured storage modulus of water (2.2 GPa), and the predicted modulus of the solute is plausible for a highly hydrated network of gelatin molecules. A fit to the Reuss model (Figure 4.12a) resulted in a reasonable value for the storage modulus of the fluid component (2.3 GPa), however it failed to accurately determine a value for the solute (predicted value $M_s = (1 \pm 8) \times 10^{43}$ GPa). Figure 4.12b shows the fit to both Voigt and Reuss models plotted with the parameters for M_f and M_s derived from the respective fits in part (a). Both models fit the hydrated regime well, however as $\epsilon \to 0$ the Reuss model diverges, resulting in an unrealistically large value of M_s. Therefore, for the broad hydration range investigated here, the Voigt model was found to fit the data better than the inverse relation (Reuss) used in previous works [91].

The storage modulus is derived from the measured acoustic wave velocity c and the density of the sample, from the relation:

$$c = \sqrt{M'/\rho}. \tag{4.3}$$

In the highly hydrated regime ($\epsilon = 0.7$–1.0), the effect of the square root operation approximates to a decrease in gradient with respect to that of M as a function of ϵ. This function behaviour is demonstrated by the simulated data for $y(x)$ in the range $x = 0$–1 in Figure 4.13. The calculated density of the hydrogels is linearly dependent

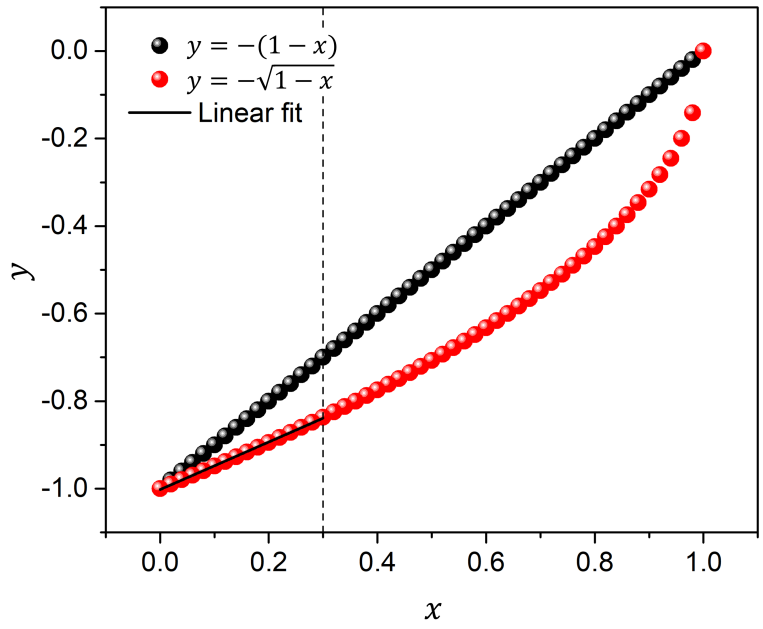

Figure 4.13.: *Plot of $y = -(1-x)$ (black) and $y = -\sqrt{1-x}$ (red) for $x = 0$–1, where $(1-x) = \epsilon$. For $x = 0-0.3$, $y = -\sqrt{1-x}$ is approximately linear ($R^2 = 0.999$), with a gradient of -0.54. Dashed line at $x = 0.3$.*

on the water volume fraction ($\rho = 1.35 - 0.35\epsilon$), so the overall effect of equation (4.3) on the highly hydrated regime can be approximated as a decrease in gradient, therefore not significantly changing the shape of the function. Applying this logic allows the Voigt and Reuss models to be used to describe the acoustic wave velocity, with the Voigt model:

$$c = \epsilon c_f + (1-\epsilon)c_s \tag{4.4}$$

providing the upper bound, and the Reuss model:

$$\frac{1}{c} = \frac{\epsilon}{c_f} + \frac{(1-\epsilon)}{c_s} \tag{4.5}$$

the lower bound. c_f and c_s are the acoustic wave velocities of the fluid and solute components, respectively, analogous to the classical interpretation used in equations (3.6) and (3.7) in Chapter 3.

Applying the rule of mixtures to the acoustic wave velocity (Figure 4.14) results in reasonable predictions for the acoustic velocity of the fluid and solute parts of the gel. Fitting the hydrogel data with the Voigt model (Figure 4.14a) gave values of

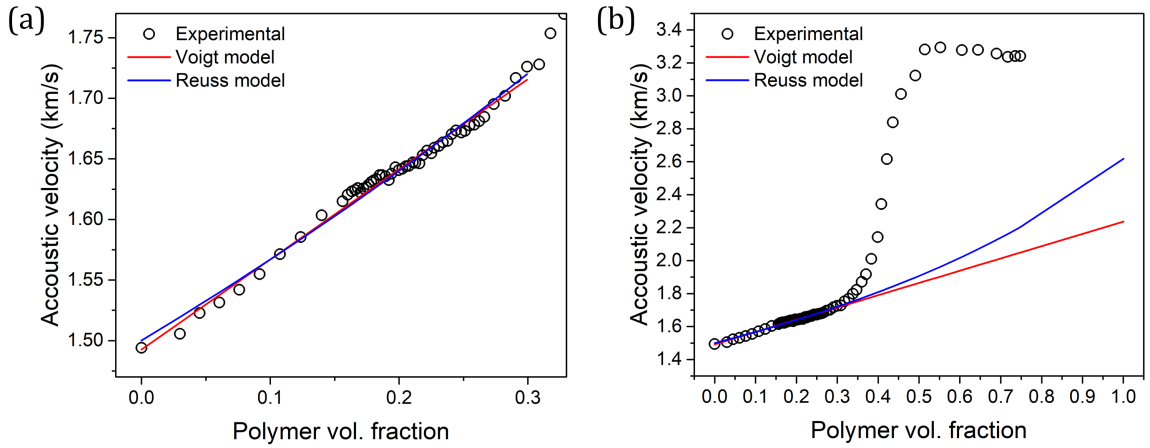

Figure 4.14.: *Evolution of acoustic wave velocity as a function of polymer volume fraction (1-ϵ). (a) Red line: fit to a Voigt (4.4) model, giving values of $c_f = 1.493 \pm 0.002$ and $c_s = 2.24 \pm 0.01$ km/s for the fluid and solute components, respectively; $R^2 = 0.988$. Blue line: fit to a Reuss model (4.5), giving $c_f = 1.500 \pm 0.002$ and $c_s = 2.62 \pm 0.03$ km/s; $R^2 = 0.984$. (b) Comparison of Voigt and Reuss models over entire concentration range using parameters for fluid and solute moduli derived in (a). Fits were applied for $\epsilon = 0.7$–1 and errors denote the standard error in the fit.*

1.493 km/s and 2.24 km/s for the fluid and solute components, respectively, whereas a fit to the Reuss model gave $c_f = 1.500$ km/s and $c_s = 2.62$ km/s. Both predictions for the fluid component match closely the measured acoustic wave velocity of water (1.49 km/s). The value for the solute component given by the Voigt model resulted in a similar modulus to that found in Figure 4.12, albeit slightly higher at 6.76 GPa. The fit of the Reuss model to the acoustic wave velocity was able to give a reasonable value for the storage modulus of the solute, compared to that determined in Figure 4.12. The modulus of 9.13 GPa was higher than that determined by the Voigt model, however, since neither model fits the data through the glass-like transition observed in the hydrogels of lower hydration, neither value is close to what is measured experimentally for the dehydrated gels. This result indicates that the rule of mixing is valid when applied to the acoustic wave velocity, provided that the system remains in the same phase. In the case of the gelatin hydrogels studied here, both models appear to be valid in the liquid-like phase (0–0.3 polymer volume fraction), but break down

at the glass transition. An effective medium model does not take into account the structural arrest the system undergoes, and methods such as mode-coupling theory are more appropriate to model the glass transition itself.

4.5. Summary

This chapter has included measurements of gelatin hydrogels across a range of frequencies, including Young's modulus measurements in the Hz (compressive testing) and MHz (ultrasound elastography) regimes, and longitudinal modulus measurements in the GHz regime (Brillouin spectroscopy). Raman spectroscopy was used alongside Brillouin microscopy to determine the effect of chemical cross-linking on the hydrogels, highlighting the potential of correlative Brillouin-Raman measurements. The stability of the gels used throughout this thesis was confirmed, and the onset of gelation was monitored with Brillouin microscopy. Dehydrating the hydrogels revealed a glass-like transition, associated with a sigmoidal distribution of the Brillouin frequency shift, and a corresponding maximum in Brillouin linewidth. This will be explored further using Raman spectroscopy in the following chapter.

5. Raman spectroscopy as a correlative technique to Brillouin light scattering

The following chapter contains sections from the publication "Predicting the refractive index of tissue models using light scattering spectroscopy" [2].

5.1. Introduction

Raman spectroscopy provides valuable information on the chemical composition and structure of materials through the inelastic scattering of light from molecular vibrations. Brillouin and Raman spectroscopy are "sister" techniques, with light scattering occurring on adjacent frequency scales, providing information on mechanical and chemical composition, respectively. The first high-contrast Brillouin-Raman microscope, enabling simultaneous measurement of micro-mechanical and chemical properties, was realised by Scarponi et al. [101] in 2017. In both Raman spectroscopy, and BLS, the signal intensity is linearly proportional to the concentration or density of the scattering species [67, 183], which in turn is related to the refractive index of the investigated materials.

This chapter presents Raman microspectroscopy measurements applied to gelatin hydrogels, used as biological tissue models. The first section aims to use Raman spectroscopy to monitor the refractive index of the hydrogels, using a calibration model based on Raman band intensities and measurements conducted with an Abbe refractometer. Simultaneous Brillouin and Raman measurements demonstrate how this method can be applied to obtain Brillouin spectra and refractive indices from the same spatial location within the sample, facilitating the determination of the storage and loss moduli from the Brillouin spectra. The latter section aims to utilise Raman spectroscopy as a complementary technique to BLS, and measures the Raman spectra of a thin film of gelatin during dehydration, to be compared with the results obtained using BLS in Chapter 4.

5.2. Refractive index prediction

Gelatin hydrogels were used as biological tissue models to investigate the capabilities of Raman microscopy in monitoring changes in refractive index. Figure 5.1 shows the normalised Raman spectra of gels between 4 and 18% gelatin, in both the fingerprint (Figure 5.1a) and C-H stretching regions (Figure 5.1b, RHS). Brillouin spectra were also acquired simultaneously to the high wavenumber spectra (Figure 5.1b LHS). There is a clear dependence of the scattering intensity on gel concentration across

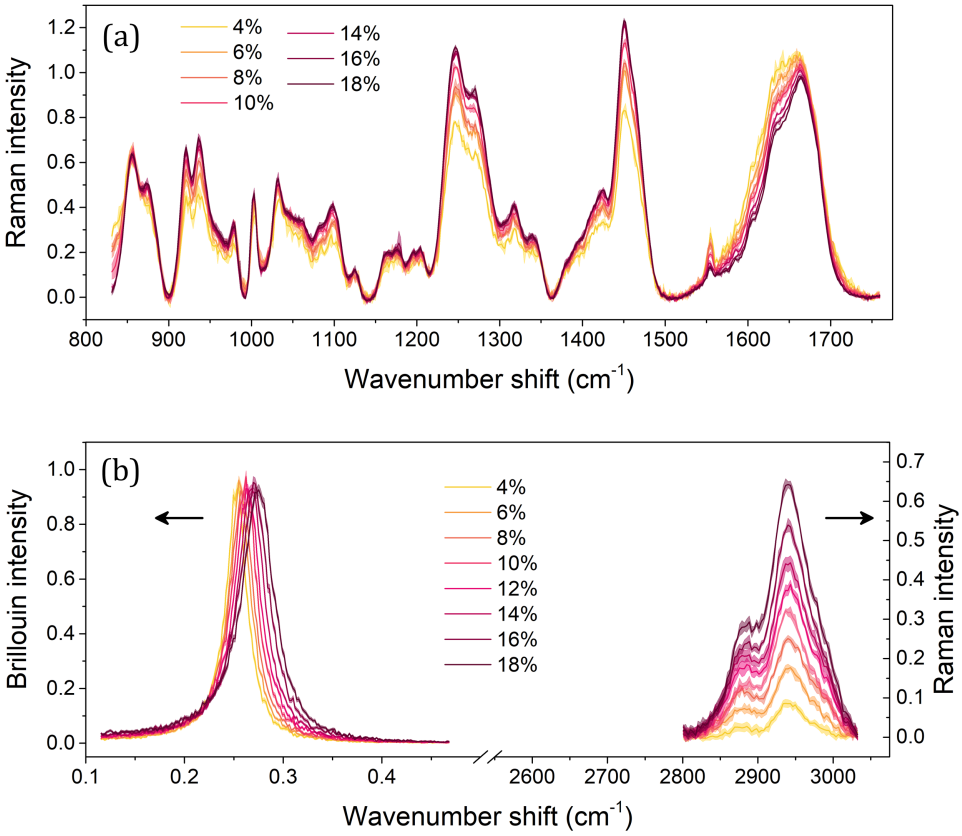

Figure 5.1.: *Normalised Raman and Brillouin spectra of gelatin hydrogels measured across (a) the fingerprint and (b) Brillouin (left) and C-H stretching region (right). Each Raman spectrum is an average from (a) three or (b) five measurements, pre-processed and analysed as described in Chapter 3. Each Brillouin spectrum is an average of three measurements, normalised to the Stokes peak. Shading is the standard deviation of the measurements.*

the entire spectrum. For example, there is a distinct increase in the intensity of the C-H stretching peaks with increasing concentration (Figure 5.1b, RHS). The Brillouin spectra have been discussed in Chapter 4.

Principal component analysis (PCA) was applied to the spectra in the fingerprint region to determine the regions of the spectra where the variance across the concen-

tration range was most significant. The first principal component (PC1) accounts for the highest percentage of the total variance, principal component 2 (PC2), the second highest and so on. Here, PC1 accounted for 89% of the total variance, and the loadings (Figure 5.2a) highlight the spectral regions where this variance is observed. The corresponding score plot (Figure 5.2b) represents the trend in the variation as a

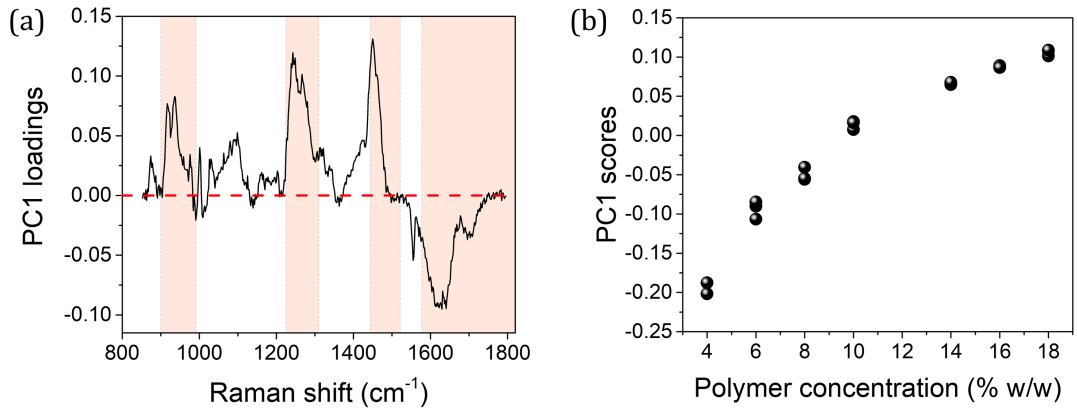

Figure 5.2.: *PCA applied to the fingerprint region of the spectra. (a) Principal component 1 (PC1) loading, where shading denotes spectral regions of interest and the red dashed line at $y = 0$ serves as a guide for the eye. (b) Corresponding score plot for PC1, showing tight clustering between repeated measurements.*

function of concentration.

Through PCA, four spectral regions of interest were identified and the integrated intensities were plotted as a function of polymer concentration (Figure 5.3). Among these is the 898–988 cm^{-1} region, which contains a doublet comprising of peaks at 922 cm^{-1} and 938 cm^{-1}, attributed to C-C stretching of the proline ring and plausibly C-C stretching of the protein backbone [184, 185], respectively. There is also a small peak at 980 cm^{-1}, likely due to arginine [186]. The signals in this spectral region are sensitive to the presence of "bound" water within the hydrogel [187]. The number of protein binding sites increases with increasing polymer concentration, and so it follows that the quantity of bound water is also observed to increase with increasing gel concentration (Figure 5.3a). This behaviour replicates well what has previously been observed in this spectral range for type I collagen and porcine skin samples [187], and supports the linearised model used in the Brillouin study of gelatin hydrogels (Chapter 4), where the kinematic viscosity (determined from the Brillouin linewidth) is described as a concentration-dependent weighted average of the bulk and hydration water components, and used to determined the retardation factor of hydration water. The range 1216–1300 cm^{-1} presents a doublet at 1248 and 1271 cm^{-1} (amide III [184]), while the range 1431–1507 cm^{-1} corresponds to CH_3 and

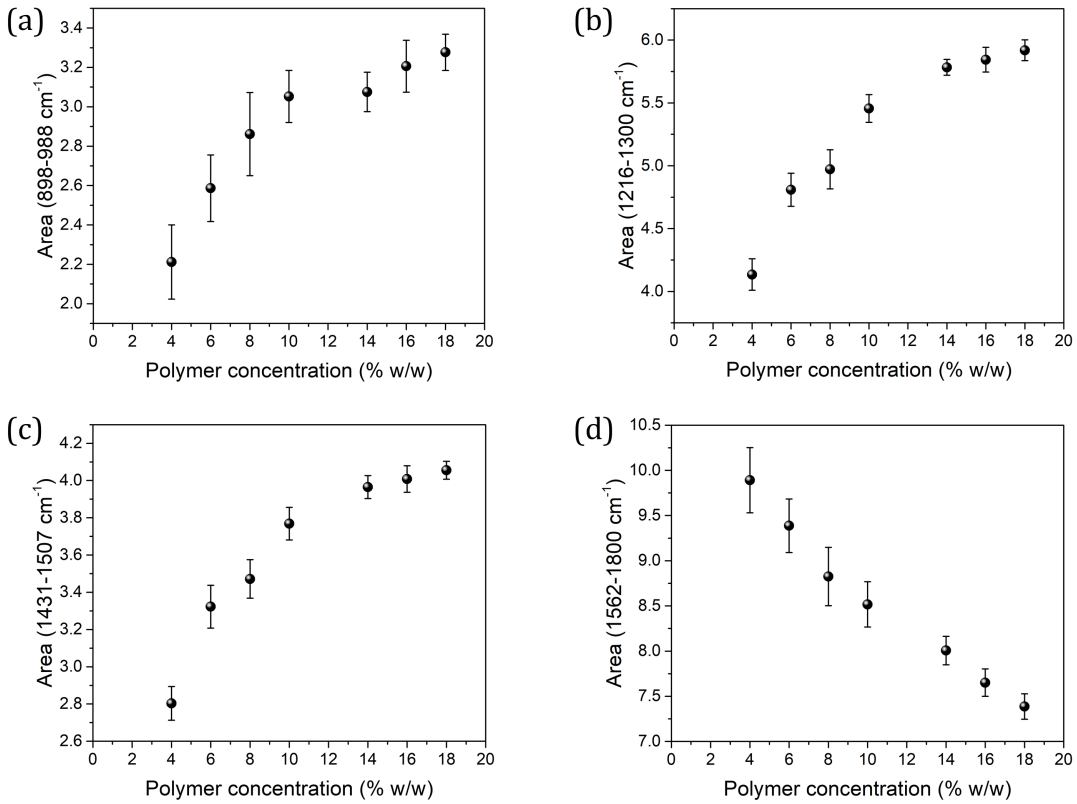

Figure 5.3.: *Integrated spectral regions as a function of polymer concentration for wavenumber ranges: (a) 898–988 cm^{-1} ("bound" water), (b) 1216–1300 cm^{-1} (amide III), (c) 1431–1507 cm^{-1} (CH_3 and CH_2 deformations), (d) 1562–1800 cm^{-1} (amide I and water bending mode).*

CH_2 deformations [184, 188]. The integrals of both bands increase with increasing polymer concentration (Figure 5.3b–c), before appearing to reach a plateau towards higher concentrations. The range between 1562 and 1800 cm^{-1} contains contributions from both protein and water. The peak centred at 1665 cm^{-1} is due to amide I [184, 188], and is assigned to disordered protein structure [189, 190], whilst the shoulder at 1635 cm^{-1} is associated with denatured triple helices [190] with a contribution from water (bending mode at 1635 cm^{-1}) [191, 192]. Highly hydrated gelatin is expected to be more disordered than gels of lower water content, where a larger proportion of alpha helices are expected to be present [190], so it follows that the integral of the 1562–1800 cm^{-1} region decreases as water content is reduced and the degree of disorder decreases (Figure 5.3d). Of the four spectral bands identified within the fingerprint region, the 1562–1800 cm^{-1} region has a linear dependence on polymer concentration, in line with the linear behaviour previously observed for the refractive index (Chapter 4). In addition to the fingerprint region, the C-H stretching band

[193] presents two peaks at 2885 and 2940 cm^{-1}, corresponding to symmetric and anti-symmetric CH_2 stretches, respectively. This band also displays a linear dependence on gel concentration, and so was used alongside the amide I band to construct a model, where the integrated intensities of each spectral region were plotted versus the refractive index of the corresponding gel concentration (Figure 5.4).

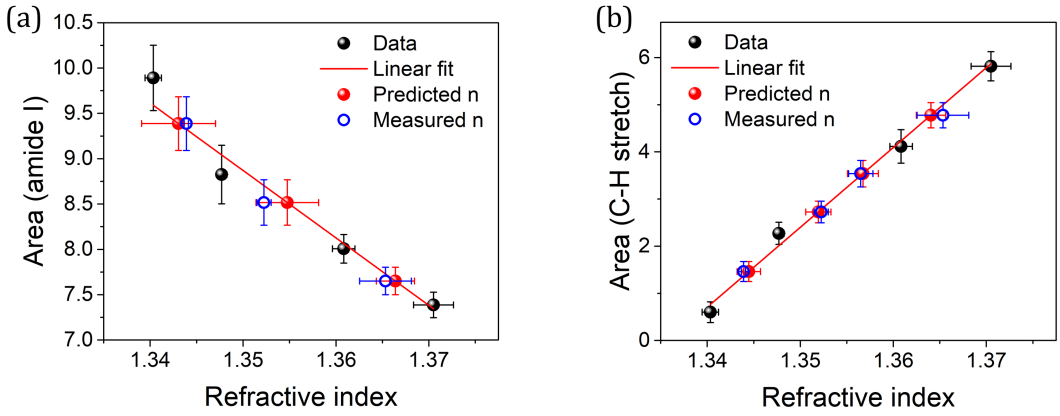

Figure 5.4.: *Plot of (a) amide I (1562–1800 cm^{-1}) and (b) C-H stretching (2800–3040 cm^{-1}) integrated intensity versus refractive index of gelatin hydrogels measured with Abbe refractometry. Red line denotes a linear fit of the data-set used as model data for each wavenumber region (black filled circles): (a) $R^2 = 0.96$, (b) $R^2 = 0.99$. Red filled circles denote the refractive indices predicted by the Raman spectra and blue circles indicate those measured using Abbe refractometry for gels of the same concentration. Error bars denote the standard deviation across repeat measurements.*

In the model, the data are split into two subsets: half of the samples were used as model data to derive the fit and the other half were used as test samples to determine the refractive index. The data points selected as model data corresponded to 4%, 8%, 14%, and 18% gels (black filled circles in Figure 5.4). A linear fit was applied to these data (red line) and calibration functions were derived for the amide I (5.1) and C-H stretching regions (5.2):

$$y = (109.3137 \pm 12) - (74.402 \pm 9)n \tag{5.1}$$

$$y = (169.351 \pm 12)n - (226.226 \pm 16), \tag{5.2}$$

where y represents the integrated intensity of the peak and n the corresponding refractive index of the gel. The refractive indices of the test samples, derived from the integrated intensity (red filled circles) using the calibration equations, were then compared with those obtained with an Abbe refractometer (blue empty circles). Figure 5.4 shows that there is a close correspondence between predicted and measured

values of n, confirmed by plotting the predicted versus the measured refractive indices (Figure 5.5).

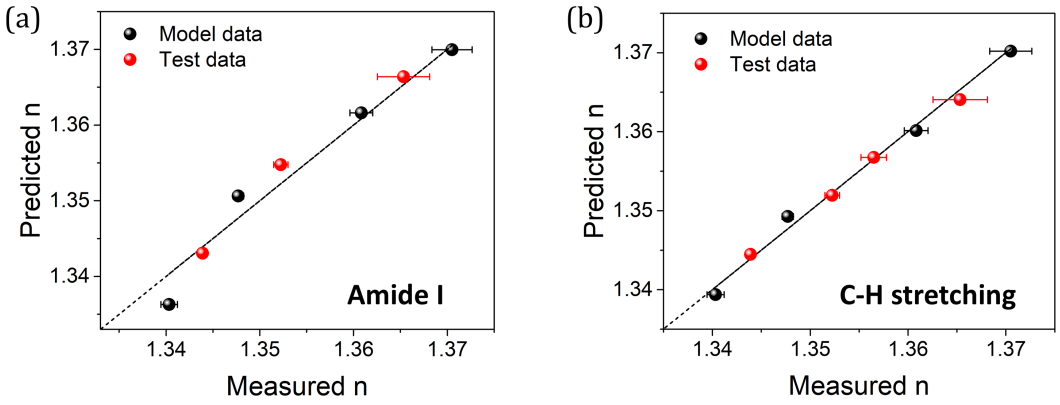

Figure 5.5.: *Predicted vs. measured refractive indices for (a) amide I and (b) C-H stretching. Black dots are the data from which the model was calculated and red dots correspond to test data, where the refractive index was determined from the model. Dashed line ($y = x$) serves as a guide for the eye. Error bars denote the standard deviation.*

The RMSE (root mean square error) of these data was 0.002 and 0.0009 for the amide-I and C-H stretching modes, respectively. This indicates that the model is capable of predicting the refractive index of the gelatin hydrogels with high accuracy. Table 5.1 lists the complete results for this analysis.

A very good estimation of the refractive index was found using this method, with predicted values of n being within 0.02–0.3% of the measured values. Differences between measured and predicted values were of the same order of magnitude as the standard deviation of the measurements performed with an Abbe refractometer (Table 5.1). Prediction based on C-H stretching analysis was generally more accurate than that based on amide I, as can be expected because the C-H stretching modes are exclusively protein modes, whereas the amide I band contains a contribution from the water bending mode (the amide I increases with concentration, while the water bending decreases).

5.3. Gelatin dehydration

The dehydration of a thin film of gelatin was measured using Raman spectroscopy, to correspond to the measurements conducted with Brillouin microscopy in Chapter 4. Measurements were taken every 2–4 min at the interface of the hydrogel film and

Table 5.1.: *Refractive indices derived from Abbe refractometry and Raman measurements using the calibration model.*[a]

Polymer concentration (%)	**Measured n (±SD)**[b]	**Predicted n (± difference)**[c]	
		Amide I	ν(C-H)
4	1.3403 (±0.0009)	1.3363 (±0.004)	1.3394 (±0.0009)
6	1.3403 (±0.0002)	1.3431 (±0.0008)	1.3445 (±0.0006)
8	1.3477 (±0.0006)	1.3506 (±0.003)	1.3493 (±0.0016)
10	1.3523 (±0.0008)	1.3548 (±0.003)	1.3519 (±0.0003)
12	1.356 (±0.001)	-	1.3567 (±0.0002)
14	1.361 (±0.001)	1.3616 (±0.0008)	1.3602 (±0.0007)
16	1.365 (±0.003)	1.3664 (±0.0011)	1.3641 (±0.0013)
18	1.370 (±0.002)	1.3699 (±0.0006)	1.3702 (±0.0003)

Data used for calibration Data used to test model

[a]Note that this method is based on a calibration to Abbe refractometry data measured with a D line (589 nm) light source, so all refractive indices presented refer to 589 nm, irrespective of the wavelength at which Raman spectra were acquired.
[b]Standard deviation derived from five measurements at each concentration.
[c]Difference between refractive indices measured by Abbe refractometry and those determined from Raman spectroscopy.

the CaF_2 substrate. At time $t = 0$ all films have a concentration of 20% gelatin, so should also be relatively comparable to the 18% gelatin samples measured in Section 5.2. Normalised Raman spectra from the first 40–60 min of thin film dehydration (Figure 5.6a,b) show similar trends to those observed for hydrated gels in Section 5.2, whereas the normalised spectra for the thick film (Figure 5.6c) show more subtle changes. The spectra for the thinner samples have a higher level of noise than those measured for the thick film. This is likely due to the higher rate of dehydration in the thin samples, resulting in more changes within the gel over the spectral acquisition time than in the thick film. PCA revealed that the main source of variation across the spectra occurred in the same spectral regions as those identified in Section 5.2. Integrating the spectra across these regions reveals how the bands change during dehydration (Figure 5.7). As observed for gels between 4 and 18% polymer (Figure 5.3a),

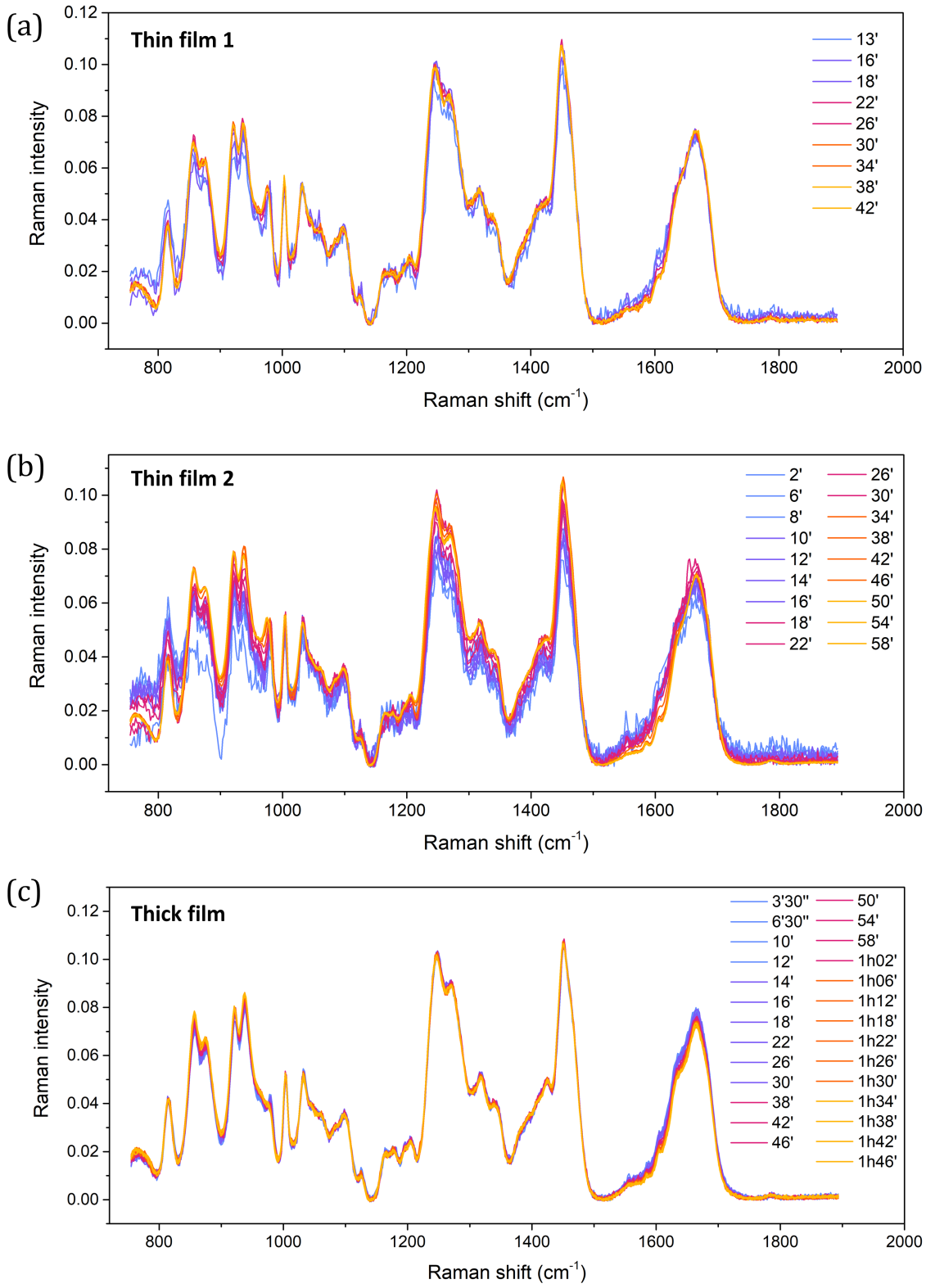

Figure 5.6.: *Normalised Raman spectra and the evolution over time for (a,b) two thin films of gelatin (200–300 µm thick) and (c) a thick film of gelatin (∼2 mm thick).*

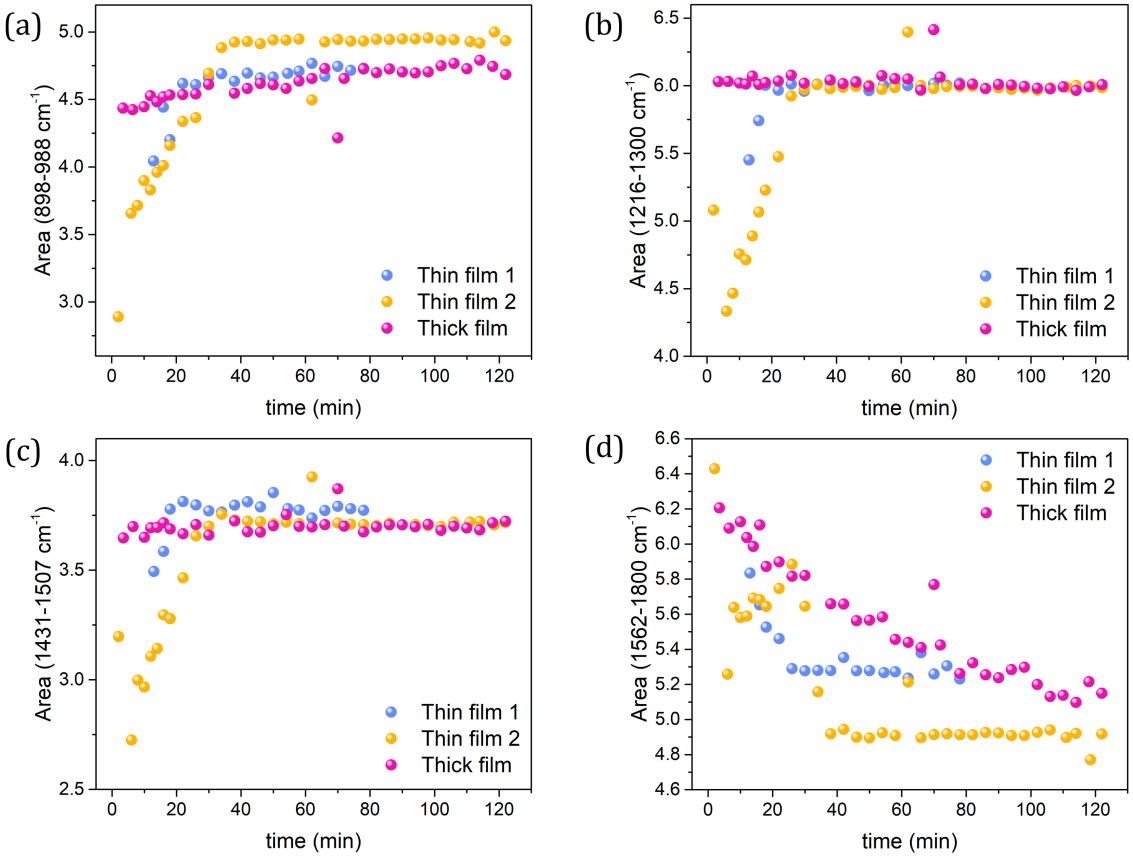

Figure 5.7.: *Integrated spectral regions as a function of time after film deposition for wavenumber ranges: (a) 898–988 cm^{-1} ("bound" water), (b) 1216–1300 cm^{-1} (amide III), (c) 1431–1507 cm^{-1} (CH_3 and CH_2 deformations), (d) 1562–1800 cm^{-1} (protein and water). Note that the glass transition observed with Brillouin measurements occurred after ∼70–80 min.*

the content of bound water within the hydrogel (associated with the 898–988 cm^{-1} band [187]) increases with time as the gel dehydrates (Figure 5.7a). A faster rate of increase is seen for the two thin films than the thick film, due to the slower rate of water loss in the thicker sample. The amide III region (1216–1300 cm^{-1}; Figure 5.7b) and CH_3 and CH_2 deformation band (1431–1507 cm^{-1}; Figure 5.7c) are also found to increase in the early stages of dehydration for the two thin film samples; however, no significant change is observed for the thick film. The integrals of the amide III band and CH_3 and CH_2 deformation bands for the thick film (Figure 5.7b,c) match closely with those obtained for an 18% gelatin in Section 5.2 (Figure 5.3b,c). The integrals of these bands for thin films of gelatin (Figure 5.7b,c) are much lower for early times ($t < 20$ min), and increase until they reach a plateau, matching the thick film data. Comparing the integrals to those obtained for an 18% gelatin, suggests

that the changes observed in the thin films could just be artefacts from normalisation of slightly noisy spectra.

The protein and water integral (1562–1800 cm^{-1}; Figure 5.7d) decreases for all gelatin films. The two thin films plateau after $\sim$ 40 min, in line with the behaviour of the bound water in Figure 5.7a, suggesting that this is when the gel has reached its dehydration limit. The slower rate of dehydration of the thicker film, results in a more gradual decline in water content than that observed for the thin films. This spectral region also contains information about the secondary structure of proteins (Amide I peak). The lack of significant change in the bandshape of the Amide I peak throughout the dehydration process may suggest that there are no major conformational changes in the protein during the glass transition (Chapter 4).

The dehydration of the hydrogels was measured over the first 80–120 min after gel deposition. Within this time frame, Brillouin measurements revealed a glass-like transition (Chapter 4), shown by the sigmoidal behaviour of the Brillouin frequency shift and corresponding maximum in linewidth. However, although Raman measurements reveal changes in the relative water and protein content within the hydrogels, there is no indication of the glass-like transition revealed by Brillouin microscopy. This is indicative of the differences between the two techniques, with Raman scattering resulting from interactions on an intra-molecular length scale, and Brillouin scattering from acoustic phonons giving a relatively larger overview of interactions within the system.

5.4. Summary

This chapter has presented Raman spectroscopy as a correlative, and complementary technique to Brillouin spectroscopy. Raman measurements of gelatin hydrogels have been shown to correlate to refractive index measurements, and a calibration model enabled the refractive indices of the hydrogels to be predicted from the Raman spectra. Unlike Brillouin spectroscopy, Raman measurements failed to detect the glass transition observed in Chapter 4, highlighting the differences between the measurement capabilities of the two techniques.

6. Development and use of a VIPA-based Brillouin spectrometer

The following chapter contains sections from the publication "Brillouin microspectroscopy data of tissue-mimicking gelatin hydrogels" [138].

6.1. Introduction

The virtually imaged phase array (VIPA) etalon has enabled faster Brillouin measurements of biological samples, avoiding the need for the scanning mirrors required by the TFPI. Instead, multiple reflections within the slightly tilted etalon (Figure 6.1a) result in an array of transmitted beams with varying phase delay, and interference among these angularly disperse the frequency components.

Since the development of the first VIPA-based Brillouin spectrometer [29], numerous developments and improvements to spectrometer design have been proposed. The original spectrometer contained a single VIPA etalon; however, since then, the use of multiple etalons has been explored [103], separating the dispersion axis from the "crosstalk" (Figure 6.1b) between Rayleigh peaks of adjacent orders.

This chapter is based around a spectrometer consisting of two VIPA etalons and seeks to discuss its development and use. Improvements to the basic system design are explored, such as the introduction of a Lyot stop, and the choice of detector. In addition to this, data on hydrogels are presented, enabling some comparison with the measurements conducted previously using a TFPI-based spectrometer (Chapter 4), and various spectral analysis methods are explored using data from the interface of water and oil drops.

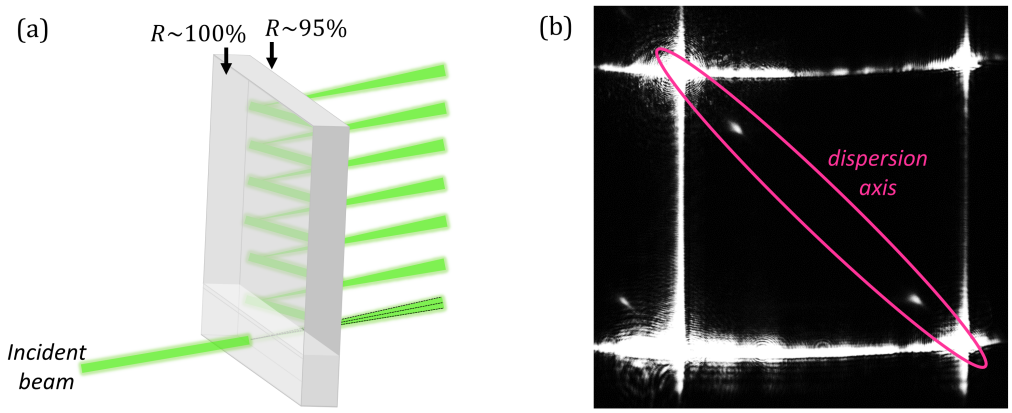

Figure 6.1.: *(a) Schematic of a VIPA etalon. Incoming light enters the tilted etalon through an entrance window and undergoes multiple internal reflections, due to the high reflectivity R of the two sides of the etalon. The edge on the opposite side to the entrance window has a reflectivity of* $\sim 95\%$*, meaning that some light is transmitted on each reflection, resulting in an array of output beams with increasing phase delay. The angle of propagation of the output beams is wavelength dependent (light of different wavelengths highlighted by black dashed lines in first output beam). Interference among the array of output beams therefore results in angular dispersion of the frequency components [29, 45]. (b) sCMOS image of methanol (1 s exposure) from a dual-stage VIPA spectrometer. The edges of the square are "crosstalk" between Rayleigh peaks from adjacent orders. With two orthogonal VIPA etalons, the dispersion axis is spatially separated from the crosstalk.*

6.2. VIPA spectrometer

A lab-built dual-stage VIPA spectrometer was developed. The spectrometer was coupled to a two-deck inverted microscope (Olympus iX73 with epi-configuration) and incident laser light of 532 nm wavelength was used. The full optical design is shown in Figure 6.2.

Two single-frequency 532 nm light sources were used inter-changeably; a DPSS laser (Cobolt Samba) with 300 mW output power and < 1 MHz spectral linewidth, and a Torus 532 (Laser Quantum) with 250–750 mW output power and 1 MHz spectral linewidth. The Cobolt laser was included in the original system design [194], and a periscope was used to introduce the Torus 532 laser to the existing beam path whilst maintaining the alignment of the original laser. The laser beam passed through an optical isolator (Thorlabs) and a motorised neutral density filter wheel (Thorlabs) was used to control the power transmitted to the sample. A half waveplate $\lambda/2$ (Thorlabs) was used to match the polarisation of the incident light to that reflected by the polarising beam splitter (PBS). The beam was then expanded to a diameter

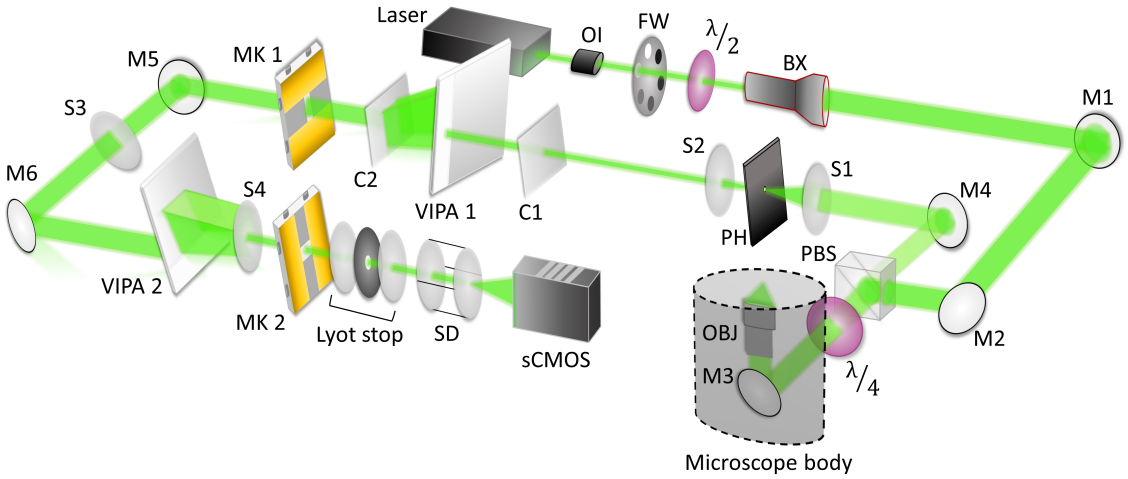

Figure 6.2.: *Dual-stage VIPA micro-spectroscopy setup, consisting of; 532 nm laser; OI: optical isolator; FW: neutral density filter wheel; λ/2: half-wave plate; BX: beam expander; M1-6: mirrors; PBS: polarising beam splitter; λ/2: half-wave plate; OBJ: microscope objective; PH: pinhole; C1-2: cylindrical lenses; S1-4: spherical lenses; MK1-2: spatial masks; SD: spherical lens doublet.*

of ∼ 8.5 mm to ensure the entrance to the objective (diameter 8 mm) was filled. A 10× beam expander (Thorlabs) was used when the Cobolt laser was employed, and a 5× beam expander (Thorlabs) was used when the Torus 532 was in use.

The original setup contained a (10:90) non-polarising beam splitter (NPBS) [194] at the entrance of the microscope; however, this was later replaced with a polarising beam-splitter (Thorlabs) to reduce losses in the system. A quarter waveplate $\lambda/4$ (Thorlabs, WPQ10M-532) was placed in between the PBS and the microscope to adjust the polarisation of the light such that the scattered light was transmitted through the PBS. On the first pass through the $\lambda/4$, the linearly polarised light is transformed to circularly polarised light. The scattered light sent back through the $\lambda/4$ is then returned to a linear polarisation, but is rotated by 90° with respect to the incident light. The scattered light is therefore transmitted through the PBS and directed towards the spectrometer.

Within the microscope body, a Chroma sputtered enhanced silver reflective mirror (R ∼ 99.6% at 530 nm) was used to direct the incident light towards the objective. A 60× (NA 1.20) water immersion objective (Olympus UPlanApo) was used for all Brillouin measurements. Back-scattered light from the sample was collected through the same objective and was transmitted through the PBS as previously described. The transmitted light was collected by a spherical lens (Thorlabs) and focused into a 75 µm pinhole (Thorlabs). The light transmitted through the pinhole was collimated

with a spherical lens (Thorlabs, $f = 200$ mm) and focused to the entrance slit of the first VIPA etalon (LightMachinery, 30 GHz FSR) by a cylindrical lens (Thorlabs, $f = 200$ mm). The transmitted light was collected by a second cylindrical lens (Thorlabs, $f = 200$ mm) which focused the dispersed light onto the first spatial mask. The spatial mask (OptoSigma) consisted of adjustable blades in the x and y directions, enabling the desired dispersion order(s) to be selected, and rejecting any unwanted stray light. The transmitted light was focused onto the entrance slit of the second VIPA (orthogonal, but otherwise identical to the first) by a spherical lens (Thorlabs). In the original system [194] the dispersed light was focused onto the second spatial mask by a spherical lens (Thorlabs) and then enlarged by a spherical doublet and detected by an air-cooled sCMOS camera (Andor Zyla 4.2P-USB3), with 13 µm × 13 µm pixel size. However, to reduce the effect of diffraction at the second spatial mask, the spherical doublet was later moved to enlarge the dispersed light prior to focusing it on the second spatial mask, resulting in a larger gap for the beam to pass through.

6.2.1. Lyot stop

A Lyot stop has since been added to the setup to remove the brightest diffraction orders, based on the work by Edrei et al. [112]. The concept is based on Lyot coronagraphy, used in astronomy to block a very bright star and the resulting high order spatial frequencies generated from the diffraction, in order to image a much fainter object of interest (e.g. exoplanets). In Brillouin spectroscopy, a spatial mask is used to block the very intense Rayleigh peaks, and a 4-f imaging system (here, consisting of two spherical lenses; $f = 30$ mm, Thorlabs) is introduced before the camera, where an iris of variable aperture (Thorlabs) is placed in the Fourier plane to block the high order spatial frequencies. Figure 6.3 shows the effect of the Lyot stop on this system, where in Figure 6.3a the iris is fully open and diffraction from Rayleigh peaks is visible as the edges of the square in the image. Part (b) shows the effect of closing the iris, where the highest order spatial frequencies are blocked, resulting in the disappearance of the left-hand edge of the square in the sCMOS image, and an increase in extinction of the Rayleigh peak of ~ 10 dB. In this case, the highest order spatial frequencies correspond to a diffraction line which is well separated from the peaks of interest. However, in more highly scattering samples, the addition of the Lyot stop can be beneficial.

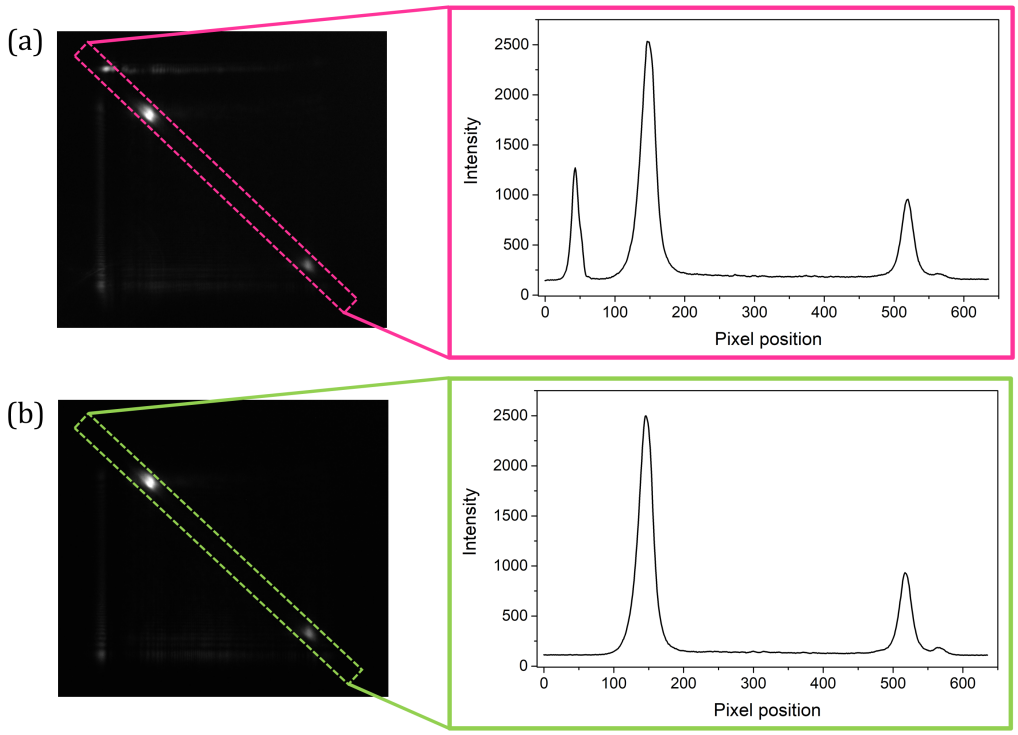

Figure 6.3.: *sCMOS images and associated spectra for methanol (acquisition time 3 s), (a) in the absence and (b) in the presence of a Lyot stop. The diffraction order on the left-hand side of (a) is removed by the Lyot stop, and is therefore not visible in (b).*

6.2.2. System specifications

A summary of the specifications of the VIPA-based system can be found in Table 6.1. Methanol and quartz were used as standards to derive these parameters. The signal to noise ratio (SNR) was calculated as the ratio of peak height to the standard deviation of the intensity in the region between the two Brillouin peaks, and an average was obtained from Stokes and anti-Stokes peaks. The SNR values given in Table 6.1 are an average of at least 5 independent measurements, acquired across several different days.

The spectral resolution and finesse were obtained from measurements of high-purity quartz (Hellma Suprasil) at short exposure times (0.01–1 ms), to avoid saturation of the Rayleigh peaks. The spectral resolution was defined as the full width at half maximum (FWHM) of the Rayleigh peaks (determined by a Gaussian fit), and an average was taken across the two adjacent Rayleigh peaks. The finesse was calculated as the ratio of the FWHM of the Rayleigh peaks to the free spectral range (FSR), and

Table 6.1.: *VIPA-Brillouin microscope specifications with both Cobolt and Torus lasers. Objective lens was 60× (NA 1.2) WI. PBS and NPBS indicate the beam splitter that was in place. Note that the Lyot stop was not in place during this characterisation.*

Parameter	**Value**	
	Cobolt	***Torus***
Laser:		
Power (emission)	300 mW	750 mW*
Power at sample	∼ 6 mW (PBS) ∼ 200 mW (NPBS)	∼ 16 mW* (PBS) ∼ 475 mW* (NPBS)
Spectral linewidth	< 1 MHz	1 MHz
Spectrometer:		
Spectral resolution**	900 ± 100 MHz	490 ± 50 MHz
Finesse	38 ± 6	70 ± 10
SNR	18 ± 2 dB *(methanol, 3 s)*	18 ± 2 dB *(methanol, 3 s)*

**Maximum power (laser power is variable).*

***This is an upper limit on the resolution, and localisation precision of Brillouin peaks is much higher.*

an average of the finesse obtained for the two adjacent Rayleigh peaks was determined. The values for spectral resolution and finesse presented in Table 6.1 are each an average of 3 independent measurements, and the error is the standard deviation.

6.3. Sample measurement

Unless otherwise specified, samples were placed on a round glass coverslip (Biochrom, 170 µm thickness) mounted on an Attofluor cell chamber (Life Technologies) for microscopy measurements. Measurements near the glass interface were not possible, due to specular reflection from the surface, as well as the refractive index mismatch and subsequent high scattering of light at the sample-glass interface, masking the relatively weak Brillouin signals. For measurements of water, a distance of 100 µm away from the glass surface into the water reduced these effects sufficiently (Figure 6.4), further quantified by increasing signal-to-noise ratio (SNR) as the distance from the coverslip was increased (Figure 6.4c). For samples which produced more scattering,

such as gelatin hydrogels, this distance needed to be increased, and so, unless otherwise specified, all Brillouin measurements were conducted at a focal point ~ 150 µm away from the coverslip. For very thin samples (< 150 µm), it was found that coating

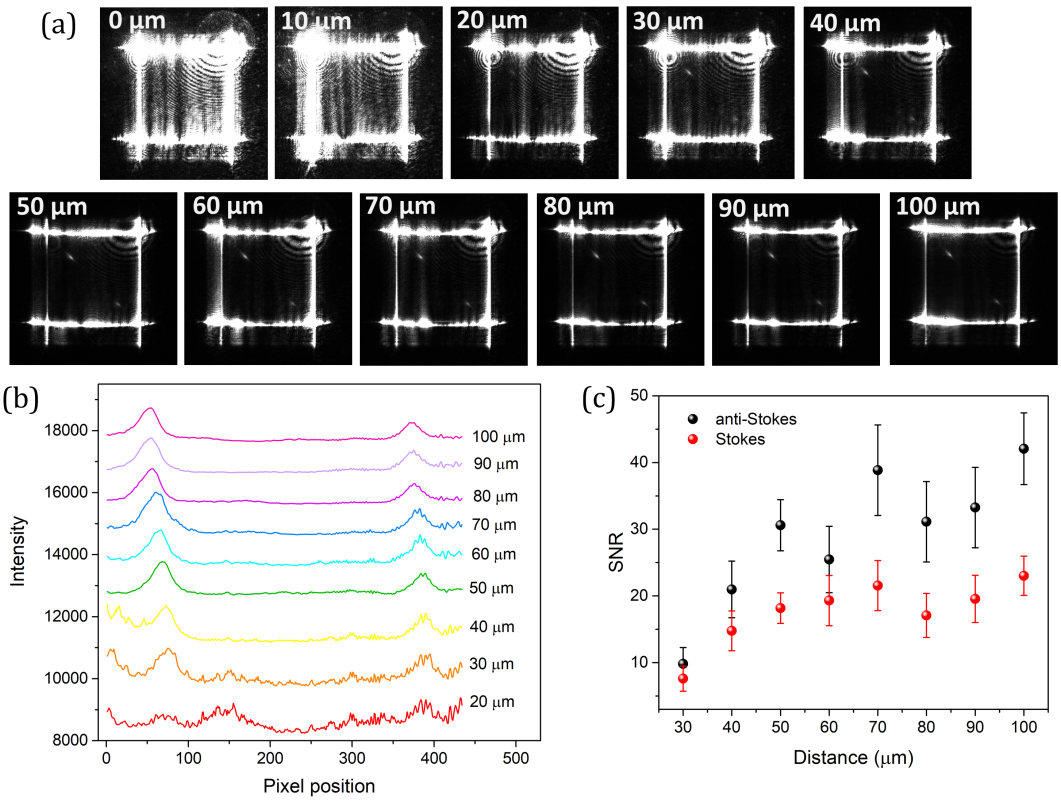

Figure 6.4.: *(a) sCMOS images and (b) associated spectra acquired from the coverslip surface (0 µm) to 100 µm into a distilled water sample. (c) Signal to noise ratio (SNR) as a function of distance from the coverslip surface for Stokes (red) and anti-Stokes (black) peaks. Exposure times were varied according to the intensity, with 0.1 s used for the surface (0 µm), 0.5 s for 10 µm, 1 s for 20 µm, and 3 s for all remaining measurements.*

the coverslip with a thin layer of gelatin hydrogel ($\sim$150 µm) helped to reduce the scattering effects.

6.3.1. Calibration

For all VIPA Brillouin measurements, spectral calibration was performed using known values of frequency shift for methanol and water (5.59 GHz and 7.46 GHz, respectively [104]). Calibration spectra from these standards were collected at the beginning and end of all experiments, and these measurements were averaged for each standard to account for drift during the experiment. To convert the peak position from a pixel to

frequency scale, a scaling factor P was determined according to the relation:

$$P = \frac{2(\nu_w - \nu_m)}{X_m - X_w}, \tag{6.1}$$

where ν_m and ν_w are the known frequency shifts and X_m and X_w the distance in pixels between peaks from neighbouring dispersion orders (Figure 6.5), with subscripts m and w denoting methanol and water, respectively. The free spectral range (FSR)

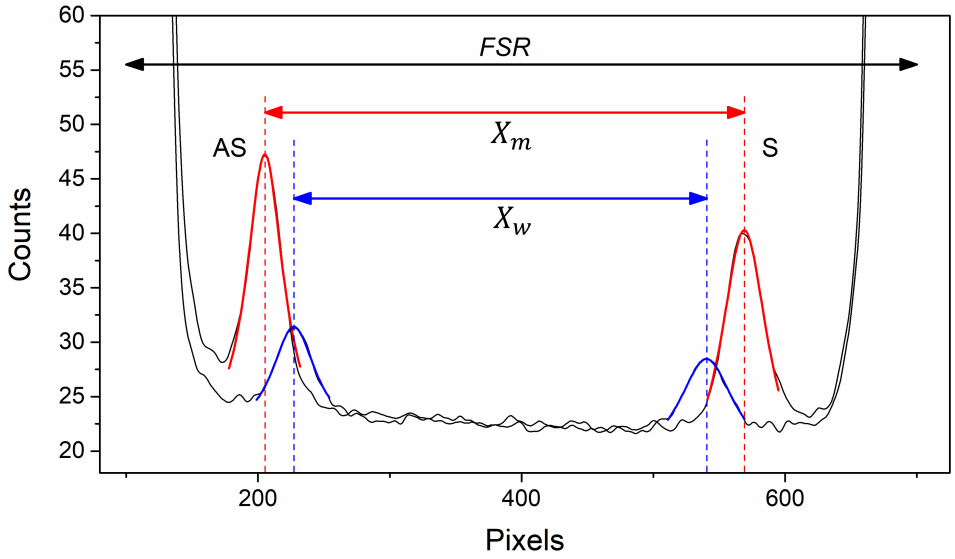

Figure 6.5.: *Calibration spectra and Lorentzian fit for methanol (red) and water (blue). Distances between Brillouin peaks, X_m and X_w, were used to determine absolute peak positions. The free spectral range (FSR) is also shown.*

was taken to be a summation of the measured distance between adjacent Brillouin peaks X and the frequency shift ν of the standards: $FSR = 2\nu + PX$. The Brillouin frequency shift ν_B for each sample was therefore determined from the FSR and the distance X between adjacent Brillouin peaks according to the expression:

$$\nu_B = \frac{1}{2}(FSR - PX). \tag{6.2}$$

6.3.2. Gelatin hydrogels

Gelatin hydrogels were prepared to concentrations of 4%–18% polymer and measured using the Cobolt laser (laser power at sample $\sim$ 6 mW) and dual-VIPA spectrometer. Pseudo-colour images for the varying polymer concentrations are presented in Figure 6.6a. A Brillouin spectrum was extracted from each raw image, and fit analysis to

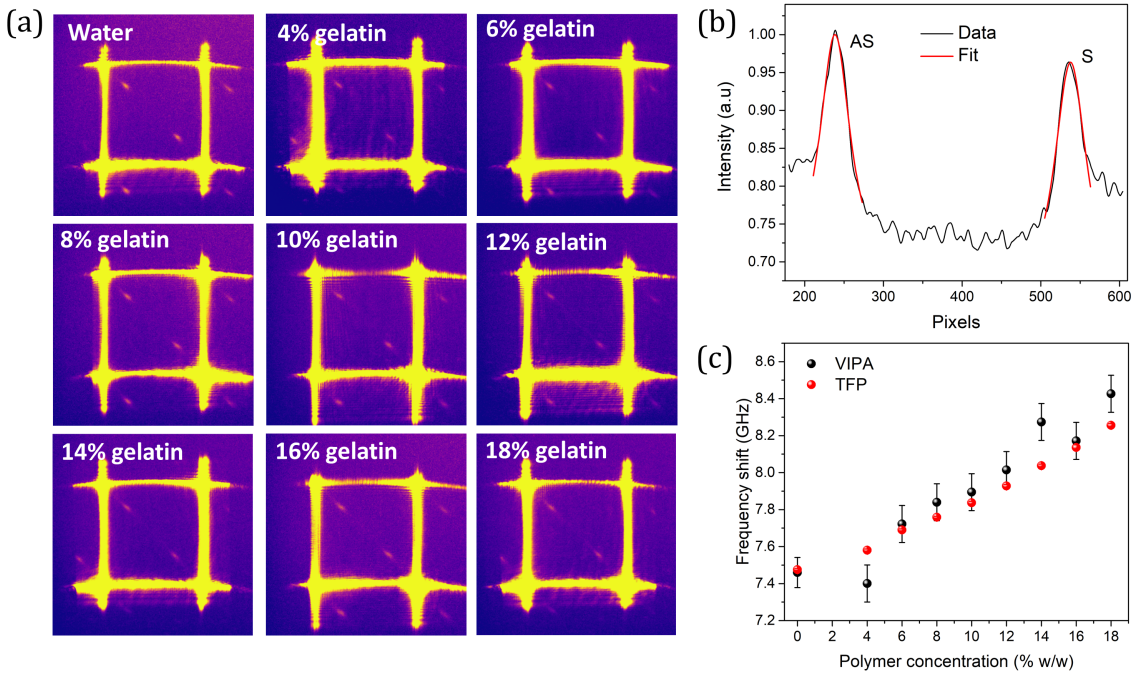

Figure 6.6.: *(a) Pseudo-colour images of the sCMOS outputs for gelatin hydrogels at varying polymer concentration, from 0 to 18% w/w. (b) Spectrum of an 8% gelatin hydrogel before calibration (black line) and Lorentzian fit for both anti-Stokes (AS) and Stokes (S) peaks (red line; $R^2 = 0.97$). (c) Plot of the Brillouin frequency shift vs. polymer concentration of the gelatin hydrogels measured with the VIPA spectrometer (black) and TFP (red). Black error bars account for drift in the calibration spectra during the course of the experiment and encompass intra-sample variability, and red error bars represent the fit error, as in Chapter 4.*

a Lorentzian function was applied to both Stokes and anti-Stokes peaks (Figure 6.6b). Average peak parameters were calculated, and an average Brillouin frequency shift was determined for each concentration (Figure 6.6c). Comparing this data with those measured using the TFPI, presented in Chapter 4, the data from both spectrometers are largely in agreement within the bounds of experimental error. As expected, there is a smaller error associated with the TFPI measurements than the VIPA, owing to the higher spectral resolution and stability of the TFPI. Values of the Brillouin linewidth are not presented here due to the presence of spectral broadening from the instrument. A deconvolution of the instrumental function from the Brillouin spectra is necessary in order to measure accurate Brillouin linewidths.

6.4. Spectral analysis

Peak fit analysis is often employed in the analysis of Brillouin spectra; however, for large numbers of spectra (e.g. obtained from spatial maps), this can be computationally demanding and time consuming. A biphasic system consisting of distilled water and sunflower oil was used to demonstrate the outcomes of fit analysis to a Lorentzian function, and of applying principal component analysis (PCA) and k-means cluster analysis to the data. Spectra were acquired across a 3×0.3 mm region, which encompassed the boundary of the two substances, with a 50 µm step size, and an exposure time of 1 s. These data were then analysed using a peak fitting approach, PCA, and k-means cluster analysis.

6.4.1. Peak fitting

Peak fitting enables the Brillouin frequency shift and linewidth of the spectra to be determined (as well as the peak intensity). Examples of spectra from water and oil (Figure 6.7a) show the spectral differences between the two liquids. A heatmap of these parameters from each location within the sample shows a clear separation between the two substances, with oil having a larger Brillouin frequency shift and broader linewidth than water (Figure 6.7b–d).

6.4.2. Principal component analysis

The first three principal components (PCs) obtained from PCA account for 99% of the variance in the data set (PC 1: 79%; PC 2: 19%; PC 3: 1%). The loading plot of the first principal component (PC 1; Figure 6.8a) accounts for oil, and matches closely the spectrum for oil in Figure 6.7a. This is reflected by the corresponding scores plot (Figure 6.8d), which shows a boundary between positive and negative scores, associated with the oil and water, respectively. The loading of PC 2 (Figure 6.8b) encompasses both the water and oil spectra, with the peaks corresponding to the water spectrum, and the troughs aligned to the oil. This results in a divide in the scores plot (Figure 6.8e), where positive scores relate to the spectrum of water, and negative scores to the oil spectrum. Finally, PC 3 highlights the drift in the Brillouin spectra over the measurement time, denoted by the loading plot in Figure 6.8c. The corresponding distribution of scores (Figure 6.8f) shows a shift of the entire spectrum in the centre of the map, reverting to close to its original position at the end of the

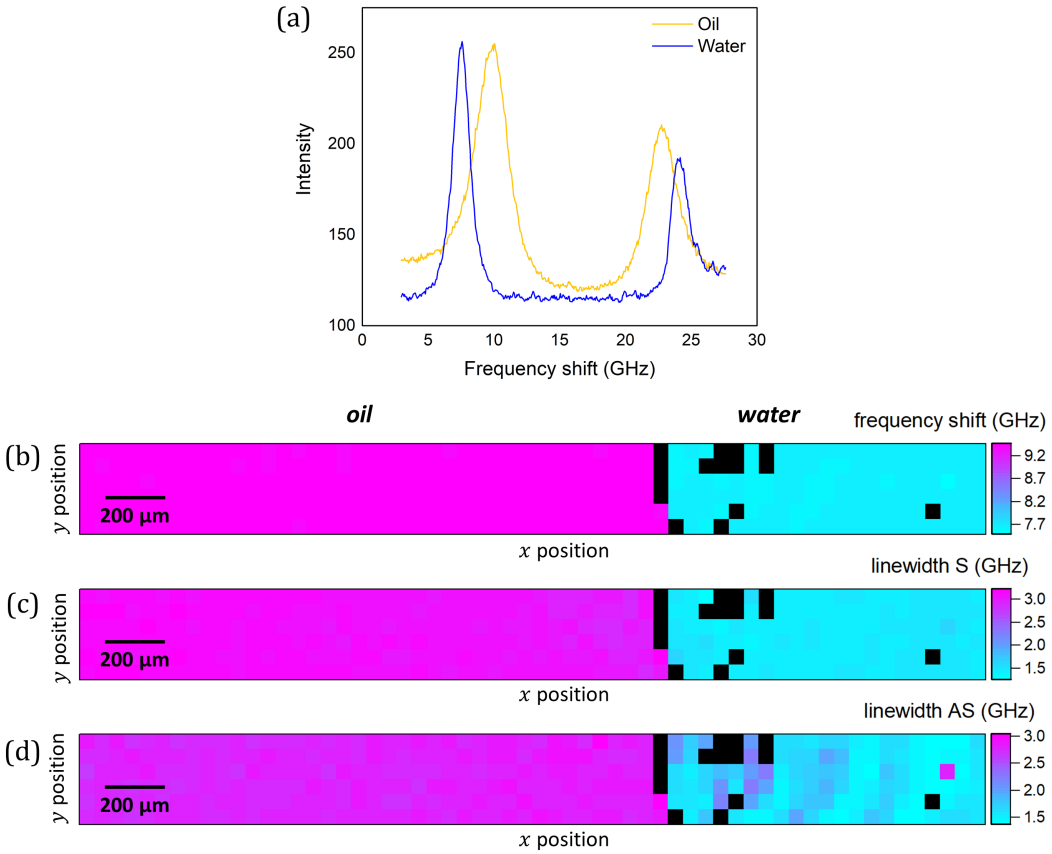

Figure 6.7.: *(a) Example spectra from water and oil with a Lorentzian fit. (b) Brillouin frequency shift and (c–d) linewidth ((c) Stokes, (d) anti-Stokes) distribution across a water:oil boundary. Black pixels correspond to points where there was high scattering intensity due to refractive index mismatch at the water-oil interface.*

map. Provided this drift remains symmetrical (i.e. the entire spectrum translates, but does not stretch or compress), the peak fit analysis is unaffected by it, since the calibration is based on the relative distance between the two Brillouin peaks. However, it is useful to keep track of the drift in spectral position on the camera chip to assess the stability of the system. The loading plot and scores (of PC 3, in this case) for each spatial position can also be used to correct for this drift post-measurement. PCA was applied with no mean centring, and the spectra were reconstructed by multiplying the scores and loadings from all principal components, apart from PC3. Even a small sample of the uncorrected spectra (Figure 6.9a), from varying times during the measurement, show a slight drift in peak position; however, reconstructing the spectra, omitting PC3, removes this drift (Figure 6.9b). In the most extreme case, reconstructing the spectra using only the first two PCs dramatically reduces the noise in the spectra, as well as removing the drift (Figure 6.10). For this two-component system, the first two PCs account for 98% of the variance within the data

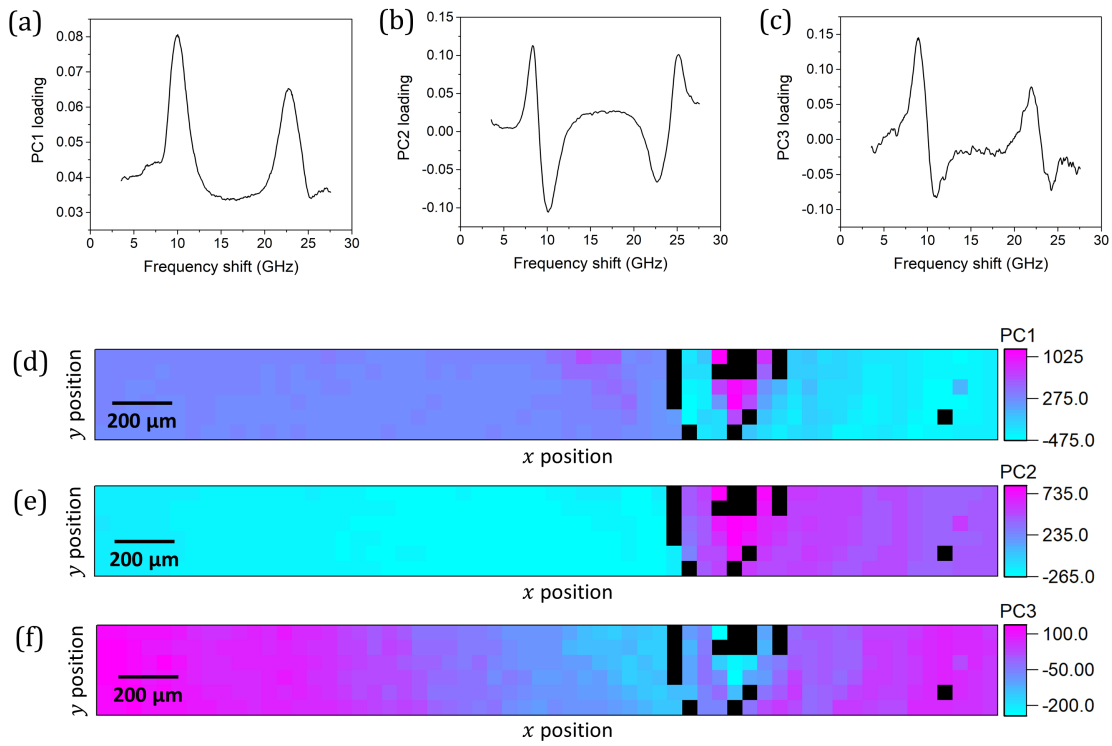

Figure 6.8.: *(a–c) Loadings and (d–f) score distributions from principal component analysis of the data, where (a,d) relate to PC 1, (b,e) PC 2 and (c,f) PC 3. Black pixels correspond to points where there was high scattering intensity due to refractive index mismatch at the water-oil interface.*

set, and account for the two components within the sample. As demonstrated, PC3 accounts for the spectral drift, and higher PCs account for noise within the data. Removing these components from the spectra, results in variance only due to the different components within the sample. However, care must be taken, particularly in more complex samples, not to "over-correct" the data.

6.4.3. k-Means cluster analysis

An alternative method of spectral analysis is k-means cluster analysis. The algorithm classifies the data into a user-defined number of clusters, enabling complex spectra to be clustered according to similarity. K-means clustering was performed on data from the boundary of water and oil, which divided the data into the specified number of clusters in such a way that minimised the total point-to-centroid distance for all points within the data set. The use of two clusters results in centroids (Figure 6.11a)

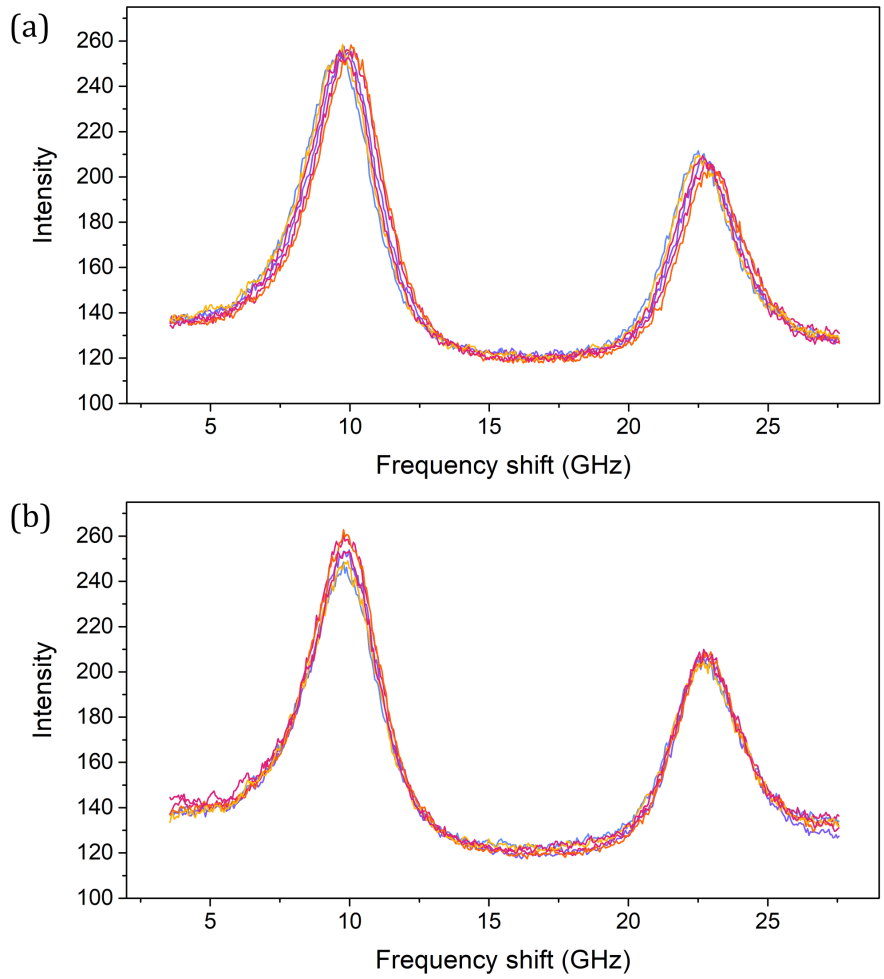

Figure 6.9.: *A selection of spectra from varying positions within the oil portion of the water:oil boundary (a) calibrated with no drift correction, and (b) drift corrected by removing PC3 from the data. (Note, that these are the Stokes and anti-Stokes peaks from adjacent spectral orders, and the frequency scale of the graph relates to the spectral order of the Stokes peak.)*

which account for water (C1) and oil (C2); however, the distribution of these clusters suggests there is a pocket of oil (C2) within the water (C1) (Figure 6.11b). Increasing the number of clusters to 4 reveals a third cluster (C3) which accounts for water, but with increased noise in the spectra (Figure 6.11b). This cluster correlates to the region in Figure 6.11c that the 2-cluster k-means analysis assigned as the "oil" cluster. Therefore, it is important (particularly in data sets containing noisy spectra) to ensure an adequate number of clusters are chosen to prevent misassignment of spectra. There are a number of analytical approaches to determining this, such as silhouette analysis [195] or the gap statistic [196]. K-means clustering has the benefit

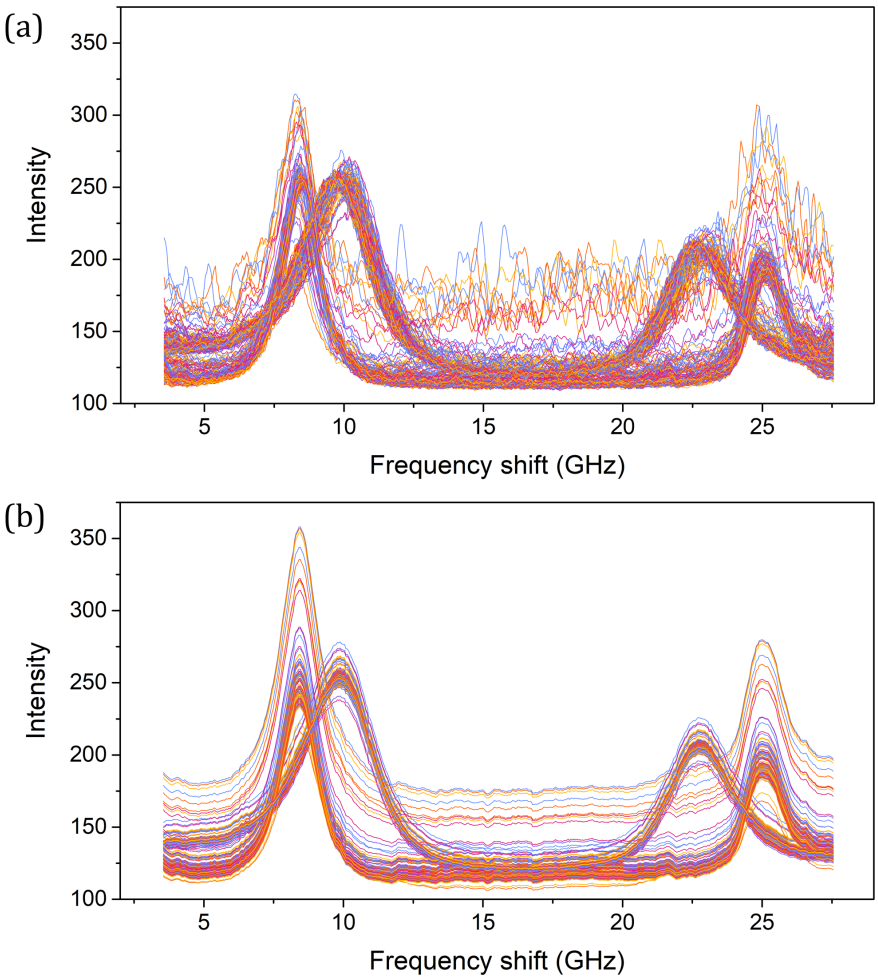

Figure 6.10.: *All spectra from the map of a water:oil boundary. (a) Calibrated spectra with no further corrections, (b) Corrected spectra, using the first two PCs only, removing noise and correcting for spectral drift. (Note, that these are the Stokes and anti-Stokes peaks from adjacent spectral orders, and the frequency scale of the graph relates to the spectral order of the Stokes peak.) Black pixels correspond to points where there was high scattering intensity due to refractive index mismatch at the water-oil interface.*

of simplifying a complicated data set into discrete clusters; however, in doing so any subtlety within the data is lost.

6.4.4. Comparison of analysis methods

Computationally, PCA and k-means clustering are considerably faster than peak fitting. For this map (60×6 pixels) two Lorentzian fits on each Brillouin spectrum (fit to Stokes and anti-Stokes components) in Matlab 2020a took $\sim$ 13 s, whereas applying PCA to the full data set took $\sim$ 0.04 s, and k-means analysis $\sim$ 0.03 s.

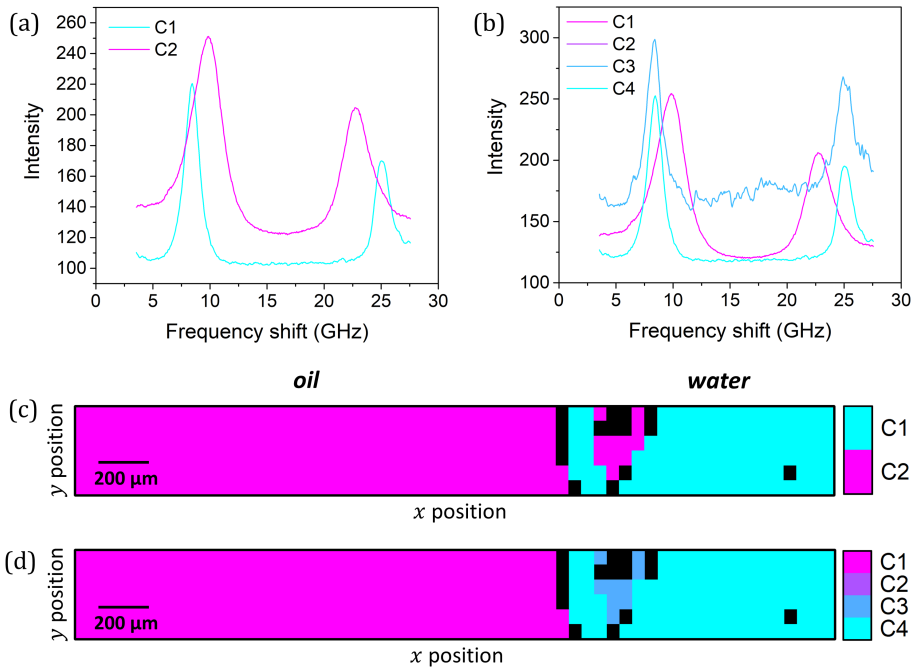

Figure 6.11.: *Plot of the centroids for k-means analysis with (a) 2 clusters and (b) 4 clusters and (c,d) corresponding cluster maps for the centroids plotted in (a) and (b), respectively.*

The time taken for fit analysis on larger maps increases with increasing map size (e.g. for a 30×30 pixel map, run time was ~ 30 s), whereas the time taken to run PCA and k-means clustering increased slightly to ~ 0.06 s and ~ 0.04 s, respectively. It should be noted that the time taken for individual peak fitting can be optimised further by utilising the parallel computing toolbox in Matlab. Doing this can reduce the time by up to a factor equal to the number of cores utilised (for example, if 4 cores were used, the time would be up to 4× quicker). In this case, using 4 cores takes the analysis time down to ~ 5 s for the 60×6 pixel map, and ~ 10 s for the larger map. This is still significantly slower than the time taken to run PCA or k-means clustering. Of course, the drawback of PCA and k-means clustering is that they must be run on the entire data set, and so cannot be used in real-time during measurement, unlike individual peak-fitting. Although more complex to interpret than k-means clustering, PCA provides more detail on the data set and provides a means of removing unwanted spectral drift and noise from the data. Having said that, there are certainly advantages to k-means clustering, predominantly in the simplicity of interpretation, and so choice of analysis method will be dependent on the sample measured. Where subtle changes are expected in the spectra, k-means clustering is probably not well-suited; however, in a sample such as hair [82] where the Brillouin

peaks are very distinct, k-means clustering could be more advantageous when reduced computational time is desired.

6.5. Imaging camera

Due to the intrinsically weak nature of the Brillouin signals, the choice of detector can greatly affect the ability to measure the Brillouin spectrum quickly and reliably. Brillouin measurements of calibration standards (methanol and distilled water) made using the sCMOS camera (Andor Zyla 4.2P-USB3, Section 6.2) were compared with those taken with a new sCMOS (Andor Sona 4.2B-6) and an EMCCD camera (Andor iXon Ultra 888). The specifications of these cameras are summarised in Table 6.2.

Table 6.2.: *Specifications for the Zyla 4.2P-USB3 sCMOS, Sona 4.2B-6 sCMOS and iXon Ultra 888 EMCCD cameras. QE_{max} is the maximum quantum efficiency.*

	Zyla	**Sona**	**iXon Ultra 888**
sensor	front-illuminated sCMOS	back-illuminated sCMOS	back-illuminated EMCCD
pixel size	6.5 µm	6.5 µm	13 µm
active pixels	2048 × 2048	2048 × 2048	1024 × 1024
$\mathbf{QE_{max}}$	82%	95%	> 95%

The Cobolt laser was used for these tests and ∼ 10% of the backscattered light was transmitted to the spectrometer. A region of interest (ROI) was selected on the camera software (Andor SOLIS) around the Brillouin peaks, allowing the Rayleigh peaks to be completely blocked from the image without diffraction, and increasing the relative intensity of the Brillouin peaks (Figure 6.12). For the Zyla, this also significantly increased the SNR at short exposure times. The EM gain of the iXON was adjusted between 0 and 650. Images were acquired at multiple exposure times, ranging from 0.01 s to 5 s, and the signal to noise ratio (SNR) was calculated for each exposure time (Figure 6.13a). For exposure times ≥ 0.5 s, the SNR of spectra obtained with the Sona camera was significantly higher than that of spectra from the other cameras. This was true for both methanol (Figure 6.13a) and distilled water (Figure B.1 in Appendix B). The Zyla gave a comparable SNR to the iXON at longer exposure times, with marginally higher SNR for strong Brillouin signals (as is the case for methanol). For both samples, the SNR of the iXON with no EM gain was

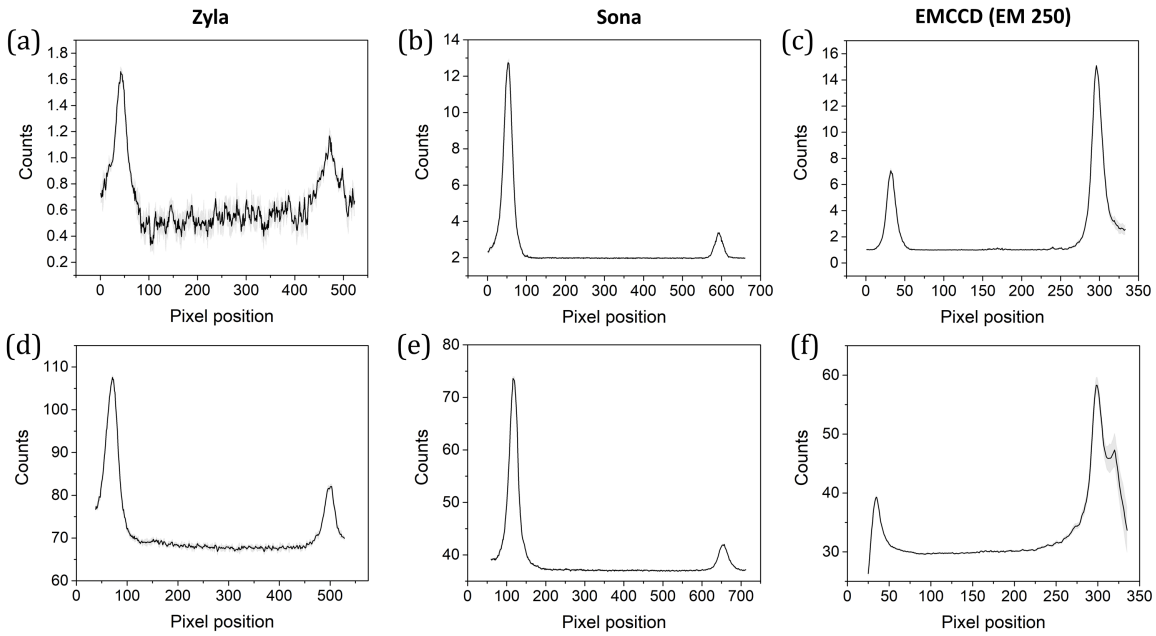

Figure 6.12.: *Brillouin spectra for methanol (0.5 s exposure) obtained using the full camera image (including Rayleigh peaks) from (a) Zyla (SNR 13 dB), (b) Sona (SNR 30 dB) and (c) iXON (EM 250; SNR 25 dB) cameras. (d–f) Corresponding spectra when a region of interest (ROI) is selected on the cameras, with SNR (d) 21 dB, (e) 28 dB and (f) 21.5 dB.*

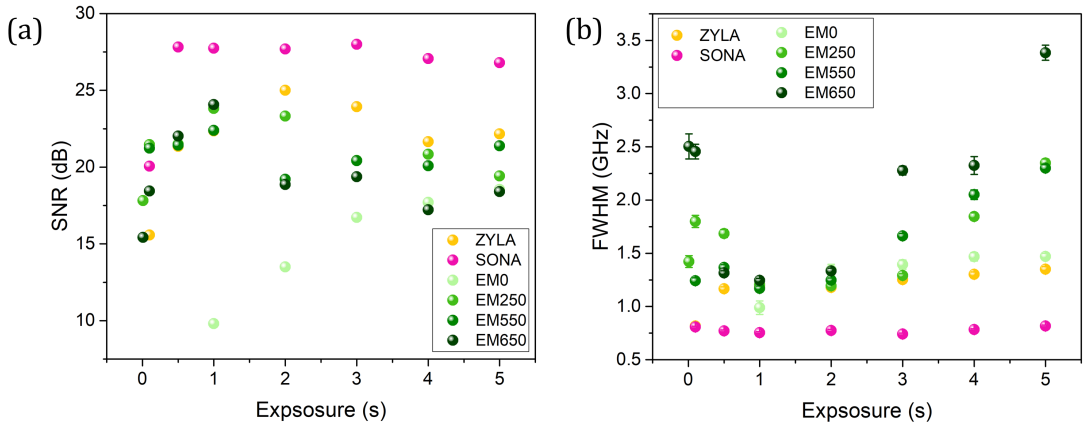

Figure 6.13.: *(a) Signal to noise ratio (SNR) and (b) linewidth (FWHM) measured for methanol as a function of exposure time, using the two sCMOS cameras: Zyla (yellow) and Sona (pink); and the EMCCD (iXon Ultra 888) with the EM gain set to 0, 250, 550 and 650 (varying shades of green).*

very poor compared to the other measurements, becoming comparable only at very long exposure times (for methanol, ≥ 4 s).

The Brillouin linewidth gives valuable information about the viscosity of the sample, and so the variation in linewidth of the spectra is an important parameter to consider. Although some spectral broadening within the system is inevitable, it is desirable to

keep this to a minimum. Plotting the full width at half maximum (FWHM) of the Brillouin peaks as a function of the exposure time for the three cameras (Figure 6.13b), shows that the Sona gives a far narrower peak than either of the other cameras, despite having the same pixel size as the Zyla. Like the SNR, it appears that the Zyla and iXon give similar linewidths, with the Zyla giving a slightly narrower linewidth when the signal is strong (i.e. for methanol), and vice versa for measurement of a weaker signal (water). It's therefore plausible that the broadening in linewidth observed when using the Zyla is an artefact of lower SNR in the spectra, whereas the broadening in the EMCCD spectra is most likely due to the larger pixel size of the camera. The broader linewidth observed with high EM gain EMCCD measurements is plausibly due to pixels reaching the full-well capacity (i.e. the largest charge the pixel can hold before saturation). Once this point is reached, charge starts to fill adjacent pixels [197], accounting for the broadening observed.

Comparing the raw spectra from the three cameras at a single exposure time, it is clear that the iXON enables faster acquisition, being the only camera tested that gave distinct Brillouin peaks at an exposure time of 0.01 s (Figure 6.14). By increasing

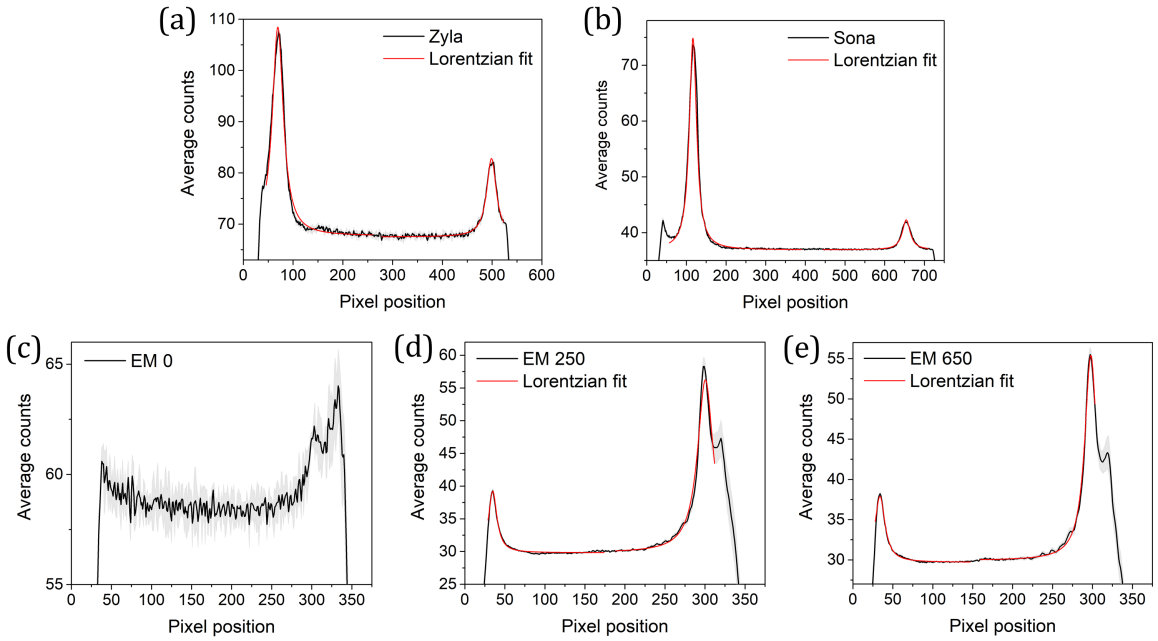

Figure 6.14.: *Spectrum for methanol acquired with an exposure time of 0.01 s for (a) the Zyla sCMOS camera, (b) Sona sCMOS, (c) EMCCD with EM gain 0, (d) EMCCD with EM gain of 250, and (e) EMCCD (iXon Ultra 888) with EM gain of 650. Where possible, a Lorentzian fit (red) has been applied to the spectra.*

the exposure time to 0.5 s (Figure 6.15), all cameras give distinct Brillouin peaks,

but as shown in Figure 6.13, the line-shape and SNR of the spectra from the Sona are significantly better than those obtained for the other two cameras.

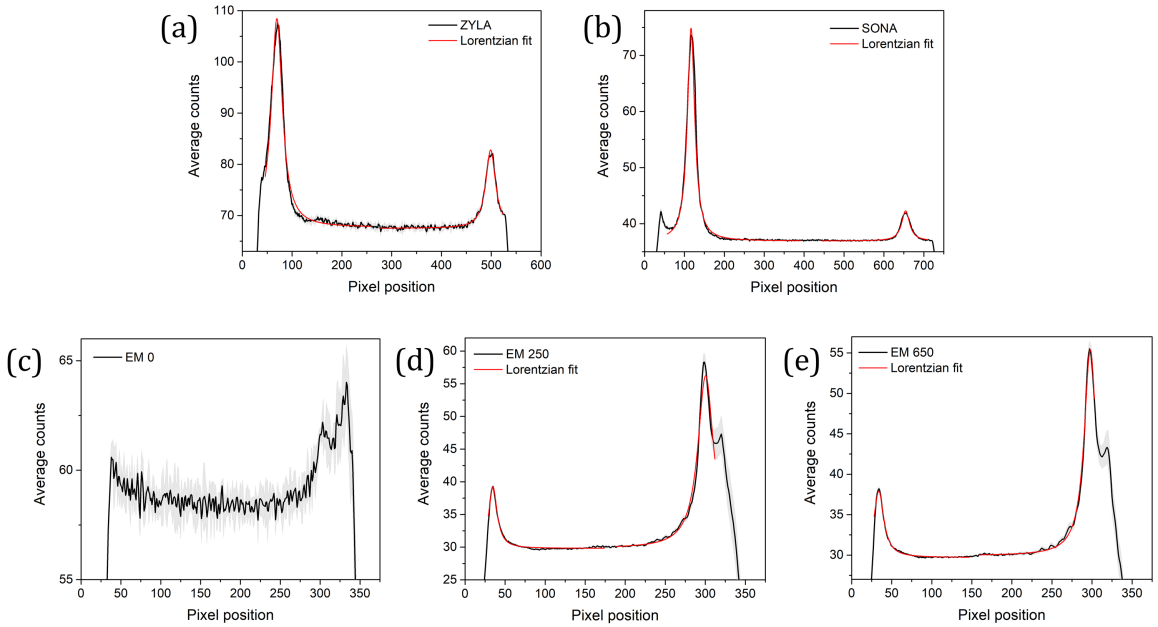

Figure 6.15.: *Spectrum for methanol acquired with an exposure time of 0.5 s for (a) the Zyla sCMOS camera, (b) Sona sCMOS, (c) iXON with EM gain 0, (d) EMCCD with EM gain of 250, and (e) EMCCD with EM gain of 650. Where possible, a Lorentzian fit (red) has been applied to the spectra.*

From the three cameras tested, it appears that there is a trade-off between speed and spectral quality. On the one hand, the iXON is superior in terms of speed of acquisition, beneficial for high-speed scanning of biological systems. However, the broader linewidth and lower SNR reduces the spectral resolution, so for measuring subtle changes (as are often seen in hydrated tissues), the Sona becomes favourable. Therefore, depending on the application, the question is whether the order of magnitude gained in speed is worth the loss in spectral resolution.

6.6. Summary

This chapter has investigated developments to a lab-built VIPA spectrometer, such as the addition of a Lyot stop, refinement of experimental protocol, and choice of laser. The system has also been used to measure the gelatin hydrogels used in Chapter 4, resulting in similar Brillouin shifts to those obtained with the TFPI-based spectrometer, but with faster acquisition times and diminished SNR. Different spectral analysis

methods have also been investigated, enabling faster analysis, and noise-reduction of the spectra. The choice of detector was also considered, and the strengths and weaknesses of an EMCCD camera versus an sCMOS camera were determined.

7. Conclusions & Future Work

This chapter contains sections from the publication "Predicting the refractive index of tissue models using light scattering spectroscopy" [2].

7.1. Summary & final discussions

This work sought to explore the development and use of Brillouin spectroscopy in the context of biomedical studies. To this end, gelatin (denatured collagen) was used as a tissue-mimicking phantom, where the density of physical and chemical cross-links could be tuned by adjusting the hydration and formalin (chemical cross-linker) concentration of the hydrogels. This provided a basis to explore the measurement capabilities of BLS, as well as investigating Raman spectroscopy as an invaluable correlative technique.

A high contrast TFPI-based Brillouin system was used to investigate the information contained within the Brillouin spectrum, using gelatin hydrogels as a case study. Hydrated gels (0–18% polymer concentration) revealed an increase in Brillouin frequency shift and linewidth with increasing polymer concentration. Refractive index measurements and determination of the density of the hydrogels confirmed that they follow the Lorentz-Lorenz equation, with an approximately constant ($< 1\%$ change) ratio of density to square-refractive index for the concentration range studied. It follows that, like the Brillouin frequency shift and linewidth, the storage and loss moduli were found to increase with increasing polymer concentration. Of note is the large relative increase (89%) in loss modulus due to hydrophobic hydration, leading to restricted mobility of water. This has a major effect on the viscoelastic response of the gels across the concentration range studied. Macro-mechanical compressive testing of hydrogels revealed an increase in the Young's modulus from a few kPa to ~ 100 kPa, in stark contrast to the 2.2–2.7 GPa range obtained for the longitudinal modulus. This emphasises the difference between the two moduli and the variation in the spatio-temporal scale probed by the two experimental techniques.

Controlling the temperature of the hydrogel allowed for Brillouin measurement during gelation. At 65°C, hydrated gelatin hydrogels are in a liquid state, and a gradual reduction in temperature down to $\sim$ 4°C caused the hydrogel to solidify. Brillouin measurements during this process revealed a small change in Brillouin frequency shift between 35 and 40°C. No discontinuity is observed in the Brillouin linewidth, and it undergoes a smooth increase as temperature is reduced. This is because a large proportion of the molecules remain in the liquid phase, which is almost unchanged by gelation, and it is their diffusive motion which dominates the picosecond dynamics measured with BLS. The small number of molecules in the solid-like portion of the sample are responsible for the small change in Brillouin frequency shift during gelation, revealing the high sensitivity of BLS to detect small changes in dilute samples, provided the resolution of the spectrometer is sufficient.

As well as physical cross-linking of the gels, the effect of the addition of a chemical cross-linker (formalin) was investigated. Contrary to that observed for physical cross-linking, the addition of a chemical cross-linker had a relatively subtle effect on the Brillouin spectra of the hydrogels. In fact, the major changes in Brillouin frequency shift and linewidth observed were likely due to changes in hydration, rather than chemical cross-links. Taking account of the changes expected due to water content revealed a discontinuity in the gradient of both frequency shift and linewidth at $\sim$ 8% formalin. Simultaneous Raman spectroscopy measurements revealed an increase in formalin content up to $\sim$ 10% formalin concentration, beyond which it remained approximately constant. This reinforces the discontinuity observed in the Brillouin spectra, suggesting that the hydrogels reach formalin saturation at 8–10% formalin.

An important parameter to consider when working with hydrogels is their stability over time. Brillouin measurements during the first 24 hours after preparation revealed that the gelatin hydrogels reached a stable state after approximately 12 h, and maintained this stability (whilst in sealed vials) for at least 12 days after preparation. Although the gels used in this work were all measured at a similar time point (24 h after preparation), it is important to note that variations of a few hours, or even days, in this time is unlikely to result in significant changes to the gel, provided that the container is sealed and free from contamination.

Dehydration of gelatin hydrogels enables the water content to be reduced to just 20% w/w, hence mimicking a wide variety of biological environments with varying mechanical properties and water content. Brillouin measurements during the dehydration of a thin film of gelatin revealed the onset of a glass-like transition at $\sim$ 40%

polymer fraction. Revealed by a sigmoidal evolution in Brillouin frequency shift and a maximum in the Brillouin linewidth, the transition from the liquid phase to the solid phase as a function of polymer volume fraction was revealed. Contrary to this, Raman spectroscopy measurements during the same dehydration process showed no evidence of a glass transition, showing only initial changes in bound and bulk water content. Raman spectroscopy probes intra-molecular vibrations, so it is unsurprising that the changes in inter-molecular mobility associated with the glass-like transition, are undetected by Raman spectroscopy. On the other hand, Brillouin scattering from acoustic phonons probes molecular motions and interactions on a larger scale, thereby enabling observation of the glass transition. It is also important to note that the timescale investigated by BLS is the most appropriate to observe such a glass transition. This highlights the potential of BLS to probe such physiologically relevant processes in biological systems, for instance, within the cellular environment, and protein aggregation in pathological states. A glass transition analogous to that observed for colloidal systems has been observed in the crowded cytoplasm of compressed cells [198], and in diseases such as Alzheimer's, Parkinsons and ALS, proteins normally forming liquid-like phases, have been found to take on more solid-like properties [199].

Recent works and discussions have sought to apply Voigt or Reuss models, derived from the rule of mixtures, to the evolution in longitudinal modulus as a function of concentration [91, 200, 201]. Following this, these models were applied to the longitudinal modulus of gelatin hydrogels as a function of polymer volume fraction, over a range of 4–30% polymer. This is a significantly larger concentration range than previously used for similar analyses [91], and in fact, it was found that the Voigt model fit the data better than the Reuss model across this larger concentration range, in contrast to what was previously presented for similar hydrogels. Although the Reuss model appeared to fit the data well in the high concentration regime, extrapolating the curve to low water content saw a divergence in the Reuss model, with $M_s \to \infty$. Applying the models instead to the evolution in acoustic wave velocity reduced the gradient of the data enough that both models fit the data well (in the hydrated regime) without severe divergence. However, neither model takes into account the glass-like transition within the hydrogels, so although they fit the data for hydrated gels well, the estimated value of the longitudinal modulus of the solute, M_s, is always underestimated. However, whether the Voigt or Reuss models are appropriate to apply to Brillouin data at all, and whether their use adds any value to the experimental data, is uncertain and sample dependent. For a homogeneous material such as a

hydrogel, the fibrous geometry assumed by the Voigt and Reuss models is not present. Therefore, the dependence on the direction of applied force in relation to the sample, which distinguishes the two models, is somewhat inconsequential for a network-like material. There is also a question of whether either geometry is appropriate for the length scales probed by BLS.

Raman spectroscopy was employed as a correlative technique to Brillouin spectroscopy. This work has revealed that not only can Raman spectroscopy be used to reveal the chemical composition of a sample, but it can also be applied to assess the refractive index of biologically relevant samples with appropriate calibration. The refractive index of gelatin hydrogels displays a linear dependence with concentration, and a similar linearity is observed in the Raman spectral intensity [specifically, of the amide I (1562–1800 cm^{-1}) and C-H stretching bands (2800–3040 cm^{-1})]. Using this calibration, the refractive index was predicted from Raman spectral intensity to within 0.3% of the value measured with Abbe refractometry, with a higher accuracy observed in the C-H stretching analysis. This is an important result that further substantiates implementations where Raman spectroscopy is applied alongside Brillouin microscopy, as it provides complementary information on the chemical and structural properties of the sample as well as, indirectly, its refractive index.

There are limitations of this work to note, predominantly that the refractive index assessment was performed on simple models of biological samples, whereas real specimens such as human tissues are heterogeneous and may present discontinuities in refractive index, for example, at interfaces. Future investigations into Raman assessments of refractive index in biomedical specimens will be needed to confirm the monitoring capacity of the model. For instance, it remains to be seen how similar approaches can be applied to generate refractive index maps overlaid to Brillouin-Raman images of biological specimens. However, the proof of principle presented here shows a great potential for future quantitative Brillouin elastography.

Having explored the measurement capabilities and applicability of TFP-BLS to biological systems, the final chapter of this work sought to focus on the development and use of a VIPA-based spectrometer. In general, VIPA etalons are seen as a faster alternative to the scanning TFP interferometer, but with reduced contrast and spectral resolution. Independent measurements of hydrated gelatin hydrogels (4–18% polymer) with both spectrometers supported this consensus; however, it should be noted that the experimental parameters used were chosen to give the best data, and not to directly compete with the other spectrometer. To this end, it would likely

be possible to reduce the acquisition times used with both spectrometers and still obtain satisfactory spectra, albeit with diminished signal-to-noise ratio. In addition to this, as mentioned in Chapter 1, improvements to VIPA-based spectrometers are frequently developed and implemented, and a lab-built system is hence subjected to continuous changes and updates. In fact, the VIPA system used to measure the hydrogels was largely comprised of just two VIPA etalons, with little else to improve the contrast or suppress the elastically scattered light. Based on this, and the results obtained, it can be said with relative certainty that a TFP interferometer has greater contrast and spectral resolution than a dual-stage VIPA spectrometer with *no added components*. In addition to this, when speed is not the main priority (i.e. the spectrometer is not pushed to its fastest acquisition speed, and is simply used to obtain good quality data), the VIPA-based system performs considerably faster than the TFP interferometer. Having said this, many VIPA-based spectrometers contain additional components to improve their performance, making it challenging to truly compare the two techniques beyond the available commercial systems.

As well as the spectrometer itself, choice of detector can also have a significant impact on the SNR and spectral line shape. To explore this further, an iXon EMCCD camera (Andor) was compared with a Sona sCMOS camera (Andor) and the existing Zyla sCMOS (an older sCMOS model than the Sona; Andor). All cameras had the same chip size; however, the iXon had a pixel size twice the size of that of the two sCMOS cameras, hence, reducing the spectral resolution. Brillouin measurements of methanol and water using each of these detectors revealed a significant difference in the SNR of the resulting spectra. For exposure times ≥ 0.5 s (for methanol), the Sona had significantly better SNR than the iXon or Zyla cameras. However, at short exposure times (< 0.5 s), the SNR of the Sona was comparable to the iXon, and the iXon was able to detect Brillouin peaks at shorter exposure times than either of the sCMOS cameras. However, the benefit of the iXon came only when the EM gain was utilised, and the spectra measured with no EM gain had very poor SNR.

Spectral line-shape is also an interesting parameter to consider in relation to the detector, since the Brillouin linewidth provides information about the micro-viscosity of the sample. Again, when all three cameras are compared, the Sona resulted in spectra with a significantly smaller linewidth than either the iXon or Zyla. Since the sample and spectrometer remained the same, the broadening observed is due solely to the detector. As was the case for the spectrometers, it appears that the different detector types have different qualities, with a choice between the faster acquisition speed allowed by an iXon, or the superior SNR and spectral resolution given by

the Sona. However, with constant advances in camera technology, a newer model of either detector type could surpass all the cameras tested here. The difference in performance between the Zyla and Sona demonstrates how much improvement there can be between an older and newer model. Of course, only three cameras were tested here (all Andor cameras), so this is by no means an exhaustive test; however, it does provide a baseline as to the relative performance that can be expected from an sCMOS vs. an EMCCD in the context of BLS.

In addition to experimental considerations, the choice of data analysis method is important in extracting the information contained within the Brillouin spectra. Here, a small sample of analysis methods have been demonstrated and compared, using Brillouin measurements of the boundary between oil and water as sample data to do this. Because most Brillouin spectra contain only one or two distinct peaks* (two or four if accounting for both Stokes and anti-Stokes peaks), peak fitting is a straightforward method of extracting and visualising the data. However, this can be computationally time consuming, especially for larger data sets. An alternative means of data analysis is principal component analysis (PCA), which reduces the data set to principal components (PCs) which encompass the variance within the sample. This was found to be, computationally, much faster than individual peak fitting, and was also able to detect spectral drift which occurred during the measurement time. Reconstructing the data from the principal components enabled the component due to spectral drift to be removed, hence removing the effect of spectral drift from the spectra. Taking this further, and removing higher PCs as well, resulted in spectra where both spectral drift and noise components had been removed, demonstrating PCA as a suitable post-processing method for Brillouin data. Of course, in more complex samples than a biphasic system, it's likely that more PCs would contribute to the true variance within the sample, and care should be taken when correcting data, that these sample variations are not overlooked and no artefacts are introduced. Another computationally quick analysis method is k-means clustering. This simplifies a complex data set into a user-defined number of clusters, enabling simple visualisation of the data. However, k-means clustering is sensitive to noise and intensity variation, so even for a two-component sample, k-means clustering with just 2 clusters did not perfectly classify the components. Increasing the number of clusters to 4, revealed a third cluster due to slightly noisy spectra near the boundary between the two components,

*Here, "distinct" refers to resolvable peaks, and excludes broader peaks comprising of signals with varying frequency shift where the individual components cannot be clearly resolved.

so providing an adequate number of clusters are used (taking care not to under-, or over-cluster the data), k-means clustering provides another computationally fast method of processing Brillouin data. Of course, the most appropriate analysis method will vary depending on the experiment and constraints. However, the analysis methods applied in this work will provide a proof-of-concept for future implementations.

7.2. Conclusions

The aims of this thesis were broad, and sought to explore the development and use of Brillouin spectroscopy within the biological environment. The first part of this work explored the measurement capabilities of Brillouin spectroscopy, revealing the concentration-induced (rather than temperature-induced) glass transition of gelatin, which, to the author's knowledge, is the first demonstration of such a phenomenon using BLS. In addition to this, Brillouin spectroscopy was able to measure subtle changes in the viscoelastic properties of gelatin during gelation, demonstrating a high sensitivity to small changes in the storage modulus in diluted samples.

The second part of this thesis aimed to investigate the use of correlative techniques, in particular, Raman spectroscopy. Simultaneous Brillouin-Raman measurements of chemically cross-linked hydrogels revealed the mechanical and chemical composition of the samples. This demonstrated how the two techniques combined can be beneficial in elucidating the mechano-chemistry of the samples, in this case substantiating the saturation point of formalin in the hydrogels. Raman spectroscopy proved useful, not only in determining chemical composition, but also in monitoring the refractive index of gelatin hydrogels through a calibration model. This proof-of-principle demonstration, revealed how simultaneous Brillouin-Raman measurements could be beneficial in monitoring the refractive index within the sample, a necessary parameter to decouple the optical and mechanical properties contained within Brillouin spectra.

The final part of this thesis focused on development, using a dual-stage VIPA-based spectrometer to introduce experimental improvements and analytical methods. Measurements of gelatin hydrogels confirmed the perception that VIPA-based spectrometers are generally faster, but have poorer contrast and resolution than TFPI-based spectrometers. However, it is important to note that this is based on a simple VIPA-based spectrometer design, with little else present to improve the contrast and remove the elastically scattered light. Compared to spectrometer design, relatively little work has been done to date on analytical methods used to process Brillouin data. Using

Brillouin measurements of the boundary between an oil and water drop as sample data, PCA and k-means clustering analysis were found to be effective alternatives to peak fitting when processing spectral maps consisting of many spectra. PCA was also demonstrated as a means of correcting the spectral drift present in the data, as well as removing noise from the spectra, which could be beneficial in itself as a pre-processing method. The choice of detector used in Brillouin measurements was also investigated, and it was found that for the Brillouin system utilised, the EM-CCD camera was able to detect Brillouin spectra up to an order of magnitude faster than the sCMOS; however, the sCMOS introduced less spectral broadening, proving beneficial for linewidth analysis.

7.3. Perspectives and future work

The application of Brillouin spectroscopy to biological samples has grown tremendously in the last 15 years. Even in the last 5 years, the number of publications has increased substantially. This says a lot about the progression of the field, and although it is not yet a widely used technique within the biosciences, it is proving itself as a valuable tool to probe the micro-scale viscoelasticity of samples.

Throughout this thesis, gelatin hydrogels have been used as model biological systems to explore the measurement capabilities of BLS and simultaneous Raman spectroscopy. It is important to highlight that these serve only as simple models, and real biological tissues are far more complex. Further work is now needed to apply these techniques to more complex biological samples. Since glassy behaviour has previously been observed in the cytoplasm of cells [198], Brillouin measurements on a similar system would be an interesting application for the glass-like transition observed in this thesis.

On a more general level, measurements on *ex vivo* tissue sections make a logical next step to further relating this work to the biological milieu. This is truly where the benefits of correlative Raman spectroscopy can be demonstrated. Similarly, the analysis methods described in Chapter 6 can be utilised more fully with the more complex spectral maps obtained from tissue sections. As discussed in Chapter 1, there have already been numerous studies of various biological tissue types [66–70, 75, 76]; however, the fundamental work presented in this thesis will provide the basis for further investigations, particularly in relation to the effect of hydration in the biological milieu.

With a more local focus on spectrometer design, a number of improvements are available that have not been included in the Brillouin microscope system used in this thesis. Most significant would be suppression of the elastically scattered light, as this is often the main limitation in measuring highly scattering samples. Future inclusion of a notch filter for spectral filtering will further improve this system, enabling the measurement of highly scattering samples (such is the case for many biological tissues).

As a non-contact, label-free microscopic technique, BLS, in combination with complementary techniques such as Raman spectroscopy, has the potential to make a real impact on the biological field, through integration with medical pathways, use in plant biology, tissue engineering and more. The future of BLS is an exciting one, and the formation of the International BioBrillouin Society will likely be paramount in supporting its evolution and success.

Appendices

A. Glass transition

Extract from the publication "Viscoelastic properties of biopolymer hydrogels determined by Brillouin spectroscopy: A probe of tissue mechanics" [1]. The viscoelastic model described was developed by Daniele Fioretto.

The glass transition is a dynamic process that occurs as an abrupt increase in the structural relaxation time, leading the system out of equilibrium (ergodic to nonergodic transition) [182]. In the framework of MCT, the transition is induced by a slowdown of density fluctuations, which, in the frequency domain, can be described by the complex frequency-dependent longitudinal modulus $M(\omega) = M'(\omega) + iM''(\omega)$. Close to the glass transition, a stretched exponential relaxation of the longitudinal modulus typically occurs, described by the Kohlrausch-Williams-Watts (KWW) law: $e^{(-t/\tau)\beta}$, where τ is the characteristic time and $\beta < 1$ is the stretching parameter. In the frequency domain, the Fourier transform of the KWW law can be conveniently described by a Havriliak-Negami relaxation function [202]

$$\frac{M(\omega)}{\rho} = c_\infty^2 - \frac{c_\infty^2 - c_0^2}{[1 + (i\omega\tau)^a]^b} \tag{A.1}$$

where c_0 and c_∞ are the relaxed (low frequency ω or low τ with respect to the Brillouin frequency, such as in the high hydration regime) and unrelaxed (high ω or high τ, low hydration) sound velocities; a and b are the stretching parameters determined by the value of the KWW β parameter [202]. The MCT, in its basic formulation, predicts a power law divergence of the relaxation time $\tau \propto (-\epsilon)^{-\gamma}$ and a square root singularity of the amplitude of the structural relaxation (nonergodicity parameter) $1 - c_0^2/c_\infty^2 = f_q = f_q^c + h_q\sqrt{\epsilon}$ for the control parameter $\epsilon \to 0$. The nonergodicity parameter f_q quantifies the arrest of density fluctuations in the nonergodic state. Depending on the experimental path, the control parameter can be expressed in terms of temperature (thermal vitrification) or density (pressure vitrification) or volume fraction of polymer molecules in the case of colloidal suspensions [182]. Here, we define it in terms of volume fraction of collagen molecules x as $\epsilon = (x - x_0)/x_0$, where x_0 is the "ideal" critical concentration for the structural arrest. According to MCT, the values of the parameters regulating the stretching of the relaxation time

depend only on the structure of the sample and are mutually related by well-defined analytical expressions [203]. Measuring these parameters give a quantitative test of the predictions of the theory.

Brillouin spectra from longitudinal acoustic modes are informative of $M(\omega)$ and can be used to test the predictions of the MCT, since they give direct access to the spectrum of density fluctuations (fluctuation-dissipation theorem) [204]

$$I_q(\omega) = \frac{I_0}{\omega}\zeta\{[M(\omega)/\rho - \omega^2/q^2]^{-1}\} \tag{A.2}$$

This equation, where ζ denotes the imaginary part, shows that the maximum of information (maximum intensity) in the Brillouin spectrum is the resonance (Brillouin peak) occurring around $\omega_B = (q^2 M'(\omega_B)/\rho)^{1/2}$. Unfortunately, the fit of a single Brillouin spectrum to this equation is not sufficient to get the whole set of relaxation parameters c_0, c_∞, τ and β. Different strategies can be implemented to mitigate this problem [205]. In the present work, we expanded the frequency range by collecting light from two simultaneous scattering geometries (see Chapter 3). In this case, the measured spectrum is given by the sum of two Brillouin peaks:

$$I_q^{TOT}(\omega) = I_{qS}(\omega) + I_{qB}(\omega) \tag{A.3}$$

where subscripts qs and qB refer to the parallel to surface and bulk modes, respectively. Further improvement to the fitting procedure was obtained by fixing $n(x)$, $c_0(x)$ and $\beta(x)$ to values obtained from extrapolation of limiting behaviours, as described below.

In a narrow region around the frequency of Brillouin peaks ω_B, one can approximate the spectrum of density fluctuations to a DHO function [205]:

$$I_q(\omega) = I_0 \frac{\omega_B^2 \Gamma_B}{(\omega_B^2 - \omega^2)^2 - (\omega\Gamma_B)^2} \tag{A.4}$$

where $\omega_B^2 = q^2 M'(\omega_B)/\rho$ and $\omega\Gamma_B = q^2 M''(\omega_B)/\rho + \omega\Gamma_\infty$, with $M'(\omega_B)$ and $M''(\omega_B)$ being the real and imaginary parts of the modulus at the single frequency of the Brillouin peak, and Γ_∞ the unrelaxed part of kinematic viscosity.

Brillouin measurements were used to determine the refractive indices of the hydrogel during dehydration, and these were compared with those derived from a linear extrapolation of $1/n^2$ from Abbe refractometry of hydrated gels (Chapter 4, Figure 4.11a). As expected, Brillouin data confirm the refractometry data in relaxed (low x) and

unrelaxed (high x) conditions, validating the linear extrapolation of $1/n^2$. The rationale for this linear extrapolation can further be found in an almost constant ration n^2/ρ (Chapter 4). In the following elaboration, we will fix $n(x)$ according to this law. Notice that in the intermediate x region, the presence of the relaxation process is associated with the frequency dependence of the modulus, responsible for the breakdown of the simple relation $n = (\omega_{0B}/\omega_{0S}) \sin\theta/2$. In this condition, Brillouin peaks will be most sensitive to the values of the relaxation parameters.

The next step for the characterisation of the glass transition is the determination of the relaxed sound velocity, $c_0(x)$. Using the Voigt fit described in Chapter 3, we obtained values for the longitudinal modulus in this relaxed regime, $M_0(x)$. The concentration dependence of c_0 is then obtained as $c_0(x) = M_0(x)/\rho)^{1/2}$.

A reasonable estimation for the value of the stretching parameter β can be obtained from the Cole-Cole plot of the imaginary vs. real part of the elastic modulus [206], shown in Figure A.1.

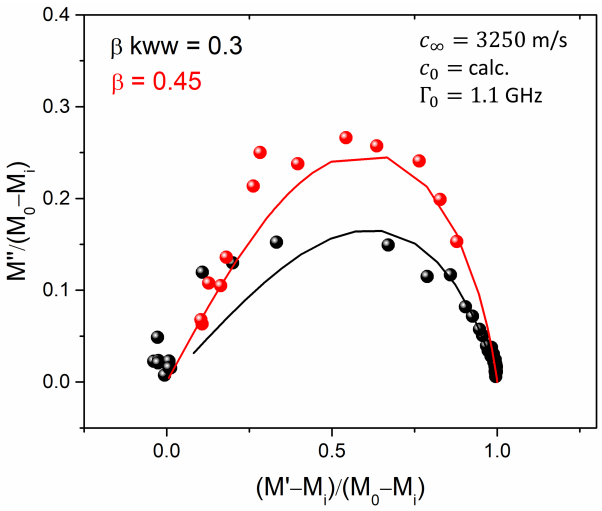

Figure A.1.: *Cole-Cole plot of the imaginary vs. real part of the elastic moduli. M' and M'' were obtained from DHO fit of the BLS peaks of bulk phonons. By an iterative process, in first approximation black dots were calculated fixing c_∞ to the limiting high concentration value $c_\infty = 3250$ m/s and subtracting a constant unrelaxed contribution $\Gamma_\infty = 1.1$ GHz from the measured linewidths. In this representation, the single exponential relaxation would give a semicircle. Conversely, the shrunk shape of the curve is evidence of a stretched exponential behaviour. A good representation of the data can be obtained using a stretching parameter $\beta \approx 0.3$ (solid line). This value was fixed to fit Brillouin spectra to equations (A.3) (A.4) and (A.1). A better approximation for $c_\infty(x)$ was thus obtained and used, in the second iteration, to recalculate the Cole-Cole plot (red dots), giving a β parameter of 0.45. This value was ultimately used to fit the Brillouin spectra.*

Fixing the values of ρ, n, c_0 as described previously, and $\beta = 0.45$ as explained in Figure A.1, we can now fit the Brillouin spectra, both bulk and parallel to surface modes, to equations (A.3) (A.4) and (A.1), leaving only c_∞ and τ as free parameters. From the fit, the concentration dependence of the relaxation time τ and of the nonergodicity parameter $1 - c_0^2/c_\infty^2$ was obtained and is reported in Figure A.2 to be compared with the predictions of the MCT.

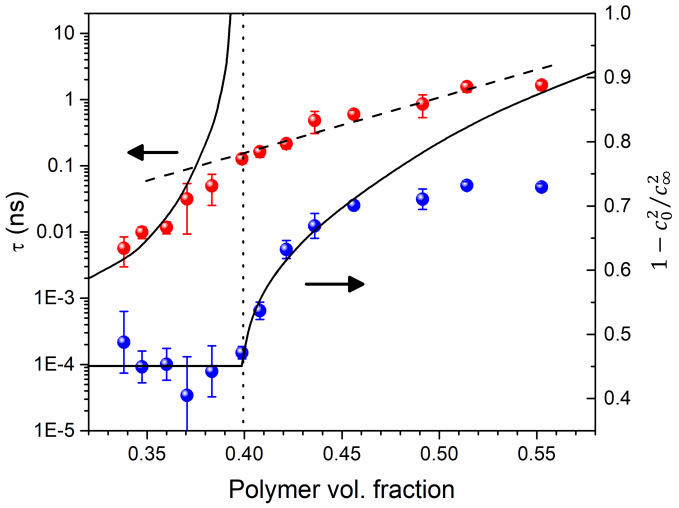

Figure A.2.: *Plot of the relaxation time τ and nonergodicity parameter $f = 1 - c_0^2/c_\infty^2$ vs. polymer volume fraction x. Deviations of data points (full circles) from ideal behaviour (solid lines) can be explained by secondary relaxation processes, which are relevant for real systems. Dashed line is a guide for the eye, and dotted line denotes the ideal critical concentration for the structural arrest predicted by MCT.*

Although the system investigated here is by far more complex than the liquids and colloidal suspensions usually analysed with MCT, signatures of a critical concentration x_0 located around 40% polymer can be clearly seen in Figure A.2. In particular, f_q shows an inflection close to x_0, with an increase at higher concentrations that mimics the square root behaviour predicted by the theory (solid line). Moreover, at lower concentrations, τ follows the power law behaviour predicted by the theory, with an exponent γ of approximately 4, the value related by MCT to the stretching parameter of the structural relaxation $\beta = 0.45$. The deviation from the power law visible in Figure A.2 when approaching the critical point is quite typical for all glass-forming systems [182] and attributed to the presence of additional (secondary) relaxation processes responsible for restoring ergodicity above x_c.

As a whole, these results are in good agreement with the predictions of the MCT for the glass transition, which was previously verified in simple glass formers through

more traditional thermodynamic paths, namely, with temperature as the control parameter [182]. This was previously verified as a function of temperature [207, 208] and pressure [209], upon hardening of epoxy glues [181] and astonishingly here in the hardening of "kolla" controlled by changing concentration.

B. Camera testing data: water

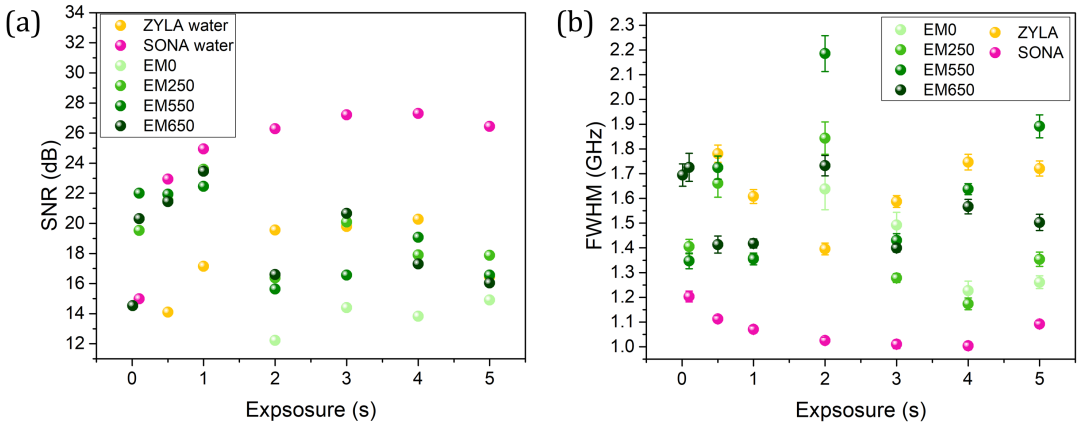

Figure B.1.: *(a) Signal to noise ratio (SNR) and (b) linewidth (FWHM) measured for distilled water as a function of exposure time, using the two sCMOS cameras: Zyla (yellow) and SONA (pink); and the EMCCD (iXon Ultra 888) with the EM gain set to 0, 250, 550 and 650 (varying shades of green).*

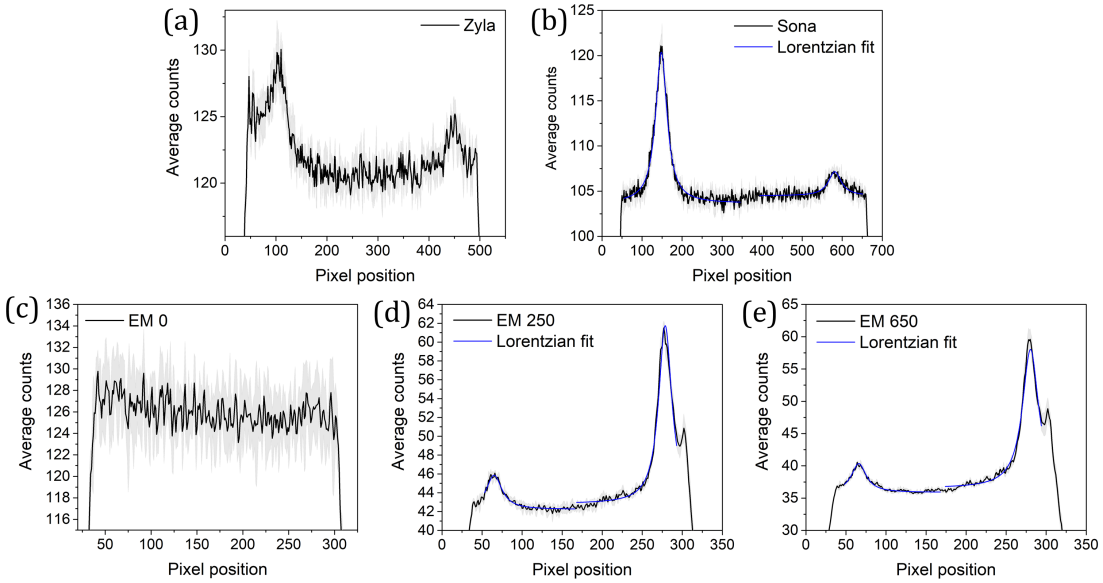

Figure B.2.: *Spectrum for distilled water acquired with an exposure time of 0.1 s for (a) the ZYLA sCMOS camera, (b) SONA sCMOS, (c) EMCCD (iXon Ultra 888) with EM gain 0, (d) EMCCD with EM gain of 250, and (e) EMCCD with EM gain of 650. Where possible, a Lorentzian fit (red) has been applied to the spectra.*

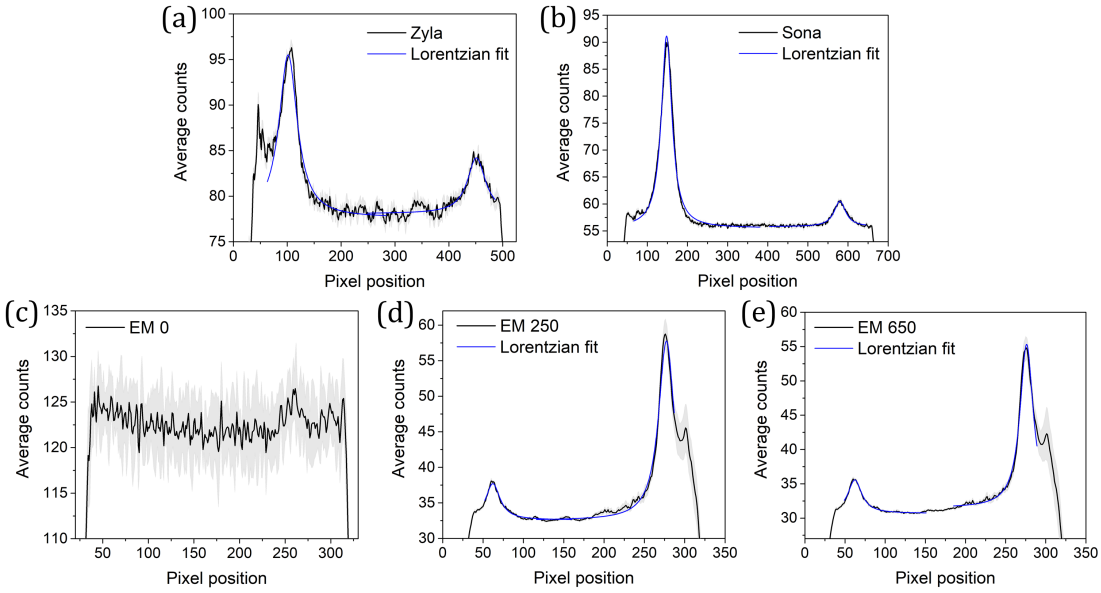

Figure B.3.: *Spectrum for distilled water acquired with an exposure time of 0.5 s for (a) the ZYLA sCMOS camera, (b) SONA sCMOS, (c) EMCCD with EM gain 0, (d) EMCCD with EM gain of 250, and (e) EMCCD with EM gain of 650. Where possible, a Lorentzian fit (red) has been applied to the spectra.*

Bibliography

[1] M. Bailey, M. Alunni-Cardinali, N. Correa, S. Caponi, T. Holsgrove, H. Barr, N. Stone, C. P. Winlove, D. Fioretto, F. Palombo, 'Viscoelastic properties of biopolymer hydrogels determined by Brillouin spectroscopy: A probe of tissue micromechanics', in *Science advances* **2020**, *6*, eabc1937, (cit. on pp. 1, 18, 33, 91).

[2] M. Bailey, B. Gardner, M. Alunni-Cardinali, S. Caponi, D. Fioretto, N. Stone, F. Palombo, 'Predicting the refractive index of tissue models using light scattering spectroscopy', in *Applied Spectroscopy* **2021**, *75*, 574–580, (cit. on pp. 1, 18, 51, 81).

[3] K. H. Vining, D. J. Mooney, 'Mechanical forces direct stem cell behaviour in development and regeneration', in *Nature reviews Molecular cell biology* **2017**, *18*, 728–742, (cit. on p. 1).

[4] V. Swaminathan, K. Mythreye, E. T. O'Brien, A. Berchuck, G. C. Blobe, R. Superfine, 'Mechanical stiffness grades metastatic potential in patient tumor cells and in cancer cell lines', in *Cancer research* **2011**, *71*, 5075–5080, (cit. on p. 1).

[5] J. M. Northcott, I. S. Dean, J. K. Mouw, V. M. Weaver, 'Feeling stress: the mechanics of cancer progression and aggression', in *Frontiers in cell and developmental biology* **2018**, *6*, 17, (cit. on p. 1).

[6] M. Krieg, G. Fläschner, D. Alsteens, B. M. Gaub, W. H. Roos, G. J. Wuite, H. E. Gaub, C. Gerber, Y. F. Dufrêne, D. J. Müller, 'Atomic force microscopy-based mechanobiology', in *Nature Reviews Physics* **2019**, *1*, 41–57, (cit. on p. 1).

[7] H. G. Hansma, 'Surface biology of DNA by atomic force microscopy', in *Annual review of physical chemistry* **2001**, *52*, 71–92, (cit. on p. 1).

[8] T. G. Kuznetsova, M. N. Starodubtseva, N. I. Yegorenkov, S. A. Chizhik, R. I. Zhdanov, 'Atomic force microscopy probing of cell elasticity', in *Micron* **2007**, *38*, 824–833, (cit. on p. 1).

[9] R. M. Hochmuth, 'Micropipette aspiration of living cells', in *Journal of biomechanics* **2000**, *33*, 15–22, (cit. on p. 1).

[10] K. Guevorkian, J.-L. Maître, 'Micropipette aspiration: A unique tool for exploring cell and tissue mechanics in vivo', in *Methods in cell biology* **2017**, *139*, 187–201, (cit. on p. 1).

[11] L. M. Lee, A. P. Liu, 'The application of micropipette aspiration in molecular mechanics of single cells', in *Journal of nanotechnology in engineering and medicine* **2014**, *5*, (cit. on p. 1).

[12] P.-H. Wu, D. R.-B. Aroush, A. Asnacios, W.-C. Chen, M. E. Dokukin, B. L. Doss, P. Durand-Smet, A. Ekpenyong, J. Guck, N. V. Guz et al., 'A comparison of methods to assess cell mechanical properties', in *Nature methods* **2018**, *15*, 491–498, (cit. on p. 1).

[13] N. Redhu, D. Rastogi, A. Yadav, S. Hariprasad, Z. Jigar, S. Tripathi, S. Gupta, D. Chawla, 'Ultrasound elastography–Review', in *Current Medicine Research and Practice* **2015**, *5*, 67–71, (cit. on p. 1).

[14] R. M. Sigrist, J. Liau, A. El Kaffas, M. C. Chammas, J. K. Willmann, 'Ultrasound elastography: review of techniques and clinical applications', in *Theranostics* **2017**, *7*, 1303, (cit. on pp. 1, 23).

[15] J.-L. Gennisson, T. Deffieux, M. Fink, M. Tanter, 'Ultrasound elastography: principles and techniques', in *Diagnostic and interventional imaging* **2013**, *94*, 487–495, (cit. on p. 1).

[16] L. Brillouin in Annales de physique, *Vol. 9*, **1922**, pp. 88–122 (cit. on pp. 1, 2, 11).

[17] L. Mandelstam, 'Light scattering by inhomogeneous media', in *Zh. Russ. Fiz-Khim. Ova* **1926**, *58*, 146, (cit. on p. 2).

[18] L. Brillouin in Light Scattering Spectra of Solids, (Ed.: G. B. Wright), Proceedings of the International Conference on Light Scattering Spectra of Solids held at: New York University, New York September 3, 4, 5, 6, 1968, Springer Science & Business Media, **1969** (cit. on p. 2).

[19] L. Brillouin, in *Comptes rendus* **1914**, *158*, 1331–1334, (cit. on p. 2).

[20] D. Rank, 'Brillouin effect in liquids in the prelaser era', in *The Journal of the Acoustical Society of America* **1971**, *49*, 937–940, (cit. on pp. 2, 3).

[21] E. Gross, 'über Änderung der WellenlÄnge bei Lichtzerstreuung in Kristallen', in *Zeitschrift für Physik* **1930**, *63*, 685–687, (cit. on pp. 2, 3).

[22] I. L. Fabelinskiĭ, 'The prediction and discovery of Rayleigh line fine structure', in *Physics-Uspekhi* **2000**, *43*, 89, (cit. on pp. 2, 3).

[23] E. Gross, 'Change of wave-length of light due to elastic heat waves at scattering in liquids', in *Nature* **1930**, *126*, 201–202, (cit. on p. 3).

[24] F. Kargar, A. A. Balandin, 'Advances in Brillouin–Mandelstam light-scattering spectroscopy', in *Nature Photonics* **2021**, 1–12, (cit. on p. 3).

[25] D. S. Bedborough, D. Jackson, 'Brillouin scattering study of gelatin gel using a double passed Fabry-Perot spectrometer', in *Polymer* **1976**, *17*, 573–576, (cit. on pp. 3, 5, 35).

[26] R. Harley, D. James, A. Miller, J. White, 'Phonons and the elastic moduli of collagen and muscle', in *Nature* **1977**, *267*, 285, (cit. on pp. 3–5).

[27] S. Cusack, A. Miller, 'Determination of the elastic constants of collagen by Brillouin light scattering', in *Journal of molecular biology* **1979**, *135*, 39–51, (cit. on pp. 3, 4).

[28] J. Vaughan, J. Randall, 'Brillouin scattering, density and elastic properties of the lens and cornea of the eye', in *Nature* **1980**, *284*, 489–491, (cit. on pp. 3, 4).

[29] G. Scarcelli, S. H. Yun, 'Confocal Brillouin microscopy for three-dimensional mechanical imaging', in *Nature photonics* **2008**, *2*, 39, (cit. on pp. 3, 5, 61, 62).

[30] R. Prevedel, A. Diz-Muñoz, G. Ruocco, G. Antonacci, 'Brillouin microscopy: an emerging tool for mechanobiology', in *Nature methods* **2019**, *16*, 969–977, (cit. on p. 3).

[31] K. Elsayad, S. Polakova, J. Gregan, 'Probing Mechanical Properties in Biology Using Brillouin Microscopy', in *Trends in cell biology* **2019**, *29*, 608–611, (cit. on p. 3).

[32] F. Palombo, D. Fioretto, 'Brillouin Light Scattering: Applications in Biomedical Sciences', in *Chemical reviews* **2019**, *119*, 7833–7847, (cit. on pp. 3, 26).

[33] G. Antonacci, T. Beck, A. Bilenca, J. Czarske, K. Elsayad, J. Guck, K. Kim, B. Krug, F. Palombo, R. Prevedel, 'Recent progress and current opinions in Brillouin microscopy for life science applications', in **2020**, (cit. on pp. 3, 6).

[34] C. Poon, J. Chou, M. Cortie, I. Kabakova, 'Brillouin imaging for studies of micromechanics in biology and biomedicine: from current state-of-the-art to future clinical translation', in *Journal of Physics: Photonics* **2020**, *3*, 012002, (cit. on p. 3).

[35] R. J. J. Rioboó, N. Gontán, D. Sanderson, M. Desco, M. V. Gómez-Gaviro, 'Brillouin Spectroscopy: From Biomedical Research to New Generation Pathology Diagnosis', in *International Journal of Molecular Sciences* **2021**, *22*, 8055, (cit. on p. 3).

[36] Z. Meng, A. J. Traverso, C. W. Ballmann, M. A. Troyanova-Wood, V. V. Yakovlev, 'Seeing cells in a new light: a renaissance of Brillouin spectroscopy', in *Advances in Optics and Photonics* **2016**, *8*, 300–327, (cit. on p. 3).

[37] S. Caponi, A. Passeri, G. Capponi, D. Fioretto, M. Vassalli, M. Mattarelli, 'Non-contact elastography methods in mechanobiology: A point of view', in *European Biophysics Journal* **2021**, 1–6, (cit. on p. 3).

[38] J. Marqusee, J. Deutch, 'Brillouin light scattering from polymer gels', in *The Journal of Chemical Physics* **1981**, *75*, 5239–5245, (cit. on p. 3).

[39] J. Jarry, G. Patterson, 'Brillouin scattering from polyepoxide solutions and gels', in *Macromolecules* **1981**, *14*, 1281–1284, (cit. on p. 3).

[40] A. Bot, R. Schram, G. Wegdam, 'Brillouin light scattering from a biopolymer gel: hypersonic sound waves in gelatin', in *Colloid and polymer science* **1995**, *273*, 252–256, (cit. on pp. 3, 35).

[41] P. Zhao, J. Vanderwal, 'Brillouin scattering study of gelatin gel', in *Polymer Gels and Networks* **1997**, *5*, 23–36, (cit. on p. 3).

[42] H. Mahmodi, A. Piloni, R. H. Utama, I. Kabakova, 'Mechanical mapping of bioprinted hydrogel models by brillouin microscopy', in *Bioprinting* **2021**, *23*, e00151, (cit. on p. 3).

[43] D. Akilbekova, T. Yakupov, V. Ogay, B. Umbayev, V. V. Yakovlev, Z. N. Utegulov in Optical Elastography and Tissue Biomechanics V, *Vol. 10496*, International Society for Optics and Photonics, p. 104961I (cit. on p. 3).

[44] G. Scarcelli, P. Kim, S. H. Yun, 'In vivo measurement of age-related stiffening in the crystalline lens by Brillouin optical microscopy', in *Biophysical journal* **2011**, *101*, 1539–1545, (cit. on p. 4).

[45] R. Stephan, B. Gerolf, S. Oliver, G. Rudolf, S. Heinrich, 'Spatially resolved Brillouin spectroscopy to determine the rheological properties of the eye lens', in *Biomed. Opt. Express* **2011**, *2*, 2144–2159, DOI 10.1364/BOE.2.002144, (cit. on pp. 4, 62).

[46] G. Scarcelli, R. Pineda, S. H. Yun, 'Brillouin optical microscopy for corneal biomechanics', in *Investigative ophthalmology & visual science* **2012**, *53*, 185–190, (cit. on p. 4).

[47] S. Giuliano, Y. Seok Hyun, 'In vivo Brillouin optical microscopy of the human eye', in *Opt. Express* **2012**, *20*, 9197–9202, DOI 10.1364/OE.20.009197, (cit. on p. 4).

[48] J. N. Webb, J. P. Su, G. Scarcelli, 'Mechanical outcome of accelerated corneal crosslinking evaluated by Brillouin microscopy', in *Journal of Cataract & Refractive Surgery* **2017**, *43*, 1458–1463, (cit. on p. 4).

[49] P. Shao, A. M. Eltony, T. G. Seiler, B. Tavakol, R. Pineda, T. Koller, T. Seiler, S.-H. Yun, 'Spatially-resolved Brillouin spectroscopy reveals biomechanical changes in early ectatic corneal disease and post-crosslinking in vivo', in *arXiv preprint arXiv:1802.01055* **2018**, (cit. on p. 4).

[50] T. G. Seiler, P. Shao, A. Eltony, T. Seiler, S.-H. Yun, 'Brillouin spectroscopy of normal and keratoconus corneas', in *American journal of ophthalmology* **2019**, *202*, 118–125, (cit. on p. 4).

[51] J. N. Webb, H. Zhang, A. S. Roy, J. B. Randleman, G. Scarcelli, 'Detecting mechanical anisotropy of the cornea using Brillouin microscopy', in *Translational Vision Science & Technology* **2020**, *9*, 26–26, (cit. on p. 4).

[52] A. M. Eltony, P. Shao, S.-H. Yun in Optical Elastography and Tissue Biomechanics VIII, *Vol. 11645*, (Eds.: K. V. Larin, G. Scarcelli), International Society for Optics and Photonics, SPIE, **2021** (cit. on p. 4).

[53] R. Mercatelli, S. Mattana, L. Capozzoli, F. Ratto, F. Rossi, R. Pini, D. Fioretto, F. S. Pavone, S. Caponi, R. Cicchi, 'Morpho-mechanics of human collagen superstructures revealed by all-optical correlative micro-spectroscopies', in *Communications biology* **2019**, *2*, 1–10, (cit. on p. 4).

[54] Corneal Biomechanical Analysis Using Brillouin Microscopy, Available at https://ichgcp.net/clinical-trials-registry/NCT04598932 (26/01/2022) (cit. on p. 4).

[55] G. Scarcelli, W. J. Polacheck, H. T. Nia, K. Patel, A. J. Grodzinsky, R. D. Kamm, S. H. Yun, 'Noncontact three-dimensional mapping of intracellular hydromechanical properties by Brillouin microscopy', in *Nature methods* **2015**, *12*, 1132–1134, (cit. on p. 4).

[56] S. Mattana, M. Mattarelli, L. Urbanelli, K. Sagini, C. Emiliani, M. Dalla Serra, D. Fioretto, S. Caponi, 'Non-contact mechanical and chemical analysis of single living cells by microspectroscopic techniques', in *Light: Science & Applications* **2018**, *7*, 17139–17139, (cit. on pp. 4, 6).

[57] J. Zhang, X. A. Nou, H. Kim, G. Scarcelli, 'Brillouin flow cytometry for label-free mechanical phenotyping of the nucleus', in *Lab on a Chip* **2017**, *17*, 663–670, (cit. on pp. 4, 6).

[58] K. Elsayad, S. Werner, M. Gallemí, J. Kong, E. R. S. Guajardo, L. Zhang, Y. Jaillais, T. Greb, Y. Belkhadir, 'Mapping the subcellular mechanical properties of live cells in tissues with fluorescence emission–Brillouin imaging', in *Science signaling* **2016**, *9*, rs5–rs5, (cit. on pp. 4, 6).

[59] M. Nikolić, G. Scarcelli, 'Long-term Brillouin imaging of live cells with reduced absorption-mediated damage at 660nm wavelength', in *Biomedical optics express* **2019**, *10*, 1567–1580, (cit. on pp. 4, 6).

[60] G. Antonacci, S. Braakman, 'Biomechanics of subcellular structures by non-invasive Brillouin microscopy', in *Scientific reports* **2016**, *6*, 37217, (cit. on pp. 4, 8).

[61] M. A. Taylor, A. W. Kijas, Z. Wang, J. Lauko, A. E. Rowan, 'Heterodyne Brillouin microscopy for biomechanical imaging', in *Biomedical Optics Express* **2021**, *12*, 6259–6268, (cit. on p. 4).

[62] R. Schlüßler, S. Möllmert, S. Abuhattum, G. Cojoc, P. Müller, K. Kim, C. Möckel, C. Zimmermann, J. Czarske, J. Guck, 'Mechanical mapping of spinal cord growth and repair in living zebrafish larvae by brillouin imaging', in *Biophysical journal* **2018**, *115*, 911–923, (cit. on pp. 4, 8).

[63] C. Bevilacqua, H. Sánchez-Iranzo, D. Richter, A. Diz-Muñoz, R. Prevedel, 'Imaging mechanical properties of sub-micron ECM in live zebrafish using Brillouin microscopy', in *Biomedical Optics Express* **2019**, *10*, 1420–1431, (cit. on pp. 4, 6, 7).

[64] I. Remer, R. Shaashoua, N. Shemesh, A. Ben-Zvi, A. Bilenca, 'High-sensitivity and high-specificity biomechanical imaging by stimulated Brillouin scattering microscopy', in *Nature Methods* **2020**, 1–4, (cit. on pp. 4, 7).

[65] Z. Steelman, Z. Meng, A. J. Traverso, V. V. Yakovlev, 'Brillouin spectroscopy as a new method of screening for increased CSF total protein during bacterial meningitis', in *Journal of Biophotonics* **2015**, *8*, 408–414, (cit. on p. 4).

[66] F. Palombo, M. Madami, N. Stone, D. Fioretto, 'Mechanical mapping with chemical specificity by confocal Brillouin and Raman microscopy', in *Analyst* **2014**, *139*, 729–733, (cit. on pp. 4, 6, 8, 88).

[67] F. Palombo, M. Madami, D. Fioretto, J. Nallala, H. Barr, A. David, N. Stone, 'Chemico-mechanical imaging of Barrett's oesophagus', in *Journal of Biophotonics* **2016**, *9*, 694–700, DOI 10.1002/jbio.201600038, (cit. on pp. 4, 6, 51, 88).

[68] S. Ryu, N. Martino, S. J. Kwok, L. Bernstein, S.-H. Yun, 'Label-free histological imaging of tissues using Brillouin light scattering contrast', in *Biomedical optics express* **2021**, *12*, 1437–1448, (cit. on pp. 4, 88).

[69] S. Mattana, S. Caponi, F. Tamagnini, D. Fioretto, F. Palombo, 'Viscoelasticity of amyloid plaques in transgenic mouse brain studied by Brillouin microspectroscopy and correlative Raman analysis', in *Journal of innovative optical health sciences* **2017**, *10*, 1742001, (cit. on pp. 4, 31, 88).

[70] G. Antonacci, R. M. Pedrigi, A. Kondiboyina, V. V. Mehta, R. De Silva, C. Paterson, R. Krams, P. Török, 'Quantification of plaque stiffness by Brillouin microscopy in experimental thin cap fibroatheroma', in *Journal of the Royal Society Interface* **2015**, *12*, 20150843, (cit. on pp. 4, 88).

[71] M. Troyanova-Wood, Z. Meng, V. V. Yakovlev, 'Differentiating melanoma and healthy tissues based on elasticity-specific Brillouin microspectroscopy', in *Biomedical optics express* **2019**, *10*, 1774–1781, (cit. on p. 4).

[72] J. Margueritat, A. Virgone-Carlotta, S. Monnier, H. Delanoë-Ayari, H. C. Mertani, A. Berthelot, Q. Martinet, X. Dagany, C. Rivière, J.-P. Rieu, 'High-frequency mechanical properties of tumors measured by Brillouin light scattering', in *Physical review letters* **2019**, *122*, 018101, (cit. on p. 4).

[73] C. Conrad, K. M. Gray, K. M. Stroka, I. Rizvi, G. Scarcelli, 'Mechanical Characterization of 3D Ovarian Cancer Nodules Using Brillouin Confocal Microscopy', in *Cellular and Molecular Bioengineering* **2019**, 1–12, (cit. on p. 4).

[74] G. Yan, S. Monnier, M. Mouelhi, T. Dehoux, 'Probing molecular crowding in compressed tissues with Brillouin light scattering', in *Proceedings of the National Academy of Sciences* **2022**, *119*, (cit. on p. 4).

[75] P.-J. Wu, M. I. Masouleh, D. Dini, C. Paterson, P. Török, D. R. Overby, I. V. Kabakova, 'Detection of proteoglycan loss from articular cartilage using Brillouin microscopy, with applications to osteoarthritis', in *Biomedical optics express* **2019**, *10*, 2457–2466, (cit. on pp. 4, 88).

[76] M. Cardinali, D. Dallari, M. Govoni, C. Stagni, F. Marmi, M. Tschon, S. Brogini, D. Fioretto, A. Morresi, 'Brillouin micro-spectroscopy of subchondral, trabecular bone and articular cartilage of the human femoral head', in *Biomedical optics express* **2019**, *10*, 2606–2611, (cit. on pp. 4, 45, 88).

[77] M. Alunni Cardinali, A. Morresi, D. Fioretto, L. Vivarelli, D. Dallari, M. Govoni, 'Brillouin and Raman Micro-Spectroscopy: A Tool for Micro-Mechanical and Structural Characterization of Cortical and Trabecular Bone Tissues', in *Materials* **2021**, *14*, 6869, (cit. on p. 4).

[78] M. Alunni Cardinali, A. Di Michele, M. Mattarelli, S. Caponi, M. Govoni, D. Dallari, S. Brogini, F. Masia, P. Borri, W. Langbein et al., 'Brillouin–Raman microspectroscopy for the morpho-mechanical imaging of human lamellar bone', in *Journal of the Royal Society Interface* **2021**, (cit. on p. 4).

[79] T. Lainović, J. Margueritat, Q. Martinet, X. Dagany, L. Blažić, D. Pantelić, M. D. Rabasović, A. J. Krmpot, T. Dehoux, 'Micromechanical imaging of dentin with Brillouin microscopy', in *Acta Biomaterialia* **2020**, *105*, 214–222, (cit. on p. 4).

[80] J. T. Randall, J. M. Vaughan, 'Brillouin scattering in systems of biological significance', in *Philosophical Transactions of the Royal Society of London. Series A Mathematical and Physical Sciences* **1979**, *293*, 341–348, (cit. on p. 4).

[81] C. J. Chan, C. Bevilacqua, R. Prevedel, 'Mechanical mapping of mammalian follicle development using Brillouin microscopy', in *Communications biology* **2021**, *4*, 1133, DOI 10.1038/s42003-021-02662-5, (cit. on p. 4).

[82] N. Correa, M. Alunni Cardinali, M. Bailey, D. Fioretto, P. D. Pudney, F. Palombo, 'Brillouin microscopy for the evaluation of hair micromechanics and effect of bleaching', in *Journal of Biophotonics* **2021**, e202000483, (cit. on pp. 4, 75).

[83] D. Fioretto, S. Caponi, F. Palombo, 'Brillouin-Raman mapping of natural fibers with spectral moment analysis', in *Biomedical optics express* **2019**, *10*, 1469–1474, (cit. on p. 4).

[84] D. R. Williams, D. J. Nurco, N. Rahbar, K. J. Koski, 'Elasticity of bamboo fiber variants from Brillouin spectroscopy', in *Materialia* **2019**, *5*, 100240, (cit. on p. 4).

[85] K. Elsayad, G. Urstöger, C. Czibula, C. Teichert, J. Gumulec, J. Balvan, M. Pohlt, U. Hirn, 'Mechanical Properties of cellulose fibers measured by Brillouin spectroscopy', in *Cellulose* **2020**, 1–12, (cit. on pp. 4, 8).

[86] S. Lees, N.-J. Tao, S. Lindsay, 'Studies of compact hard tissues and collagen by means of Brillouin light scattering', in *Connective tissue research* **1990**, *24*, 187–205, (cit. on pp. 4, 8).

[87] C. Morin, C. Hellmich, P. Henits, 'Fibrillar structure and elasticity of hydrating collagen: a quantitative multiscale approach', in *Journal of theoretical biology* **2013**, *317*, 384–393, (cit. on p. 4).

[88] F. Palombo, C. P. Winlove, R. S. Edginton, E. Green, N. Stone, S. Caponi, M. Madami, D. Fioretto, 'Biomechanics of fibrous proteins of the extracellular matrix studied by Brillouin scattering', in *Journal of The Royal Society Interface* **2014**, *11*, 20140739, (cit. on pp. 4, 8).

[89] R. S. Edginton, S. Mattana, S. Caponi, D. Fioretto, E. Green, C. P. Winlove, F. Palombo, 'Preparation of extracellular matrix protein fibers for Brillouin spectroscopy', in *Journal of visualized experiments: JoVE* **2016**, (cit. on p. 4).

[90] K. J. Koski, P. Akhenblit, K. McKiernan, J. L. Yarger, 'Non-invasive determination of the complete elastic moduli of spider silks', in *Nature Materials* **2013**, *12*, 262, (cit. on p. 4).

[91] P.-J. Wu, I. V. Kabakova, J. W. Ruberti, J. M. Sherwood, I. E. Dunlop, C. Paterson, P. Török, D. R. Overby, 'Water content, not stiffness, dominates Brillouin spectroscopy measurements in hydrated materials', in *Nature methods* **2018**, *15*, 561, (cit. on pp. 4, 5, 47, 83).

[92] V. C. Mow, C. C. Wang, C. T. Hung, 'The extracellular matrix, interstitial fluid and ions as a mechanical signal transducer in articular cartilage', in *Osteoarthritis and Cartilage* **1999**, *7*, 41–58, (cit. on p. 4).

[93] C. Frantz, K. M. Stewart, V. M. Weaver, 'The extracellular matrix at a glance', in *J Cell Sci* **2010**, *123*, 4195–4200, (cit. on p. 4).

[94] M. Guo, A. F. Pegoraro, A. Mao, E. H. Zhou, P. R. Arany, Y. Han, D. T. Burnette, M. H. Jensen, K. E. Kasza, J. R. Moore, 'Cell volume change through water efflux impacts cell stiffness and stem cell fate', in *Proceedings of the National Academy of Sciences* **2017**, 201705179, (cit. on p. 4).

[95] Y. L. Han, A. F. Pegoraro, H. Li, K. Li, Y. Yuan, G. Xu, Z. Gu, J. Sun, Y. Hao, S. K. Gupta, 'Cell swelling, softening and invasion in a three-dimensional breast cancer model', in *Nature Physics* **2020**, *16*, 101–108, (cit. on p. 4).

[96] M. Urbanska, H. E. Muñoz, J. S. Bagnall, O. Otto, S. R. Manalis, D. Di Carlo, J. Guck, 'A comparison of microfluidic methods for high-throughput cell deformability measurements', in *Nature Methods* **2020**, *17*, 587–593, (cit. on p. 4).

[97] K. M. Stroka, H. Jiang, S.-H. Chen, Z. Tong, D. Wirtz, S. X. Sun, K. Konstantopoulos, 'Water permeation drives tumor cell migration in confined microenvironments', in *Cell* **2014**, *157*, 611–623, (cit. on p. 4).

[98] S. Adichtchev, Y. A. Karpegina, K. Okotrub, M. Surovtseva, V. Zykova, N. Surovtsev, 'Brillouin spectroscopy of biorelevant fluids in relation to viscosity and solute concentration', in *Physical Review E* **2019**, *99*, 062410, (cit. on pp. 5, 7).

[99] J. R. Sandercock, *Light Scattering in Solids III*, (Eds.: M. Cardona, G. Guntherodt), **1982**, Chapter 2 (cit. on pp. 5, 11).

[100] S. Lindsay, M. Anderson, J. Sandercock, 'Construction and alignment of a high performance multipass vernier tandem Fabry–Perot interferometer', in *Review of scientific instruments* **1981**, *52*, 1478–1486, (cit. on p. 5).

[101] F. Scarponi, S. Mattana, S. Corezzi, S. Caponi, L. Comez, P. Sassi, A. Morresi, M. Paolantoni, L. Urbanelli, C. Emiliani, 'High-performance versatile setup for simultaneous Brillouin-Raman microspectroscopy', in *Physical Review X* **2017**, *7*, 031015, (cit. on pp. 5, 6, 25, 51).

[102] M. Shirasaki, 'Large angular dispersion by a virtually imaged phased array and its application to a wavelength demultiplexer', in *Optics letters* **1996**, *21*, 366–368, (cit. on p. 5).

[103] G. Scarcelli, S. H. Yun, 'Multistage VIPA etalons for high-extinction parallel Brillouin spectroscopy', in *Optics express* **2011**, *19*, 10913–10922, (cit. on pp. 5, 61).

[104] K. V. Berghaus, S. H. Yun, G. Scarcelli, 'High speed sub-GHz spectrometer for Brillouin scattering analysis', in *Journal of visualized experiments: JoVE* **2015**, (cit. on pp. 5, 67).

[105] K. Berghaus, J. Zhang, S. H. Yun, G. Scarcelli, 'High-finesse sub-GHz-resolution spectrometer employing VIPA etalons of different dispersion', in *Optics letters* **2015**, *40*, 4436–4439, (cit. on p. 5).

[106] J. Zhang, A. Fiore, S.-H. Yun, H. Kim, G. Scarcelli, 'Line-scanning Brillouin microscopy for rapid non-invasive mechanical imaging', in *Scientific reports* **2016**, *6*, 1–8, (cit. on p. 5).

[107] G. Antonacci, G. Lepert, C. Paterson, P. Török, 'Elastic suppression in Brillouin imaging by destructive interference', in *Applied Physics Letters* **2015**, *107*, 061102, (cit. on p. 5).

[108] A. Fiore, J. Zhang, P. Shao, S. H. Yun, G. Scarcelli, 'High-extinction virtually imaged phased array-based Brillouin spectroscopy of turbid biological media', in *Applied physics letters* **2016**, *108*, 203701, (cit. on p. 5).

[109] P. Shao, S. Besner, J. Zhang, G. Scarcelli, S.-H. Yun, 'Etalon filters for Brillouin microscopy of highly scattering tissues', in *Optics express* **2016**, *24*, 22232–22238, (cit. on p. 5).

[110] M. Zhaokai, J. T. Andrew, V. Y. Vladislav, 'Background clean-up in Brillouin microspectroscopy of scattering medium', in *Opt. Express* **2014**, *22*, 5410–5415, DOI 10.1364/OE.22.005410, (cit. on p. 5).

[111] G. Antonacci, S. De Panfilis, G. Di Domenico, E. DelRe, G. Ruocco, 'Breaking the contrast limit in single-pass fabry-pérot spectrometers', in *Physical Review Applied* **2016**, *6*, 054020, (cit. on p. 5).

[112] E. Edrei, M. C. Gather, G. Scarcelli, 'Integration of spectral coronagraphy within VIPA-based spectrometers for high extinction Brillouin imaging', in *Optics express* **2017**, *25*, 6895–6903, (cit. on pp. 5, 64).

[113] Z. Coker, M. Troyanova-Wood, A. J. Traverso, T. Yakupov, Z. N. Utegulov, V. V. Yakovlev, 'Assessing performance of modern Brillouin spectrometers', in *Optics express* **2018**, *26*, 2400–2409, (cit. on p. 6).

[114] G. Yan, A. Bazir, J. Margueritat, T. Dehoux, 'Evaluation of commercial virtually imaged phase array and Fabry-Pérot based Brillouin spectrometers for applications to biology', in *Biomedical optics express* **2020**, *11*, 6933–6944, (cit. on p. 6).

[115] J. R. Sandercock, VIPA vs. TFP - putting the record straight, *Plenary talk at 5th BioBrillouin meeting*, 12-14 Oct. **2021**, (cit. on p. 6).

[116] G. Antonacci, M. R. Foreman, C. Paterson, P. Török, 'Spectral broadening in Brillouin imaging', in *Applied Physics Letters* **2013**, *103*, 221105, (cit. on pp. 6, 12).

[117] S. Caponi, D. Fioretto, M. Mattarelli, 'On the actual spatial resolution of Brillouin Imaging', in *Opt. Lett.* **2020**, *45*, 1063–1066, DOI 10.1364/OL.385072, (cit. on pp. 6, 31).

[118] Y. Xiang, M. R. Foreman, P. Török, 'SNR enhancement in Brillouin microspectroscopy using spectrum reconstruction', in *Biomedical optics express* **2020**, *11*, 1020–1031, (cit. on p. 6).

[119] Y. Xiang, K. L. C. Seow, C. Paterson, P. Török, 'Multivariate analysis of Brillouin imaging data by supervised and unsupervised learning', in *Journal of Biophotonics* **2021**, e2723, (cit. on p. 6).

[120] K. Elsayad, 'Spectral phasor analysis for Brillouin microspectroscopy', in *Frontiers in Physics* **2019**, *7*, 62, (cit. on p. 6).

[121] M. Mattarelli, G. Capponi, A. A. Passeri, D. Fioretto, S. Caponi, Brillouin imaging in turbid samples: the removal of multiple scattering contribution, **2021** (cit. on p. 6).

[122] R. Schlüßler, K. Kim, M. Nötzel, A. V. Taubenberger, S. Abuhattum, T. Beck, P. Müller, S. Maharana, G. Cojoc, S. Girardo, A. Hermann, S. Alberti, J. Guck, 'Correlative all-optical quantification of mass density and mechanics of sub-cellular compartments with fluorescence specificity', in *bioRxiv* **2022**, DOI 10.1101/2020.10.30.361808, (cit. on pp. 6, 8).

[123] S. La Cavera, F. Pérez-Cota, R. J. Smith, M. Clark, 'Phonon imaging in 3D with a fibre probe', in *Light: Science & Applications* **2021**, *10*, 1–13, (cit. on pp. 6, 7).

[124] Y. Xiang, C. Basirun, J. Chou, M. E. Warkiani, P. Török, Y. Wang, S. Gao, I. V. Kabakova, 'Background-free fibre optic Brillouin probe for remote mapping of micromechanics', in *Biomedical optics express* **2020**, *11*, 6687–6698, (cit. on p. 6).

[125] I. V. Kabakova, Y. Xiang, C. Paterson, P. Török, 'Fiber-integrated Brillouin microspectroscopy: towards Brillouin endoscopy', in *Journal of Innovative Optical Health Sciences* **2017**, *10*, 1742002, (cit. on p. 6).

[126] J. Zhang, G. Scarcelli, 'Mapping mechanical properties of biological materials via an add-on Brillouin module to confocal microscopes', in *Nature protocols* **2021**, *16*, 1251–1275, (cit. on p. 7).

[127] C. W. Ballmann, J. V. Thompson, A. J. Traverso, Z. Meng, M. O. Scully, V. V. Yakovlev, 'Stimulated Brillouin scattering microscopic imaging', in *Scientific Reports* **2015**, *5*, 1–7, (cit. on p. 7).

[128] I. Remer, L. Cohen, A. Bilenca, 'High-speed continuous-wave stimulated Brillouin scattering spectrometer for material analysis', in *Journal of visualized experiments: JoVE* **2017**, (cit. on p. 7).

[129] B. Krug, N. Koukourakis, J. W. Czarske, 'Impulsive stimulated Brillouin microscopy for non-contact, fast mechanical investigations of hydrogels', in *Optics express* **2019**, *27*, 26910–26923, (cit. on p. 7).

[130] C. W. Ballmann, Z. Meng, A. J. Traverso, M. O. Scully, V. V. Yakovlev, 'Impulsive brillouin microscopy', in *Optica* **2017**, *4*, 124–128, (cit. on p. 7).

[131] R. G. Maev, *Acoustic microscopy: Fundamentals and applications*, John Wiley & Sons, **2008**, Chapter 1 (cit. on p. 7).

[132] C. F. Quate, A. Atalar, H. Wickramasinghe, 'Acoustic microscopy with mechanical scanning—a review', in *Proceedings of the IEEE* **1979**, *67*, 1092–1114, (cit. on p. 7).

[133] Z. Yu, S. Boseck, 'Scanning acoustic microscopy and its applications to material characterization', in *Reviews of Modern Physics* **1995**, *67*, 863, (cit. on p. 7).

[134] F. Perez-Cota, R. J. Smith, E. Moradi, L. Marques, K. F. Webb, M. Clark, 'Thin-film optoacoustic transducers for subcellular Brillouin oscillation imaging of individual biological cells', in *Applied optics* **2015**, *54*, 8388–8398, (cit. on p. 7).

[135] V. E. Gusev, P. Ruello, 'Advances in applications of time-domain Brillouin scattering for nanoscale imaging', in *Applied Physics Reviews* **2018**, *5*, 031101, (cit. on p. 7).

[136] S. La Cavera, F. Pérez-Cota, R. Fuentes-Domınguez, R. J. Smith, M. Clark, 'Time resolved Brillouin fiber-spectrometer', in *Optics Express* **2019**, *27*, 25064–25071, (cit. on p. 7).

[137] L. Comez, L. Lupi, M. Paolantoni, F. Picchiò, D. Fioretto, 'Hydration properties of small hydrophobic molecules by Brillouin light scattering', in *The Journal of chemical physics* **2012**, *137*, 114509, (cit. on pp. 8, 39).

[138] M. Bailey, N. Correa, S. Harding, N. Stone, S. Brasselet, F. Palombo, 'Brillouin microspectroscopy data of tissue-mimicking gelatin hydrogels', in *Data in brief* **2020**, *29*, 105267, (cit. on pp. 8, 61).

[139] M. Schürmann, G. Cojoc, S. Girardo, E. Ulbricht, J. Guck, P. Müller, 'Three-dimensional correlative single-cell imaging utilizing fluorescence and refractive index tomography', in *Journal of biophotonics* **2018**, *11*, e201700145, (cit. on p. 8).

[140] K. Kim, J. Guck, 'The relative densities of cytoplasm and nuclear compartments are robust against strong perturbation', in *Biophysical Journal* **2020**, *119*, 1946–1957, (cit. on p. 8).

[141] A. Fiore, C. Bevilacqua, G. Scarcelli, 'Direct three-dimensional measurement of refractive index via dual photon-phonon scattering', in *Physical review letters* **2019**, *122*, 103901, (cit. on p. 8).

[142] M. Diem, *Modern vibrational spectroscopy and micro-spectroscopy: theory, instrumentation and biomedical applications*, John Wiley & Sons, **2015** (cit. on pp. 11, 16).

[143] B. J. Berne, R. Pecora, *Dynamic light scattering: with applications to chemistry, biology, and physics*, Courier Corporation, **2000**, Chapter 3 (cit. on p. 11).

[144] E. Smith, G. Dent, *Modern Raman spectroscopy: a practical approach*, John Wiley & Sons, **2005**, Chapter 3 (cit. on pp. 11, 15–17).

[145] M. Cardona, *Light Scattering in Solids II*, (Eds.: M. Cardona, G. Guntherodt), **1982**, Chapter 2 (cit. on p. 11).

[146] J. F. Nye, *Physical properties of crystals: their representation by tensors and matrices*, Oxford university press, **1957**, Chapter VIII (cit. on pp. 13, 14).

[147] J. D. Ferry, *Viscoelastic properties of polymers*, John Wiley & Sons, **1961**, Chapter 1 (cit. on p. 13).

[148] T. A. Litovitz, C. M. Davis, *Properties of gases, liquids, and solutions*, (Ed.: W. P. Mason), Academic Press Inc., **1965**, Chapter 5 (cit. on p. 13).

[149] F. I. Fedorov, 'Theory of Elastic Waves in Crystals', trans. by J. E. S. Bradley, in **1968**, (cit. on p. 14).

[150] C. V. Raman, K. S. Krishnan, 'A new type of secondary radiation', in *Nature* **1928**, *121*, 501–502, (cit. on p. 15).

[151] E. Smith, G. Dent, *Modern Raman spectroscopy: a practical approach*, John Wiley & Sons, **2005**, Chapter 1 (cit. on p. 15).

[152] J. Gross, 'Organization and disorganization of collagen', in *Biophysical journal* **1964**, *4*, 63, (cit. on pp. 18, 33).

[153] X. Lou, T. V. Chirila, 'Swelling behavior and mechanical properties of chemically cross-linked gelatin gels for biomedical use', in *Journal of biomaterials applications* **1999**, *14*, 184–191, (cit. on p. 18).

[154] L. Guo, R. H. Colby, C. P. Lusignan, T. H. Whitesides, 'Kinetics of triple helix formation in semidilute gelatin solutions', in *Macromolecules* **2003**, *36*, 9999–10008, (cit. on p. 18).

[155] S. Gorgieva, V. Kokol, 'Collagen-vs. gelatine-based biomaterials and their biocompatibility: review and perspectives', in *Biomaterials applications for nanomedicine* **2011**, *2*, 17–52, (cit. on p. 18).

[156] A. Duconseille, T. Astruc, N. Quintana, F. Meersman, V. Sante-Lhoutellier, 'Gelatin structure and composition linked to hard capsule dissolution: A review', in *Food hydrocolloids* **2015**, *43*, 360–376, (cit. on p. 18).

[157] P. Davis, B. Tabor, 'Kinetic study of the crosslinking of gelatin by formaldehyde and glyoxal', in *Journal of Polymer Science Part A: General Papers* **1963**, *1*, 799–815, (cit. on p. 19).

[158] T. Hakata, H. SATo, Y. WATANABE, M. MATSUMOTO, 'Effect of formaldehyde on the physicochemical properties of soft gelatin capsule shells', in *Chemical and pharmaceutical bulletin* **1994**, *42*, 1138–1142, (cit. on p. 19).

[159] E. A. Hoffman, B. L. Frey, L. M. Smith, D. T. Auble, 'Formaldehyde crosslinking: a tool for the study of chromatin complexes', in *Journal of Biological Chemistry* **2015**, *290*, 26404–26411, (cit. on p. 19).

[160] T. Salsa, M. Pina, J. Teixeira-Dias, 'Crosslinking of gelatin in the reaction with formaldehyde: An FT-IR spectroscopic study', in *Applied spectroscopy* **1996**, *50*, 1314–1318, (cit. on p. 19).

[161] A. Taffel, 'CCXXXVI.—Thermal expansion of gelatin gels', in *Journal of the Chemical Society Transactions* **1922**, *121*, 1971–1984, (cit. on p. 21).

[162] S. Cusack, S. Lees, 'Variation of longitudinal acoustic velocity at gigahertz frequencies with water content in rat-tail tendon fibers', in *Biopolymers: Original Research on Biomolecules* **1984**, *23*, 337–351, (cit. on p. 26).

[163] P. H. Eilers, H. F. Boelens, 'Baseline correction with asymmetric least squares smoothing', in *Leiden University Medical Centre Report* **2005**, *1*, 5, (cit. on p. 29).

[164] K. J. NIKLAS, 'Voigt and Reuss models for predicting changes in Young's modulus of dehydrating plant organs', in *Annals of Botany* **1992**, *70*, 347–355, (cit. on p. 31).

[165] M. Alger, *Polymer science dictionary*, Springer Science & Business Media, **1996** (cit. on p. 31).

[166] A. Bigi, G. Cojazzi, S. Panzavolta, K. Rubini, N. Roveri, 'Mechanical and thermal properties of gelatin films at different degrees of glutaraldehyde crosslinking', in *Biomaterials* **2001**, *22*, 763–768, (cit. on p. 33).

[167] T. J. Hall, M. Bilgen, M. F. Insana, T. A. Krouskop, 'Phantom materials for elastography', in *IEEE transactions on ultrasonics ferroelectrics and frequency control* **1997**, *44*, 1355–1365, (cit. on p. 33).

[168] I. Yakimets, N. Wellner, A. C. Smith, R. H. Wilson, I. Farhat, J. Mitchell, 'Mechanical properties with respect to water content of gelatin films in glassy state', in *Polymer* **2005**, *46*, 12577–12585, (cit. on p. 33).

[169] S. Kalyanam, R. D. Yapp, M. F. Insana, 'Poro-viscoelastic behavior of gelatin hydrogels under compression-implications for bioelasticity imaging', in *Journal of Biomechanical Engineering* **2009**, *131*, 081005, (cit. on p. 33).

[170] P. Shao, T. G. Seiler, A. M. Eltony, A. Ramier, S. J. Kwok, G. Scarcelli, R. Pineda II, S.-H. Yun, 'Effects of corneal hydration on Brillouin microscopy in vivo', in *Investigative ophthalmology & visual science* **2018**, *59*, 3020–3027, (cit. on p. 35).

[171] H. Kragh, 'The Lorenz-Lorentz formula: Origin and early history', in *Substantia* **2018**, *2*, 7–18, (cit. on p. 35).

[172] G. Monaco, A. Cunsolo, G. Ruocco, F. Sette, 'Viscoelastic behavior of water in the terahertz-frequency range: An inelastic x-ray scattering study', in *Physical Review E* **1999**, *60*, 5505, (cit. on p. 38).

[173] L. Lupi, L. Comez, C. Masciovecchio, A. Morresi, M. Paolantoni, P. Sassi, F. Scarponi, D. Fioretto, 'Hydrophobic hydration of tert-butyl alcohol studied by Brillouin light and inelastic ultraviolet scattering', in *The Journal of chemical physics* **2011**, *134*, 02B603, (cit. on pp. 38, 39).

[174] S. Varma, J. P. Orgel, J. D. Schieber, 'Nanomechanics of Type I collagen', in *Biophysical journal* **2016**, *111*, 50–56, (cit. on p. 38).

[175] G. Möhlmann, 'Raman spectra of aqueous solutions of formaldehyde and its oligomers', in *Journal of Raman spectroscopy* **1987**, *18*, 199–203, (cit. on p. 41).

[176] N. Lebrun, P. Dhamelincourt, C. Focsa, B. Chazallon, J. Destombes, D. Prevost, 'Raman analysis of formaldehyde aqueous solutions as a function of concentration', in *Journal of Raman Spectroscopy* **2003**, *34*, 459–464, (cit. on p. 41).

[177] Z. Huang, A. McWILLIAMS, S. Lam, J. English, D. I. McLEAN, H. Lui, H. Zeng, 'Effect of formalin fixation on the near-infrared Raman spectroscopy of normal and cancerous human bronchial tissues', in *International journal of oncology* **2003**, *23*, 649–655, (cit. on p. 42).

[178] M. Jastrzebska, R. Wrzalik, A. Kocot, J. Zalewska-Rejdak, B. Cwalina, 'Raman spectroscopic study of glutaraldehyde-stabilized collagen and pericardium tissue', in *Journal of Biomaterials Science Polymer Edition* **2003**, *14*, 185–197, (cit. on p. 42).

[179] P. J. Flory, R. R. Garrett, 'Phase transitions in collagen and gelatin Systems1', in *Journal of the American Chemical Society* **1958**, *80*, 4836–4845, (cit. on p. 46).

[180] S. Corezzi, D. Fioretto, P. Rolla, 'Bond-controlled configurational entropy reduction in chemical vitrification', in *Nature* **2002**, *420*, 653–656, (cit. on p. 46).

[181] S. Corezzi, L. Comez, G. Monaco, R. Verbeni, D. Fioretto, 'Bond-induced ergodicity breakdown in reactive mixtures', in *Physical review letters* **2006**, *96*, 255702, (cit. on pp. 46, 95).

[182] W. Gotze, L. Sjogren, 'Relaxation processes in supercooled liquids', in *Reports on progress in Physics* **1992**, *55*, 241, (cit. on pp. 46, 91, 94, 95).

[183] M. Takeuchi, S. Kajimoto, T. Nakabayashi, 'Experimental evaluation of the density of water in a cell by Raman microscopy', in *The Journal of Physical Chemistry Letters* **2017**, *8*, 5241–5245, (cit. on p. 51).

[184] B. G. Frushour, J. L. Koenig, 'Raman scattering of collagen, gelatin, and elastin', in *Biopolymers: Original Research on Biomolecules* **1975**, *14*, 379–391, (cit. on pp. 53, 54).

[185] J. J. Cárcamo, A. E. Aliaga, R. E. Clavijo, M. R. Brañes, M. M. Campos-Vallette, 'Raman study of the shockwave effect on collagens', in *Spectrochimica Acta Part A: Molecular and Biomolecular Spectroscopy* **2012**, *86*, 360–365, (cit. on p. 53).

[186] J. De Gelder, K. De Gussem, P. Vandenabeele, L. Moens, 'Reference database of Raman spectra of biological molecules', in *Journal of Raman Spectroscopy: An International Journal for Original Work in all Aspects of Raman Spectroscopy Including Higher Order Processes and also Brillouin and Rayleigh Scattering* **2007**, *38*, 1133–1147, (cit. on p. 53).

[187] Q. Zhang, K. Andrew Chan, G. Zhang, T. Gillece, L. Senak, D. J. Moore, R. Mendelsohn, C. R. Flach, 'Raman microspectroscopic and dynamic vapor sorption characterization of hydration in collagen and dermal tissue', in *Biopolymers* **2011**, *95*, 607–615, (cit. on pp. 53, 59).

[188] L. E. Masson, C. M. O'Brien, I. J. Pence, J. L. Herington, J. Reese, T. G. van Leeuwen, A. Mahadevan-Jansen, 'Dual excitation wavelength system for combined fingerprint and high wavenumber Raman spectroscopy', in *Analyst* **2018**, *143*, 6049–6060, (cit. on p. 54).

[189] E. Li-Chan, 'The applications of Raman spectroscopy in food science', in *Trends in Food Science & Technology* **1996**, *11*, 361–370, (cit. on p. 54).

[190] A. Duconseille, C. Gaillard, V. Santé-Lhoutellier, T. Astruc, 'Molecular and structural changes in gelatin evidenced by Raman microspectroscopy', in *Food Hydrocolloids* **2018**, *77*, 777–786, (cit. on p. 54).

[191] P. C. Cross, J. Burnham, P. A. Leighton, 'The Raman spectrum and the structure of water', in *Journal of the American Chemical Society* **1937**, *59*, 1134–1147, (cit. on p. 54).

[192] D. M. Carey, G. M. Korenowski, 'Measurement of the Raman spectrum of liquid water', in *The Journal of chemical physics* **1998**, *108*, 2669–2675, (cit. on p. 54).

[193] S. Leikin, V. Parsegian, W.-H. Yang, G. Walrafen, 'Raman spectral evidence for hydration forces between collagen triple helices', in *Proceedings of the National Academy of Sciences* **1997**, *94*, 11312–11317, (cit. on p. 55).

[194] N. Correa, S. Harding, M. Bailey, S. Brasselet, F. Palombo, 'Image analysis applied to Brillouin images of tissue-mimicking collagen gelatins', in *Biomedical optics express* **2019**, *10*, 1329–1338, (cit. on pp. 62–64).

[195] P. J. Rousseeuw, 'Silhouettes: a graphical aid to the interpretation and validation of cluster analysis', in *Journal of computational and applied mathematics* **1987**, *20*, 53–65, (cit. on p. 73).

[196] R. Tibshirani, G. Walther, T. Hastie, 'Estimating the number of clusters in a data set via the gap statistic', in *Journal of the Royal Statistical Society: Series B (Statistical Methodology)* **2001**, *63*, 411–423, (cit. on p. 73).

[197] Andor, Full Well Capacity and Dynamic Range in CCD Cameras, tech. rep., Oxford Instruments (cit. on p. 78).

[198] K. Nishizawa, K. Fujiwara, M. Ikenaga, N. Nakajo, M. Yanagisawa, D. Mizuno, 'Universal glass-forming behavior of in vitro and living cytoplasm', in *Scientific reports* **2017**, *7*, 1–12, (cit. on pp. 83, 88).

[199] A. A. Hyman, C. A. Weber, F. Jülicher, 'Liquid-liquid phase separation in biology', in *Annual review of cell and developmental biology* **2014**, *30*, 39–58, (cit. on p. 83).

[200] T. Dehoux, Probing molecular crowding in compressed tissues with Brillouin light scattering, *Conference presentation at 5th BioBrillouin meeting*, 12-14 Oct. **2021**, (cit. on p. 83).

[201] D. Overby, A predictive relationship between Young's modulus and Brillouin modulus for living cells, *Conference presentation at 5th BioBrillouin meeting*, 12-14 Oct. **2021**, (cit. on p. 83).

[202] F. Alvarez, A. Alegra, J. Colmenero, 'Relationship between the time-domain Kohlrausch-Williams-Watts and frequency-domain Havriliak-Negami relaxation functions', in *Physical Review B* **1991**, *44*, 7306, (cit. on p. 91).

[203] W. Gotze, 'The scaling functions for the β-relaxation process of supercooled liquids and glasses', in *Journal of Physics: Condensed Matter* **1990**, *2*, 8485, (cit. on p. 92).

[204] C. J. Montrose, V. A. Solovyev, T. A. Litovitz, 'Brillouin Scattering and Relaxation in Liquids', in *The Journal of the Acoustical Society of America* **1968**, *43*, 117–130, DOI 10.1121/1.1910741, (cit. on p. 92).

[205] L. Comez, C. Masciovecchio, G. Monaco, D. Fioretto, 'Progress in liquid and glass physics by Brillouin scattering spectroscopy', in *Solid state physics* **2012**, *63*, 1–77, (cit. on p. 92).

[206] N. G. McCrum, B. E. Read, G. Williams, 'Anelastic and dielectric effects in polymeric solids', in **1967**, (cit. on p. 93).

[207] S. Caponi, M. Zanatta, A. Fontana, L. Bove, L. Orsingher, F. Natali, C. Petrillo, F. Sacchetti, 'Ergodicity breaking in strong and network-forming glassy systems', in *Physical Review B* **2009**, *79*, 172201, (cit. on p. 95).

[208] F. Mallamace, C. Corsaro, N. Leone, V. Villari, N. Micali, S.-H. Chen, 'On the ergodicity of supercooled molecular glass-forming liquids at the dynamical arrest: the o-terphenyl case', in *Scientific Reports* **2014**, *4*, 1–8, (cit. on p. 95).

[209] R. Casalini, M. Paluch, C. M. Roland, 'Dynamic crossover in supercooled liquids induced by high pressure', in *The Journal of chemical physics* **2003**, *118*, 5701–5703, (cit. on p. 95).